Fast Methods for Millimeter-wave Dielectric Resonator and Antenna Analysis and Design

by

Huanyu Chen

A thesis
presented to the University of Waterloo
in fulfillment of the
thesis requirement for the degree of
Master of Applied Science
in
Electrical and Computer Engineering

Waterloo, Ontario, Canada, 2009

I hereby declare that I am the sole author of this thesis. This is a true copy of the thesis, including any required final revisions, as accepted by my examiners.

I understand that my thesis may be made electronically available to the public.

Abstract

Ever-increasing interest in millimeter-wave and terahertz spectrum has prompted research and development of novel passive components working at these frequencies. Compared with the conventional planar components, non-planar dielectric devices become more attractive as frequencies increase due to their higher quality factors and dimensional tolerances. In this thesis, we present fast methods to analyze the millimeter-wave dielectric resonator and rod antenna.

First, an analytical method has been developed to evaluate resonant frequencies, quality factors of the Whispering Gallery Mode (WGM) disk resonators and also the resonator-waveguide coupling. A numerical solver based on full-wave finite element method is implemented to verify the analytical result. This analytical model provides a solution for fast design and optimization of WGM resonators in filter and sensor applications.

Secondly, a fast analytical approach based on local mode theory is introduced to calculate the radiation from tapered dielectric rod antenna. This efficient approximate model consumes much less computing resources and time, and demonstrates good agreements with full-wave numerical results. It supplies a quantitative way to understand the radiation mechanism and interaction between different parts of the antenna. Based on this, design criteria for the taper profile of rod antennas are given.

Acknowledgements

I would like to thank my supervisor Prof. Safieddin Safavi-Naeini for his support and invaluable guidance over the entire period of my study. Many thanks are due to Dr. Suren Gigoyan, without whom little of this work would be possible.

I am also grateful for the insightful suggestions made by the two readers of my thesis, Prof. Simarjeet Saini and Prof. A. Hemad Majedi.

Last, I would like to express my appreciations to all the fellow researchers and students in our group for many helpful discussions. Special thanks are extended to Mr. Mohammad Neshat, Mr. George Shaker and Dr. Daryoosh Saeedkia for providing countless helps.

Dedication

I would like to dedicate this thesis to my fiancee, Xiang Wang and my parents, who offered me unconditional love and support all the time.

Contents

List of Tables

List of Figures

Chapter 1

Introduction

1.1   Overview

Communication devices and systems at the millimeter-wave (mmW) range of frequencies (30-300GHz) are active research areas which have been applied to military terrestrial communication systems, sub-mmW imaging, high sensitivity sensor, and collision avoidance radar. Compared to devices at microwave frequency, mmW components are smaller which enables a traveling wave antenna having a featured size of several wavelengths [73]. Millimeter waves are also more sensitive to tiny objects due to smaller wavelengths, which have found important applications in imaging systems and biosensors. At this range of frequencies, guided-wave device configurations are versatile, which can be non-planar or planar, dielectric-based or metal-based. However, the conventional planar technologies suffer from skin-depth effect as the frequency becomes higher. This effect will degrade the component quality factor and increase insertion loss in the system. As a result, non-planar devices based on dielectric waveguides, inherently low-loss, attract considerable attentions especially for high-Q application. Many passive mmW dielectric components were proposed as building-blocks for mmW integrated circuits. Among them, dielectric waveguides, e.g. dielectric image line [75], NRD guide [90] and rectangular waveguide [39], are the most fundamental components being used. As natural extensions to these dielectric waveguides, high-gain efficient traveling-wave dielectric radiators including uniform rods [58], tapered rods [73] and tapered image lines [71, 21] have also been proposed. These dielectric rod antennas are good candidates for high gain satellite communication and more recently for the high-speed wireless transceivers at 60GHz [32]. In addition to the dielectric waveguides and rod antennas, dielectric resonators (DR) are also critical components in many mmW circuits. Compared with DRs working with lower-order modes, the oversized dielectric resonators using their Whispering Gallery modes [79], remain less explored. However, they have recently found interesting applications in high-Q bandstop filters [35],

spectroscopy measurements [4] and sensors [59]. As a combination of the afore-mentioned components, a sample fully-dielectric system comprising low loss image waveguides, integrated a tapered rod lens antenna, and an oversized disk resonator filter is shown in Figure 1.1. As is also illustrated, a broadband and low loss copla-nar waveguide to dielectric waveguide transition is important in a passive dielectric system packaging with active solid state devices. The design and optimization of each component using full-wave electromagnetic solvers will be inefficient due to their relatively large sizes. Fast analyzing methods are in demand not only for enabling faster designs but also for providing the underlying working mechanism.
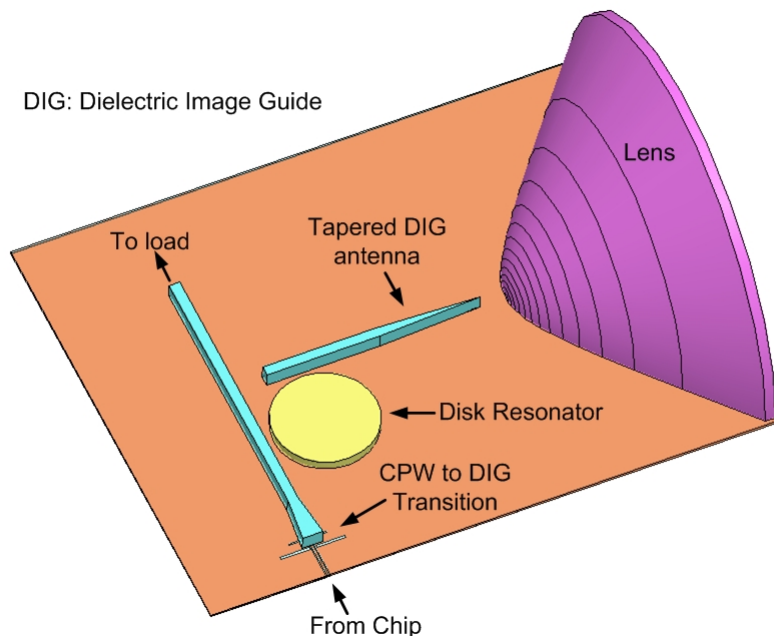
Figure 1.1: A mmW quasi-optical dielectric system consisting of lens antenna and disk resonator filter fed from coplanar waveguide

1.2 Outline

The objective of this thesis is to present fast methods for analyzing the two key com-ponents shown in Figure 1.1, the oversized disk resonator working with Whispering Gallery Modes and the tapered dielectric rod antenna.

In Chapter 2, we describe the proposed analytical model for WGM resonator by giving the predicted resonance frequencies for various kinds of the WGM resonators and their quality factors at resonance. A finite element method based numerical solver is implemented and its results are verified with the analytical results. In the last section, a coupled mode formulation is given for calculating waveguide-resonator coupling.

Chapter 3 provides an analytical model for circular dielectric tapered rod antenna. The calculated radiation patterns are compared with the numerical simulation and those in the literature. A discussion of optimal taper profiles and their design guidelines are presented. Finally, a phase-center analysis is supplied to help the integration of the tapered rod with lens antenna.

Conclusion and future works are given in Chapter 4.

Chapter 2

Whispering Gallery Mode Resonators

2.1 Introduction

Whispering Gallery mode (WGM) was first named by Lord Rayleigh after the Whispering Gallery at St. Paul's Church in London [65]. The high-Q WGM resonator is becoming an active research topic [82, 81, 54]. These resonators, in the shape of sphere, disk and ring, are widely used in millimeter-wave and optical devices such as sensors [46, 14], filters [50, 18, 35] , material characterizations and spectroscopy [43, 4], delay lines [52], microwave receivers [31] and microcavity lasers [55, 7].

Spherical WGM resonators, mostly used at optical frequencies, are relatively well-understood due to the existence of rigorous solutions for these WGMs by the series expansion [12, 54, 51]. On the other hand, the planar WGM resonators, whose machining is actually easier at mmW range, remain less explored due to the absence of rigorous analytical solutions. Full-wave numerical techniques are therefore applied to analyze these planar resonators. Making use of the rotational symmetry of these resonators, computational methods such as Finite Different Time Domain (FDTD) [77, 49] , Finite Element Method (FEM) [48] and radial Mode Matching Method [17] for body of revolution (BOR) are applied to evaluate the WGM resonant eigenmode fields and frequencies. However, all the rigorous numerical methods are computationally complex, which limits their application in fast design and optimization. To overcome this difficulty, approximate models such as Dielectric Waveguide Model (DWM) [34, 37] and Effective Dielectric Constant (EDC) method [56] have been proposed to calculate the resonance frequencies of dielectric resonators (DR) with much less computational burden and fairly accurate results. Nevertheless, these analytical models were originally reported to calculate the resonance frequencies of low-order modes in DR for DR filter and DR antenna (DRA) applications. Tobar et al. [79] extended the DWM to characterize the resonance frequencies of WGM in

a single-layered disk resonator. Further, Peng proposed a similar analytical method by alternating the dispersion equation in axial direction to characterize the axially stacked double disk resonator [64]. In the first section of this chapter, the resonance frequency analysis by DWM for the layered WGM disk is reviewed and novel study for ring resonator is presented.

Other than the resonance frequency of WGM, the quality factor at resonance is also a crucial parameter in most of the applications [37]. The quality factor can be categorized into three parts associated with dielectric, radiation and conduction losses, respectively. The radiation loss, also called whispering gallery loss, is the intrinsic loss in WGM resonators owing to the tunneling energies leak from the curved surface as a ray-optics explanation [51]. To estimate this loss, many methods are proposed, such as the WKB method based on conformal transformation [9, 18], direct complex roots of dispersion equation [69, 57, 29] and the volume current method [45, 51]. Even so, the WKB method solves only the scalar wave equation which assumes the mode is either TE or TM while WG modes are hybrid modes. This scalar approximation is only valid when the mode is weakly guided. The direct complex root method gives the complex resonance frequencies of a 2D infinite cylinder while the disk resonator in our problem is 3D. The volume current method is valid for 3D structures and is therefore adopted in our analysis. Approximate expressions for dielectric loss and conduction quality factor for WGM disk resonator are also introduced in the second section of this chapter. The analysis is based on the fields obtained from DWM and perturbation theory. The results are shown to be useful in design and analysis of WGM resonators for applications like pharmaceutical tablet sensors and dielectric constant measurement [43].

In addition to the analysis done for an isolated WGM resonator, an excitation mechanism for the resonator is necessary. Among a variety of excitation methods [54], the use of a dielectric waveguide evanescent coupler is the most popular ways, which is becoming an important building-block for large scale photonic circuits [51, 50]. Knowing the coupling coefficient between the waveguide and resonator, we can estimate the coupling quality factor which is very useful in our sensor analysis [59]. Coupled Mode Theory (CMT) has been successfully used to study the wave coupling phenomenon in guided-wave optics [53, 88, 28]. Recently, CMT has been applied to investigate the coupling between 2D WGM in a cylinder and a slab waveguide [69], the coupling of a ring resonator and a rectangular waveguide [50], and the coupling of a spherical resonator and a tapered optical fiber [23, 51]. Simple straight waveguide field distributions are used in [50] to evaluate the overlapped integral in CMT which neglect the perturbation of modes due to the finite bending curvature in ring resonator. Here, we present a study as an extension to the work done by Little et al. [51] to analyze the coupling from a dielectric rectangular-core waveguide to a WGM disk resonator. In our analysis, field distributions approximated by DWM are used to evaluate the overlapped integral.

5

2.2   Resonance Frequency Analysis

The WGMs in layered disk resonator are closely related to the higher-order modes in circular rod waveguide [83]. Therefore, this section starts from revisiting the higher-order hybrid modes in circular rod.

2.2.1   Higher-Ordered Hybrid Modes in a Circular Dielectric Waveguide

The 2D Whispering Gallery modes in an infinitely long circular dielectric waveguide are essentially the higher-order hybrid modes (HEM) of the dielectric waveguide [83]. E_z and H_z fields in a rod with symmetric axis along z satisfy the scalar Helmholtz equation in cylindrical coordinates $\{\rho, \phi, z\}$, whose solutions are Bessel functions. All the other field components can be derived from E_z and H_z. A time-harmonic dependency $e^{j\omega t}$ is assumed and suppressed throughout this thesis.

$$\left[\frac{1}{\rho}\frac{\partial}{\partial\rho}\rho\frac{\partial}{\partial\rho} + \frac{1}{\rho^2}\frac{\partial^2}{\partial\phi^2} + k_\rho^2 \right] \left[\begin{array}{c} E_z \\ H_z \end{array} \right] = 0$$

$$
\begin{aligned}
E_\rho &= \frac{j}{k_\rho^2}\left(-k_z\frac{\partial E_z}{\partial\rho} - \frac{\omega\mu_0}{\rho}\frac{\partial H_z}{\partial\phi} \right) \\
E_\phi &= \frac{j}{k_\rho^2}\left(-\frac{k_z}{\rho}\frac{\partial E_z}{\partial\phi} + \omega\mu_0\frac{\partial H_z}{\partial\rho} \right) \\
H_\rho &= \frac{j}{k_\rho^2}\left(\frac{\omega\varepsilon}{\rho}\frac{\partial E_z}{\partial\phi} - k_z\frac{\partial H_z}{\partial\rho} \right) \\
H_\phi &= \frac{j}{k_\rho^2}\left(-\omega\varepsilon\frac{\partial E_z}{\partial\rho} - \frac{k_z}{\rho}\frac{\partial H_z}{\partial\phi} \right)
\end{aligned}
$$

where $k_\rho^2 = \varepsilon_r k_0^2 - k_z^2$

Using the above expressions and applying boundary conditions on the core-cladding interface, the famous transcendental equation [61] for determining the $k_z - k_0$ dispersion relationship of HEM is obtained and shown as

$$\left[\frac{J_n'(u)}{uJ_n(u)} + \frac{K_n'(v)}{vK_n(v)} \right]\left[\frac{J_n'(u)}{uJ_n(u)} + \frac{K_n'(v)}{\varepsilon_r vK_n(v)} \right] = \left(\frac{nk_z}{k_0} \right)^2 \left(\frac{1}{u^2} + \frac{1}{v^2} \right)^2 \qquad (2.1)$$

or its equivalent form

6

$$\left[\frac{J_n'(u)}{uJ_n(u)} + \frac{K_n'(v)}{vK_n(v)}\right]\left[\frac{J_n'(u)}{uJ_n(u)} + \frac{K_n'(v)}{\varepsilon_r vK_n(v)}\right] = n^2\left(\frac{1}{u^2} + \frac{1}{v^2}\right)\left(\frac{1}{u^2} + \frac{1}{\varepsilon_r v^2}\right)$$
$$(2.2)$$

where k_z is the waveguide propagation constant in axial direction, k_0 is the free space wave number, ε_r is the dielectric constant of filling material and $u = k_{\rho 1}a$ and $v = \alpha_\rho a$, with a as the radius of the cylinder and

$$k_{\rho 1} = \sqrt{k_0^2\varepsilon_r - k_z^2}$$
$$\alpha_\rho = \sqrt{k_z^2 - k_0^2} \qquad (2.3)$$

$J_n(\cdot)$ and $K_n(\cdot)$ are the n-th order Bessel function of the first kind and modified Bessel function of the second kind, respectively. $J_n'(\cdot)$, $K_n'(\cdot)$ are the derivatives of Bessel functions with respect to the argument. Their recurrence relationships are shown in (A.1) and (A.3).

It is clear from Equation (2.2) the axial wave numbers k_z and k_0 are coupled together. To have guided modes, the k_z should satisfy that $k_0 \leq k_z \leq \sqrt{\varepsilon}k_0$. For the region $k_z < k_0$ which means the guided modes are below cut-off, and radiation modes exist. Propagation constants of radiation modes belong to a continuous spectrum whose dispersion equation is different from (2.1). However, dispersion equation (2.1) can be solved for propagation constants $\tilde{k}_z$ of leaky modes. These $\tilde{k}_z$ are complex numbers and they are shown as $\tilde{k}_z = k_{zr} - jk_{zi}$ having $k_{zr} < k_0$. Here, k_{zr} and k_{zi} are both positive real number. Proper square root branch in (2.3) should be chosen to maintain a proper leaky mode. That is

$$\tilde{k}_{\rho 1} = \sqrt{k_0^2\varepsilon_r - k_z^2} = k_{\rho 1r} + jk_{\rho 1i}$$
$$\tilde{\alpha}_\rho = \sqrt{k_z^2 - k_0^2} = -\alpha_{\rho r} + j\alpha_{\rho i}$$

where $\alpha_{\rho r}$ and $\alpha_{\rho i}$ are both positive real number. This consideration should be taken into account when implementing a numerical root searching procedure for (2.1).

Interestingly, in the limit of $k_z \to 0$, the E_z and H_z of the hybrid mode are decoupled as a direct result from Maxwell's equation. With $k_z = 0$, the wave solutions are therefore uniform in the z direction and the problem is reduced in dimension. In this scenario, the TM mode with E_z is named WGH mode, and the TE mode with

7

H_z is named WGE mode. The left-hand side of Equation (2.1) reduces to zero and hence the dispersion equation is separated into two individual equations for each of the modes [82, 5, 69]

$$2D\ WGE\ mode: \quad \frac{J'_n\left(u_0\right)}{u_0 J_n\left(u_0\right)} - \frac{H_n^{(2)'}\left(v_0\right)}{v_0 H_n^{(2)}\left(v_0\right)} = 0$$

$$2D\ WGH\ mode: \quad \frac{J'_n\left(u_0\right)}{u_0 J_n\left(u_0\right)} - \frac{H_n^{(2)'}\left(v_0\right)}{\varepsilon_r v_0 H_n^{(2)}\left(v_0\right)} = 0 \qquad (2.4)$$

where $u_0 = \sqrt{\varepsilon_r}k_0 a$ and $v_0 = k_0 a$. In order to satisfy the above transcendental equation and radiation boundary condition, the solutions k_0 should be in the complex plane which means the resonance frequencies are complex and the waves are leaky in the isolated resonator. This is the leaky mode solution of Equation (2.1) in the limit of $k_z = 0$.

Equation (2.1) and (2.4) are solved numerically and the results are displayed in Figure 2.1. It is clearly demonstrated that the leaky mode in this case is the analytical continuation of guided mode under cut-off (under the light line). The complex resonance frequency solved from (2.4) is a special case for leaky mode with $k_z = 0$.
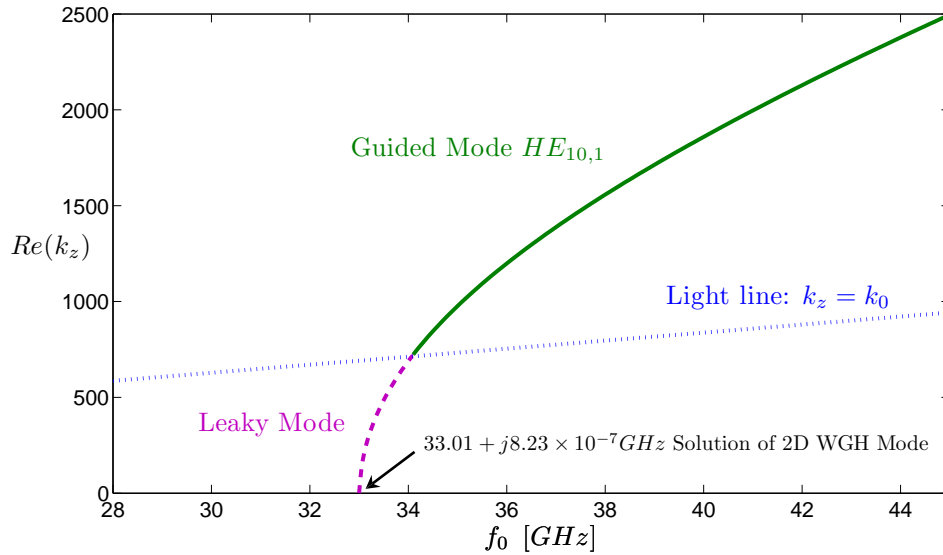
Figure 2.1: Propagation constants varies with frequencies for the lowest guided mode and leaky mode of a circular waveguide with $n = 10$, $\varepsilon_r = 14.8$ and radius $a = 5mm$.

8

2.2.2 Dielectric Waveguide Model

Dielectric Waveguide Model (DWM) has been proposed in [34] to analytically predict the resonance frequencies of a dielectric resonator (DR). It is a simple extension of the Marcatili's method [53] which has been successfully used to find the propagation constants of a dielectric waveguide with rectangular cross-section.

The basic idea of DWM and Marcatili's method is to reduce the dimensions of the object under investigation and obtain the approximate boundary condition of a simplified geometry. In this fashion, two dispersion equations are obtained for the cylindrical DR. One is along the axis of symmetry and the other is along the radial direction. To demonstrate the method, we demonstrate the basic procedures for a cylindrical resonator with a radius a and a thickness b on top of a ground plane (Figure 2.2) : First, the DR is flatten as grounded radial slab waveguide with a thickness b to obtain dispersion in axial direction which is well-known; Secondly, the resonator is protruded in axial direction as an infinitely long cylinder to obtain the radial boundary condition of which the dispersion equation is that (2.1) for circular waveguide in the last section. The WGMs in an isolated disk resonator are generally denoted as $WGH_{n,m,l}$ or $WGE_{n,m,l}$ modes [64, 5, 79]. The n, m and l are the node numbers of field variations along the azimuthal, radial and axial directions, respectively. $WGH_{n,m,l}$ mode is a quasi-TM mode and $WGE_{n,m,l}$ mode is a quasi-TE mode. In DWM, their axial dispersion equations correspond to those of the TM_l mode and TE_l mode in a slab waveguide, respectively. In a grounded disk resonator (Figure 2.2), the lowest mode for a certain azimuthal number n is $WGH_{n,1,0}$ mode while the $WGE_{n,1,0}$ mode is suppressed.

The dispersion equations of TM and TE modes are well-known for grounded slab waveguide of a thickness b [42]

$$TM\ mode:\ \frac{\varepsilon_r \alpha_{z0}}{k_z} = \tan(k_z b) \tag{2.5}$$

$$TE\ mode:\ \frac{\alpha_{z0}}{k_z} = -\cot(k_z b) \tag{2.6}$$

where $\alpha_{z0} = \sqrt{k_0^2(\varepsilon_r - 1) - k_z^2}$ is the exponential decaying constant in the air cladding of the slab waveguide modes. In DWM, we adopt these two equations for the axial dispersion equations of WGH and WGE modes, respectively. We have two unknowns k_0 and k_z in either of these two equations. It is therefore necessary to correlate them with the radial dispersion equation solving for k_0. Accordingly, for both WGH and WGE modes, the radial dispersion equation (Equation 2.2) is the same since that equation is universal for hybrid modes in circular waveguide.

The wave numbers k_0 and hence the resonance frequencies for $WGH_{n,m,l}$ and $WGE_{n,m,l}$ modes in a grounded disk are determined through solving the two simultaneous dispersion equations shown as follows

9
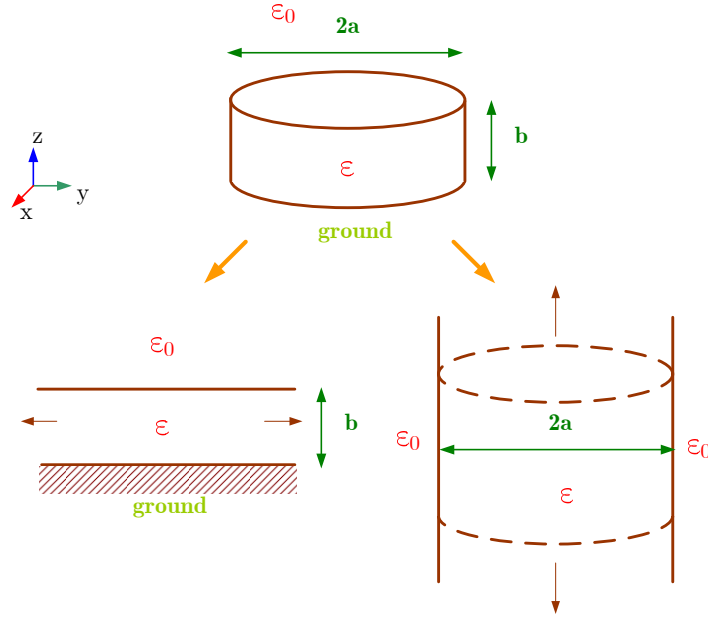
Figure 2.2: Illustration of Dielectric Waveguide Model for grounded single layered disk resonator

$WGH_{n,m,l}\ mode$:

$$\begin{cases} \left[\frac{J'_n(u)}{uJ_n(u)} + \frac{K'_n(v)}{vK_n(v)}\right]\left[\frac{J'_n(u)}{uJ_n(u)} + \frac{K'_n(v)}{\varepsilon_r vK_n(v)}\right] = n^2\left(\frac{1}{u^2} + \frac{1}{v^2}\right)\left(\frac{1}{u^2} + \frac{1}{\varepsilon_r v^2}\right) \\ \frac{\varepsilon_r \alpha_{z0}}{k_z} = \tan(k_z b) \end{cases} \qquad (2.7)$$

$WGE_{n,m,l}\ mode$:

$$\begin{cases} \left[\frac{J'_n(u)}{uJ_n(u)} + \frac{K'_n(v)}{vK_n(v)}\right]\left[\frac{J'_n(u)}{uJ_n(u)} + \frac{K'_n(v)}{\varepsilon_r vK_n(v)}\right] = n^2\left(\frac{1}{u^2} + \frac{1}{v^2}\right)\left(\frac{1}{u^2} + \frac{1}{\varepsilon_r v^2}\right) \\ -\frac{\alpha_{z0}}{k_z} = \cot(k_z b) \end{cases} \qquad (2.8)$$

The above simultaneous transcendental equations can be solved numerically by Newton-Raphson root searching method or more intuitively by finding graphically the intersection point of the two dispersion curve shown as an example in Figure 2.3. The E_z field patterns for $WGH_{n,1,0}$ of a disk resonator are plotted in Figure 2.4. The resonator parameters are $\varepsilon_r = 14.8$, $a = 5mm$ and $b = 1mm$. In this figure, dashed line circles are plotted with a radius ρ_c defined as

$$\rho_c = \frac{n}{k_{\rho 1}}$$

This ρ_c can be considered as the inner caustic of $WGM_{n,1,0}$ mode. Most of the mode energies are confined in between $\rho = \rho_c$ and $\rho = a$ in the radial direction [5]. In addition, $\frac{n}{a}$ can be given as a starting guess for solving the dispersion equation by Newton-Raphson method.
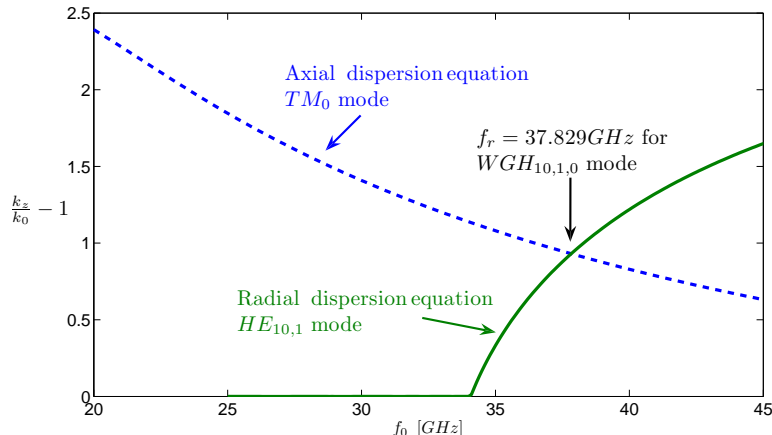
Figure 2.3: Graphical solution of the simultaneous transcendental equations (Equation 2.7) for $WGH_{10,1,0}$ mode of a disk resonator with $\varepsilon_r = 14.8$, $a = 5mm$ and $b = 1mm$.

2.2.3 Extension of DWM to the Analysis of Layered Disk Resonator

In the previous section, DWM is applied to a single-layered disk resonator. In the same fashion, the former procedure can be extended to calculate the resonances of axially and radially layered structure by simply modifying corresponding dispersion equations along the axial and radial directions, respectively. For these resonators, we will focus on the analysis of the $WGH_{n,1,0}$ modes which are usually more useful in real applications. It should be noted that although only two-layered structures are presented in the following analysis, the method is general and is easily extended to analyze multilayered resonators by substituting multilayered dispersion equations.

2.2.3.1 Dispersion Equation for Axially Layered Waveguide

By applying DWM to analyze the $WGH_{n,1,0}$ mode in a grounded axially two-layered dielectric disk shown in Figure 2.5, the transcendental equation governing k_z in Equation (2.7) is now modified to be the transcendental equation of the TM mode in a two-layered grounded slab waveguide [42] shown in Figure 2.5.
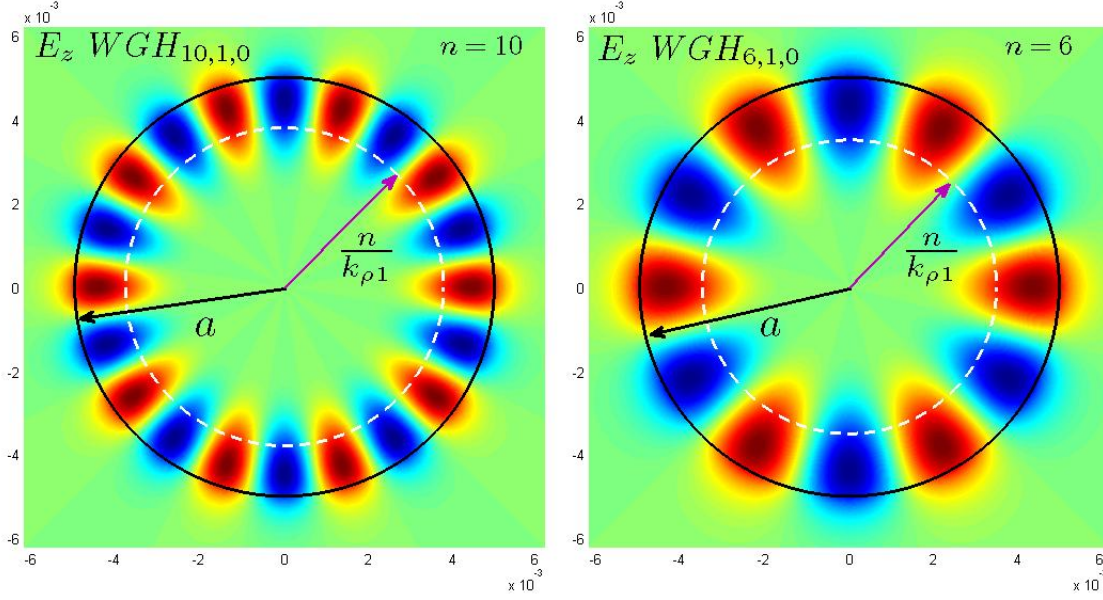
Figure 2.4: E_z fields patterns of $WGH_{n,1,0}$ mode of a disk resonator with $\varepsilon_r = 14.8$, $a = 5mm$ and $b = 1mm$.

$$1 - \frac{\varepsilon_{r1}k_z}{\varepsilon_r k_{z1}} \tan(k_z b) \tan(k_{z1}h) = \frac{1}{\alpha_{z0}\varepsilon_{r1}}\left[k_{z1}\tan(k_{z1}h) + \frac{\varepsilon_{r1}k_z}{\varepsilon_r}\tan(k_z b)\right] \quad (2.9)$$

where

$$
\begin{aligned}
\alpha_{z0} &= \sqrt{k_0^2(\varepsilon_{r1}-1) - k_{z1}^2} \\
k_{z1} &= \sqrt{k_z^2 - k_0^2(\varepsilon_r - \varepsilon_{r1})}
\end{aligned}
$$

The two simultaneous transcendental equations governing the $WGH_{n,m,l}$ mode in the axially two-layered system are

$$\begin{cases} \left[\frac{J_n'(u)}{uJ_n(u)} + \frac{K_n'(v)}{vK_n(v)}\right]\left[\frac{J_n'(u)}{uJ_n(u)} + \frac{K_n'(v)}{\varepsilon_r vK_n(v)}\right] = n^2\left(\frac{1}{u^2} + \frac{1}{v^2}\right)\left(\frac{1}{u^2} + \frac{1}{\varepsilon_r v^2}\right) \\ 1 - \frac{\varepsilon_{r1}k_z}{\varepsilon_r k_{z1}}\tan(k_z b)\tan(k_{z1}h) = \frac{1}{\alpha_{z0}\varepsilon_{r1}}\left[k_{z1}\tan(k_{z1}h) + \frac{\varepsilon_{r1}k_z}{\varepsilon_r}\tan(k_z b)\right] \end{cases} \quad (2.10)$$

The above simultaneous equations are solved and compared with the numerical and measured result shown in Figure 2.7. The graphical solution for the intersection
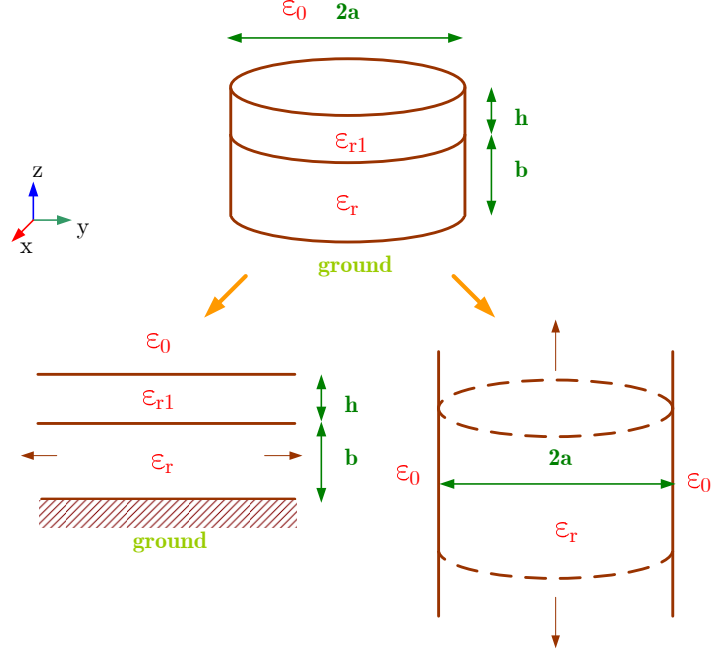
Figure 2.5: Axially double-layered disk resonator

points of the axial and radial transcendental equations in (2.10) is plotted in Figure 2.6. The numerical results are obtained from the eigenmode solver by a 2D Finite Element Method for Body of Revolution (FEM BOR) which will be described in the next section. It is demonstrated that those three sets of data agree well with each other. It is also observed that the calculated resonance frequencies by DWM are lower than the measured and numerical results. This behavior results from that the DWM overestimates the field confinement and hence the effective dielectric constant when solving the axial dispersion equation. A larger effective dielectric constant will bring down the resonance frequency.

2.2.3.2 Dispersion Equation for Radially Layered Resonator

In the case of radially layered resonator, the transcendental equation governing k_z simply remains unchanged as Equation (2.5). But the transcendental equation governing k_ρ will be complicated. We adopt the formulation for the radially multi-layered circular waveguide to solve k_ρ which is proposed by Yeh [89]. The dispersion equation of the two-layered waveguide shown in Figure 2.8 is obtained by setting the following determinant of the 4 by 4 matrix A equal to zero

$$\det(A) = 0 \tag{2.11}$$
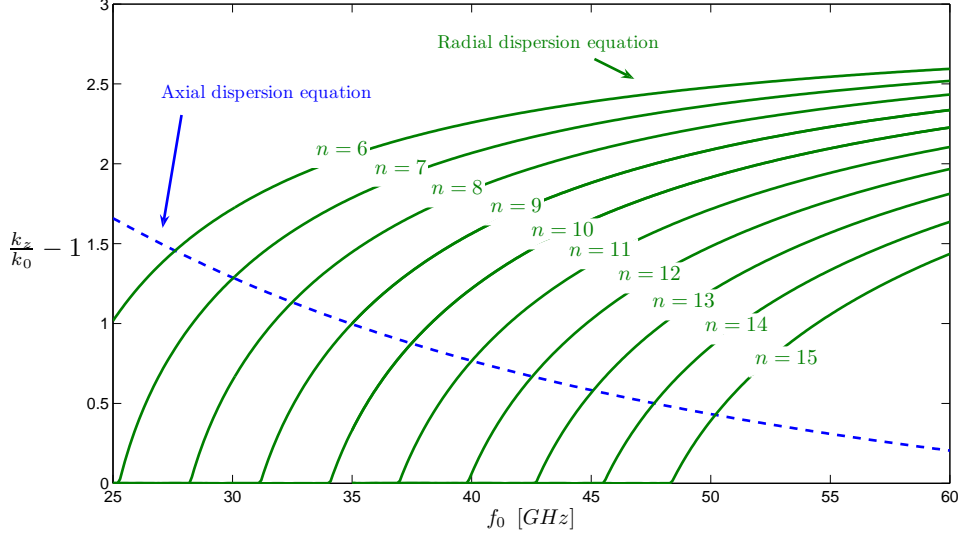
Figure 2.6: Graphical solution of the simultaneous transcendental equations (Equation 2.10) for $WGH_{n,1,0}$ mode of a axially two-layered disk resonator with $a = 5mm$, $b = 1mm$, $h = 4mm$, $\varepsilon_r = 14.8$ and $\varepsilon_{r1} = 2.33$.

$$A = \begin{bmatrix} c_1(r_1) & 0 & -M_{11} & -M_{13} \\ 0 & d_1(r_1) & -M_{21} & -M_{23} \\ e_1(r_1) & f_1(r_1) & -M_{31} & -M_{33} \\ g_1(r_1) & h_1(r_1) & -M_{41} & -M_{43} \end{bmatrix} \quad (2.12)$$

where

$$M = M_2(r_1)M_2^{-1}(r_2)M_3(r_2)$$

$$M_2(r) = \begin{bmatrix} c_2(r) & c_2'(r) & 0 & 0 \\ 0 & 0 & d_2(r) & d_2'(r) \\ e_2(r) & e_2'(r) & f_2(r) & f_2'(r) \\ g_2(r) & g_2'(r) & h_2(r) & h_2'(r) \end{bmatrix} \quad M_3(r) = \begin{bmatrix} s(r) & 0 & 0 & 0 \\ 0 & 0 & \tau(r) & 0 \\ u(r) & 0 & v(r) & 0 \\ w(r) & 0 & \chi(r) & 0 \end{bmatrix}$$

$$
\begin{array}{lll}
c_i(r) = J_n(k_{\rho i} r) & d_i(r) = \eta J_n(k_{\rho i} r) & e_i(r) = \frac{k_z n}{k_{\rho i}^2 r} J_n(k_{\rho i} r) \\
f_i(r) = \frac{j k_0 \eta}{k_{\rho i}} J_n'(k_{\rho i} r) & g_i(r) = -\frac{j k_0 \varepsilon_{ir}}{k_{\rho i}} J_n'(k_{\rho i} r) & h_i(r) = \frac{\eta k_z n}{k_{\rho i}^2 r} J_n(k_{\rho i} r) \\
s(r) = K_n(\alpha_\rho r) & \tau(r) = \eta K_n(\alpha_\rho r) & u(r) = -\frac{k_z n}{\alpha_\rho^2 r} K_n(\alpha_\rho r) \\
v(r) = -\frac{j k_0 \eta}{\alpha_\rho} K_n'(\alpha_\rho r) & w(r) = \frac{j k_0}{\alpha_\rho} K_n'(\alpha_\rho r) & \chi(r) = -\frac{\eta k_z n}{\alpha_\rho^2 r} K_n(\alpha_\rho r)
\end{array}
$$

$$k_{\rho i} = \sqrt{k_0^2 \varepsilon_{ri} - k_z^2} \quad \alpha_\rho = \sqrt{k_z^2 - k_0^2}$$

14
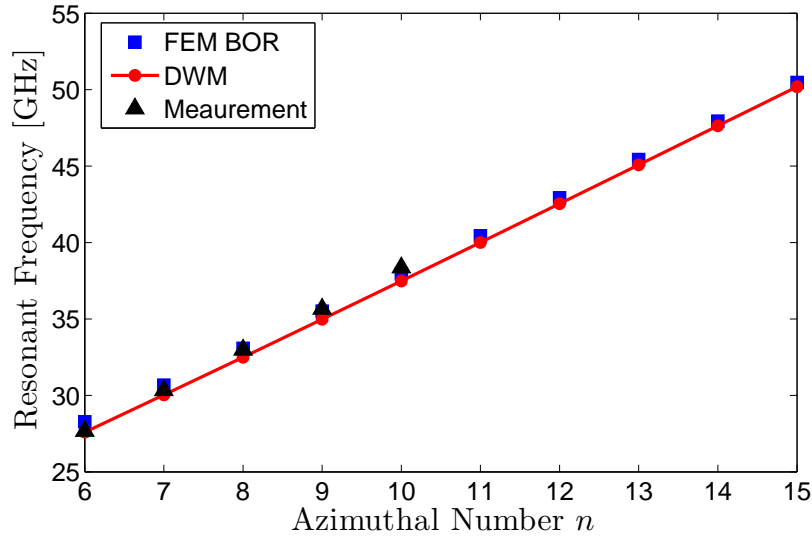
Figure 2.7: Analytical, numerical and measured result of resonance frequencies of an axially double-layered disk resonator. Structure parameters are chosen to be $a = 5mm$, $b = 1mm$, $h = 4mm$, $\varepsilon_r = 14.8$ and $\varepsilon_{r1} = 2.33$.

while the expression for $c_i'\tilde{\ } h_i'$ are simply the same as the unprimed $c_i\tilde{\ } h_i$ but with Bessel $J_n(\cdot)$ replaced by Bessel $Y_n(\cdot)$.

It should be noted that when $r_2 = r_1$, the dispersion equation Equation (2.12) will reduce to Equation (2.2). The two simultaneous transcendental equations governing the radially layered system are

$$
\begin{cases}
\det(A) = 0 \\
\frac{\varepsilon_r \alpha_{z0}}{k_z} = \tan(k_z b)
\end{cases}
\tag{2.13}
$$

Having the above equation solved, we compare the results with the FEM results with different azimuthal number n in Figure 2.9 where good agreements are shown.

2.3 Eigenmode Solver Using Finite Element Method for Body of Revolution

In order to validate the analytical result, an efficient numerical solver based on finite element method is implemented. Noticing that the structure in our analysis is axis-symmetric or the so-called Body of Revolution, we adopt the formulation solving just a cross-section of rather than the entire 3D revolutional structure [48, 49, 36]. The finite element method adopted here is formulated in cylindrical coordinate as

15
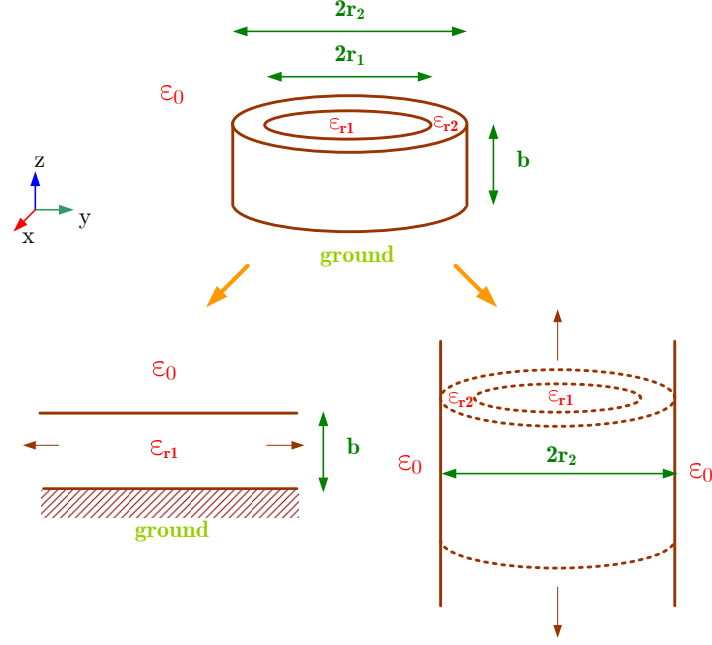
Figure 2.8: Radially double-layered disk resonator

introduced by Lee et al. [48] for calculating lower-order resonant modes . The following analysis starts from the vectorial Helmholtz equation

$$\overrightarrow{\nabla} \times \frac{1}{\mu_r} \overrightarrow{\nabla} \times \overrightarrow{E} - k_0^2 \varepsilon_r \overrightarrow{E} = 0 \tag{2.14}$$

where $k_0^2 = \omega_0^2 \varepsilon_0 \mu_0$ and $\overrightarrow{\nabla} = \hat{\rho}\frac{\partial}{\partial \rho} + \hat{z}\frac{\partial}{\partial z} + \hat{\phi}\frac{\partial}{\rho \partial \phi} = \overrightarrow{\nabla}_t + \hat{\phi}\frac{\partial}{\rho \partial \phi}$. Due to the axis-symmetry of the structure, the field components are periodic functions along ϕ axis. To solve for $WGM_{n,m,l}$ modes, the fields will have $e^{-jn\phi}$ dependency which is hence suppressed in the formulation by substituting the relationship $\frac{\partial}{\partial \phi} \rightarrow -jn$. Therefore, the actual 3D problem (2.14) is reduced into a 2D problem.

The electric fields are decomposed into transverse and azimuthal components

$$\overrightarrow{E} = \overrightarrow{E}_t + E_\phi \hat{\phi} \tag{2.15}$$

The formulation here is very similar to the mixed edge-nodal element formulation for waveguide analysis in Cartesian coordinate [47]. Here, the tangential components are expanded into the classic vectorial basis functions $\overrightarrow{N}_i$
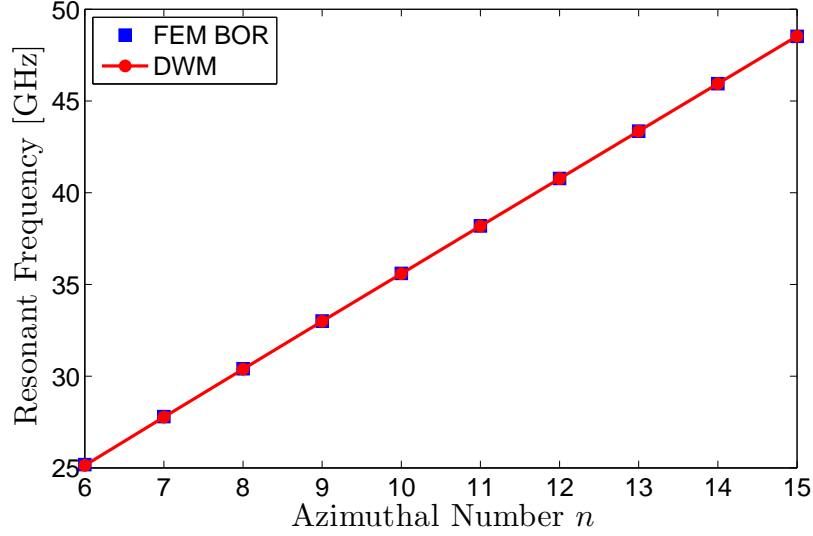
Figure 2.9: Analytical and numerical result for resonance frequencies of an axially double-layered disk resonator. Structure parameters are chosen to be $r_1 = 4mm$, $r_2 = 5mm$, $b = 3mm$, $\varepsilon_{r1} = 2.33$ and $\varepsilon_{r2} = 14.8$.

$$\overrightarrow{E}_t = j \sum_{i=1}^{N_e} E_{tj} \overrightarrow{N}_i \tag{2.16}$$

where N_e is the total number of edges in the triangular mesh of solution domain. The factor j in (2.16) is introduced to balance the overall equation factor so that this equation can be discretized into a matrix form with purely real entries.

A little modification should be added to the nodal basis function as compared to that in cartesian coordinate [47]. Here, they have the factor $\frac{1}{\rho}$ in the expansion which depends on the element location

$$E_\phi = \sum_{p=1}^{N_n} e_{\phi j} \frac{\varphi_p}{\rho} \tag{2.17}$$

Further, assuming outer boundary conditions of the solution domain is either of Dirichlet or Neumann type, the weak form of vector Helmholtz's (2.14) is

$$\iiint_V \left[\left(\frac{1}{\mu_r} \overrightarrow{\nabla} \times \overrightarrow{E}^w \right) \cdot \left(\frac{1}{\mu_r} \overrightarrow{\nabla} \times \overrightarrow{E} \right) - k_0^2 \varepsilon_r \overrightarrow{E}^w \cdot \overrightarrow{E} \right] dV = 0 \tag{2.18}$$

Using Galerkin's method, the testing function $\overrightarrow{E}^w$ is chosen the same as the basis function. By inserting (2.16) and (2.17) into (2.18) and neglecting the integration in the azimuthal direction, we have

$$\iint_S \frac{1}{\mu_r} \left\{ \rho \left(\vec{\nabla}_t \times \vec{N}_j \right) \cdot \left(\vec{\nabla}_t \times \vec{N}_i \right) + \frac{n^2}{\rho} \left(\vec{N}_j \cdot \vec{N}_i \right) \right.$$
$$- \frac{n}{\rho} \left[\left(\vec{N}_j \cdot \vec{\nabla}_t \varphi_p \right) + \left(\vec{\nabla}_t \varphi_q \cdot \vec{N}_i \right) \right] + \frac{1}{\rho} \left(\vec{\nabla}_t \varphi_q \cdot \vec{\nabla}_t \varphi_p \right)$$
$$\left. - k_0^2 \varepsilon_r \left[\rho \left(\vec{N}_j \cdot \vec{N}_i \right) + \frac{1}{\rho} \varphi_q \varphi_p \right] \right\} d\rho dz = 0 \qquad (2.19)$$

The above equation can be evaluated on basis of a single triangular element and its corresponding local matrix. The local matrices produced by all elements are then assembled to the overall matrix to be solved [13]. In order to have a universal expression of the local matrix elements, the location dependent ρ in the integration should be got rid off. This is done by replacing ρ with ρ_c at the centroid of each element as long as the mesh is dense enough. Finally, the local matrix can be written in the following form

$$\begin{bmatrix} S_{tt}^e & S_{t\phi}^e \\ S_{\phi t}^e & S_{z\phi}^e \end{bmatrix} \begin{bmatrix} E_t^e \\ e_\phi^e \end{bmatrix} = k_0^2 \begin{bmatrix} M_{tt}^e & 0 \\ 0 & M_{\phi\phi}^e \end{bmatrix} \begin{bmatrix} E_t^e \\ e_\phi^e \end{bmatrix} \qquad (2.20)$$

Here, the sub-matrices S_{tt}^e, $S_{t\phi}^e$, $S_{\phi t}^e$ and $S_{z\phi}^e$ are all 3×3 matrices. Their entries are

$$[S_{tt}^e]_{ji} = \frac{1}{\mu_r^e} \left[\rho_c^e \iint_\triangle \left(\vec{\nabla}_t \times \vec{N}_j^e \right) \cdot \left(\vec{\nabla}_t \times \vec{N}_i^e \right) dS + \frac{n^2}{\rho_c^e} \iint_\triangle \vec{N}_j^e \cdot \vec{N}_i^e dS \right] \qquad (2.21)$$

$$[S_{t\phi}^e]_{jp} = \frac{n}{\mu_r^e \rho_c^e} \iint_\triangle \vec{N}_j^e \cdot \vec{\nabla}_t \varphi_p^e dS \qquad (2.22)$$

$$[S_{t\phi}^e]_{iq} = \frac{n}{\mu_r^e \rho_c^e} \iint_\triangle \vec{N}_i^e \cdot \vec{\nabla}_t \varphi_q^e dS \qquad (2.23)$$

$$[S_{\phi\phi}^e]_{qp} = \frac{1}{\mu_r^e \rho_c^e} \iint_\triangle \vec{\nabla}_t \varphi_q^e \cdot \vec{\nabla}_t \varphi_p^e dS \qquad (2.24)$$

$$[M_{tt}^e]_{ji} = \varepsilon_r^e \rho_c^e \iint_\triangle \vec{N}_j^e \cdot \vec{N}_i^e dS \qquad (2.25)$$

$$[M_{\phi\phi}^e]_{qp} = \frac{\varepsilon_r^e}{\rho_c} \iint_\triangle \varphi_q^e \varphi_p^e dS \qquad (2.26)$$

where $i, j, p, q = \{1, 2, 3\}$ are the matrix indices.

Details of the evaluations of the matrix elements are given in Appendix B.

The local matrix entries are then assembled over the whole solution domain to obtain the overall matrix formed as a generalized eigenvalue problem to solve for the eigenvalues k_0^2

$$\mathbf{S} \left[\begin{array}{c} E_t \\ e_\phi \end{array} \right] = k_0^2 \mathbf{M} \left[\begin{array}{c} E_t \\ e_\phi \end{array} \right] \tag{2.27}$$

The above problem is solved with the structure and mesh in Figure 2.10. The radius, thickness and material of the grounded resonator are $a = 5mm$, $b = 1mm$ and $\varepsilon_r = 14.8$, respectively. We set the azimuthal revolution number $n = 10$ to assemble matrices $\mathbf{S}$ and $\mathbf{M}$. The resonance frequency of the $WGH_{10,1,0}$ mode solved from the eigenvalue problem is 38.342GHz and its field distribution is shown in Figure 2.11.
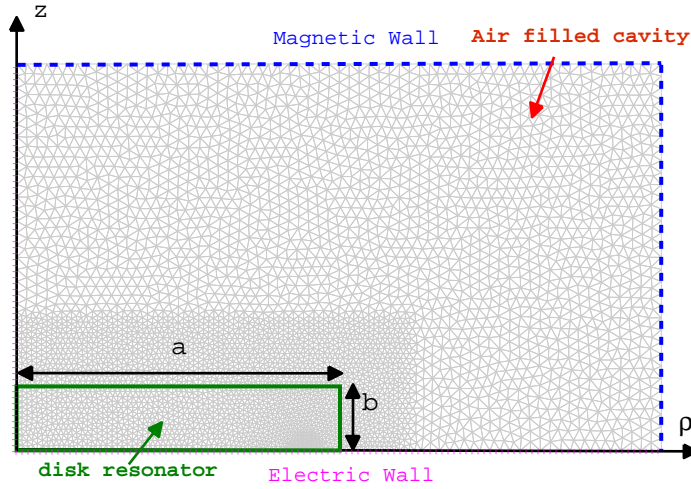
Figure 2.10: Solution mesh of the dielectric disk resonator ($\varepsilon_r = 14.8$) inside a cavity with $a = 5mm$, $b = 1mm$

19
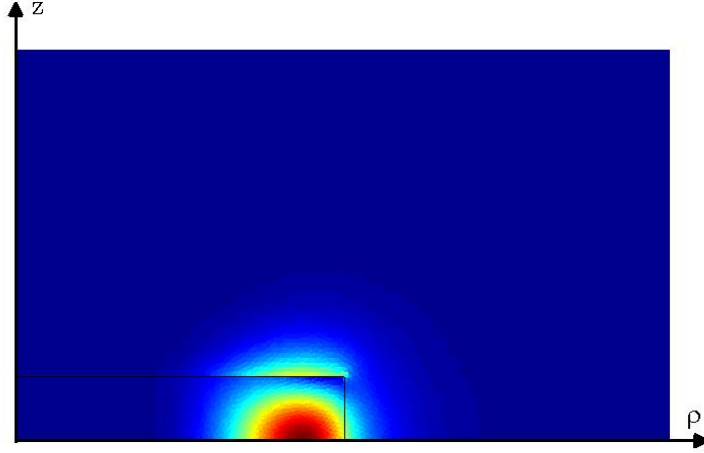
Figure 2.11: $\overrightarrow{E}_t$ field plot of the $WGH_{10,1,0}$ mode for the disk resonator ($\varepsilon_r = 14.8$) shown in Figure 2.10.

2.4 Quality Factor Analysis

The quality factor of the resonator at the resonance frequency is of primary importance to many application such as filter and dielectric characterization. The DWM is not only good for estimating the resonance frequency but also predicting the fields inside and outside the resonator except in those corner region, which is similar to the limitation of Marcatili's method [53]. If the mode fields are strongly confined inside the resonator which is the case for WGMs, the fields in the corner region (region 5 in Figure 2.12) can be neglected and set to zero. We will use a method based on the DWM shown in the previous section and perturbation analysis to find an analytical expression for the quality factor of an axially two-layered WGM resonator shown in Figure 2.5. The cross-section of the resonator is divided into several region to express the field separately (Figure 2.12).

The quality factor calculation of the resonator is based the perturbation method that is using the lossless field distribution to estimate the losses. The unloaded quality factor of an isolated resonator can be expressed as [43]

$$Q_u^{-1} = \sum_i p_{ei} tan\delta_i + Q_c^{-1} + Q_r^{-1} \tag{2.28}$$

where p_{ei} is the electric energy filling factor for region i, and it's defined as $p_{ei} = \frac{W_{ei}}{W_e}$, where $W_e = \sum_i W_{ei}$ is the total stored electric energy in the whole resonator. Q_r is the radiation quality factor accounting for the intrinsic radiation loss; Q_c is the portion accounting for conduction loss. They are defined as

$$Q_r^{-1} = \frac{P_r}{2\omega_0 W_e} \tag{2.29}$$

$$Q_c^{-1} = \frac{P_c}{2\omega_0 W_e} \tag{2.30}$$

$$P_c = \frac{R_s}{2} \iint_S \overrightarrow{H_t} \cdot \overrightarrow{H_t^*} dS \tag{2.31}$$

P_r is the radiation power and $\overrightarrow{H_t}$ is the tangential magnetic fields over the surface S of the conductor with a surface resistance $R_s = \sqrt{\frac{\omega_0 \mu_0}{2\sigma}}$.

In order to find Q_u by (2.28), W_e, P_c and P_r are addressed sequentially in the following subsections 2.4.1, 2.4.2 and 2.4.3, respectively.

2.4.1   Stored Electric Energies
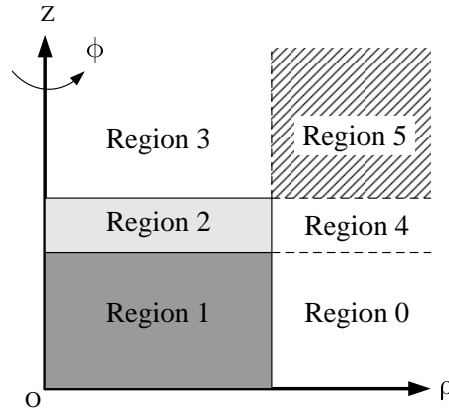
Figure 2.12: Geometry and region divisions of a cross-section of axially double-layered WGM resonator. The structure is rotationally symmetric along ϕ.

In order to find the stored electric energies defined as

$$W_e = \frac{1}{4} \iiint_V \varepsilon |E|^2 \, dV$$

we need to know the electric field in each region except region 5 in Figure 2.12. The electric field in region 1, 0, 2 and 3 can be expressed as

Region #1

$$
\begin{cases}
E_{z1}(\rho,\phi,z) & = A_{n1}J_n(k_{\rho1}\rho)e^{jn\phi}\cos\left(k_{z1}z\right) = E^c_{z1}(\rho,\phi)\cos\left(k_{z1}z\right) \\
E_{\rho1}(\rho,\phi,z) & = -\frac{j}{k^2_{\rho1}}\left[-jk_{z1}k_{\rho1}A_{n1}J'_n(k_{\rho1}\rho) + \frac{k_0\eta_0 n}{\rho}B_{n1}J_n(k_{\rho1}\rho)\right]e^{jn\phi}\sin\left(k_{z1}z\right) \\
& = E^c_{\rho1}(\rho,\phi)\sin\left(k_{z1}z\right) \\
E_{\phi1}(\rho,\phi,z) & = -\frac{j}{k^2_{\rho1}}\left[\frac{k_{z1}n}{\rho}A_{n1}J_n(k_{\rho1}\rho) + jk_0\eta_0 k_{\rho1}B_{n1}J'_n(k_{\rho1}\rho)\right]e^{jn\phi}\sin\left(k_{z1}z\right) \\
& = E^c_{\phi1}(\rho,\phi)\sin\left(k_{z1}z\right)
\end{cases}
$$

$$\text{(2.32)}$$

Region #0

$$
\begin{cases}
E_{z0}(\rho,\phi,z) & = C_{n1}K_n(\alpha_\rho\rho)e^{jn\phi}\cos\left(k_{z1}z\right) = E^c_{z0}(\rho,\phi)\cos\left(k_{z1}z\right) \\
E_{\rho0}(\rho,\phi,z) & = \frac{j}{\alpha^2_\rho}\left[-jk_{z1}\alpha_\rho C_{n1}K'_n(\alpha_\rho\rho) + \frac{k_0\eta_0 n}{\rho}D_{n1}K_n(\alpha_\rho\rho)\right]e^{jn\phi}\sin\left(k_{z1}z\right) \\
& = E^c_{\rho0}(\rho,\phi)\sin\left(k_{z1}z\right) \\
E_{\phi0}(\rho,\phi,z) & = \frac{j}{\alpha^2_\rho}\left[\frac{k_{z1}n}{\rho}C_{n1}K_n(\alpha_\rho\rho) + jk_0\eta_0\alpha_\rho D_{n1}K'_n(\alpha_\rho\rho)\right]e^{jn\phi}\sin\left(k_{z1}z\right) \\
& = E^c_{\phi0}(\rho,\phi)\sin\left(k_{z1}z\right)
\end{cases}
$$

$$\text{(2.33)}$$

Region #2

$$
\begin{cases}
E_{z2}(\rho,\phi,z) & = A_{n2}J_n(k_{\rho1}\rho)e^{jn\phi}\left[e^{-\alpha_{z2}(z-b)} + E_{n2}e^{\alpha_{z2}(z-b)}\right] \\
& = E^c_{z2}(\rho,\phi)\left[e^{-\alpha_{z2}(z-b)} + E_{n2}e^{\alpha_{z2}(z-b)}\right] \\
E_{\rho2}(\rho,\phi,z) & = \frac{1}{k^2_{\rho1}}\left[-\alpha_{z2}k_{\rho1}A_{n2}J'_n(k_{\rho1}\rho) + \frac{k_0\eta_0 n}{\rho}B_{n2}J_n(k_{\rho1}\rho)\right] \\
& \times e^{jn\phi}\left[e^{-\alpha_{z2}(z-b)} - E_{n2}e^{\alpha_{z2}(z-b)}\right] \\
& = E^c_{\rho2}(\rho,\phi)\left[e^{-\alpha_{z2}(z-b)} - E_{n2}e^{\alpha_{z2}(z-b)}\right] \\
E_{\phi2}(\rho,\phi,z) & = \frac{1}{k^2_{\rho1}}\left[\frac{\alpha_{z2}n}{j\rho}A_{n2}J_n(k_{\rho1}\rho) + jk_0\eta_0 k_{\rho1}B_{n2}J'_n(k_{\rho1}\rho)\right] \\
& \times e^{jn\phi}\left[e^{-\alpha_{z2}(z-b)} - E_{n2}e^{\alpha_{z2}(z-b)}\right] \\
& = E^c_{\phi2}(\rho,\phi)\left[e^{-\alpha_{z2}(z-b)} - E_{n2}e^{\alpha_{z2}(z-b)}\right]
\end{cases}
$$

$$\text{(2.34)}$$

Region #3

$$
\begin{cases}
E_{z3}(\rho, \phi, z) &= A_{n3} J_n(k_{\rho 1}\rho) e^{jn\phi} e^{-\alpha_{z3}(z-b-h)} \\
&= E_{z3}^c(\rho, \phi) e^{-\alpha_{z3}(z-b-h)} \\
E_{\rho 3}(\rho, \phi, z) &= \frac{1}{k_{\rho 1}^2} \left[-\alpha_{z3} k_{\rho 1} A_{n3} J_n'(k_{\rho 1}\rho) + \frac{k_0 \eta_0 n}{\rho} B_{n3} J_n(k_{\rho 1}\rho) \right] e^{jn\phi} e^{-\alpha_{z3}(z-b-h)} \\
&= E_{\rho 3}^c(\rho, \phi) e^{-\alpha_{z3}(z-b-h)} \\
E_{\phi 3}(\rho, \phi, z) &= \frac{1}{k_{\rho 1}^2} \left[\frac{\alpha_{z3} n}{j\rho} A_{n3} J_n(k_{\rho 1}\rho) + j k_0 \eta_0 k_{\rho 1} B_{n3} J'_n(k_{\rho 1}\rho) \right] e^{jn\phi} e^{-\alpha_{z3}(z-b-h)} \\
&= E_{\phi 3}^c(\rho, \phi) e^{-\alpha_{z3}(z-b-h)}
\end{cases}
$$

$$(2.35)$$

Applying the boundary conditions that enforce the continuities of tangential electric and magnetic fields on each interface normal to $\hat{\rho}$, we can express B_{ni}, C_{ni}, and D_{ni} in terms of A_{ni} [61],

$$
B_{n1} = -\frac{n k_{z1}}{j k_0 \eta_0} \frac{\left(\frac{1}{u^2} + \frac{1}{v^2}\right)}{\left[\frac{J_n'(u)}{u J_n(u)} + \frac{K_n'(v)}{v K_n(v)}\right]} A_{n1} = \frac{j k_{z1}}{k_0 \eta_0} s_n A_{n1} \tag{2.36}
$$

$$
B_{n2,3} = \frac{\alpha_{z2,3}}{k_0 \eta_0} s_n A_{n2,3} \tag{2.37}
$$

$$
C_{ni} = \frac{J_n(u)}{K_n(v)} A_{ni} \tag{2.38}
$$

$$
D_{ni} = \frac{J_n(u)}{K_n(v)} B_{ni} \tag{2.39}
$$

where we define

$$
u = k_{\rho 1} a \tag{2.40}
$$

$$
v = \alpha_\rho a \tag{2.41}
$$

$$
s_n = n \left(\frac{1}{u^2} + \frac{1}{v^2}\right) \left[\frac{J_n'(u)}{u J_n(u)} + \frac{K_n'(v)}{v K_n(v)}\right]^{-1} \tag{2.42}
$$

Substituting Equations (2.37-2.42) and the recurrence relation in (A.1-A.4) into Equations (2.32-2.35), we can rewrite the radial parts of electric fields as

$$
\begin{cases}
E_{z1}^c(\rho, \phi) &= A_{n1} J_n(k_{\rho1}\rho)e^{jn\phi} \\
E_{\rho1}^c(\rho, \phi) &= -\frac{k_{z1}}{2k_{\rho1}} A_{n1} \left[(1 - s_n) J_{n-1}(k_{\rho1}\rho) - (1 + s_n) J_{n+1}(k_{\rho1}\rho) \right] e^{jn\phi} \\
E_{\phi1}^c(\rho, \phi) &= -\frac{jk_{z1}}{2k_{\rho1}} A_{n1} \left[(1 - s_n) J_{n-1}(k_{\rho1}\rho) + (1 + s_n) J_{n+1}(k_{\rho1}\rho) \right] e^{jn\phi}
\end{cases} \quad (2.43)
$$

$$
\begin{cases}
E_{z0}^c(\rho, \phi) &= A_{n1} \frac{J_n(u)}{K_n(v)} K_n(k_{\rho1}\rho)e^{jn\phi} \\
E_{\rho0}^c(\rho, \phi) &= -\frac{k_{z1}}{2\alpha_\rho} \frac{J_n(u)}{K_n(v)} A_n \left[(1 - s_n) K_{n-1}(\alpha_\rho\rho) + (1 + s_n) K_{n+1}(\alpha_\rho\rho) \right] e^{jn\phi} \\
E_{\phi0}^c(\rho, \phi) &= -\frac{jk_{z1}}{2\alpha_\rho} \frac{J_n(u)}{K_n(v)} A_n \left[(1 - s_n) K_{n-1}(\alpha_\rho\rho) - (1 + s_n) K_{n+1}(\alpha_\rho\rho) \right] e^{jn\phi}
\end{cases}
$$
$$(2.44)$$

$$
\begin{cases}
E_{z2}^c(\rho, \phi) &= A_{n2} J_n(k_{\rho1}\rho)e^{jn\phi} \\
E_{\rho2}^c(\rho, \phi) &= -\frac{\alpha_{z2}}{2k_{\rho1}} A_{n2} \left[(1 - s_n) J_{n-1}(k_{\rho1}\rho) - (1 + s_n) J_{n+1}(k_{\rho1}\rho) \right] e^{jn\phi} \\
E_{\phi2}^c(\rho, \phi) &= -\frac{j\alpha_{z2}}{2k_{\rho1}} A_{n2} \left[(1 - s_n) J_{n-1}(k_{\rho1}\rho) + (1 + s_n) J_{n+1}(k_{\rho1}\rho) \right] e^{jn\phi}
\end{cases} \quad (2.45)
$$

$$
\begin{cases}
E_{z3}^c(\rho, \phi) &= A_{n3} J_n(k_{\rho1}\rho)e^{jn\phi} \\
E_{\rho3}^c(\rho, \phi) &= -\frac{\alpha_{z3}}{2k_{\rho1}} A_{n3} \left[(1 - s_n) J_{n-1}(k_{\rho1}\rho) - (1 + s_n) J_{n+1}(k_{\rho1}\rho) \right] e^{jn\phi} \\
E_{\phi3}^c(\rho, \phi) &= -\frac{j\alpha_{z3}}{2k_{\rho1}} A_{n3} \left[(1 - s_n) J_{n-1}(k_{\rho1}\rho) + (1 + s_n) J_{n+1}(k_{\rho1}\rho) \right] e^{jn\phi}
\end{cases} \quad (2.46)
$$

Similarly, applying the boundary conditions on each interface normal to $\hat{z}$, the unknown A_{n2}, E_{n2} and A_{n3} can be related to A_{n1}

$$
\begin{cases}
\varepsilon_{r2} A_{n2} (1 + E_{n2}) &= \varepsilon_{r1} A_{n1} \cos(k_{z1}b) \\
A_{n2}\alpha_{z2} (1 - E_{n2}) &= A_{n1} k_{z1} \sin(k_{z1}b)
\end{cases}
$$
$$
\Rightarrow
\begin{cases}
E_{n2} &= \frac{\varepsilon_{r1}\alpha_{z2} - \varepsilon_{r2}k_{z1}\tan(k_{z1}b)}{\varepsilon_{r1}\alpha_{z2} + \varepsilon_{r2}k_{z1}\tan(k_{z1}b)} \\
A_{n2} &= \frac{A_{n1}}{2} \left[\frac{\varepsilon_{r1}}{\varepsilon_{r2}} \cos(k_{z1}b) + \frac{k_{z1}}{\alpha_{z2}} \sin(k_{z1}b) \right]
\end{cases} \quad (2.47)
$$

$$
\begin{aligned}
A_{n3} &= \varepsilon_{r2} A_{n2} \left(e^{-\alpha_{z2}h} + E_{n2}e^{\alpha_{z2}h} \right) \\
&= \frac{\varepsilon_{r2}}{2} \left[\frac{\varepsilon_{r1}}{\varepsilon_{r2}} \cos(k_{z1}b) + \frac{k_{z1}}{\alpha_{z2}} \sin(k_{z1}b) \right] \\
&\quad \times \left[e^{-\alpha_{z2}h} + \frac{\varepsilon_{r1}\alpha_{z2} - \varepsilon_{r2}k_{z1}\tan(k_{z1}b)}{\varepsilon_{r1}\alpha_{z2} + \varepsilon_{r2}k_{z1}\tan(k_{z1}b)} e^{\alpha_{z2}h} \right] A_{n1}
\end{aligned} \quad (2.48)
$$

Having $\overrightarrow{E_i^c} = \begin{bmatrix} E_{\rho i}^c \hat{\rho} & E_{\phi i}^c \hat{\phi} & E_{zi}^c \hat{z} \end{bmatrix}$, the stored electric energy in region 1 can be expressed as

$$
\begin{aligned}
W_{e1} &= \frac{1}{4} \int_0^a \int_0^b \int_0^{2\pi} \varepsilon(\rho, \phi, z) \left| \overrightarrow{E_1}(\rho, \phi, z) \right|^2 \rho \, d\rho \, d\phi \, dz \\
&= \frac{\pi}{2} \varepsilon_0 \varepsilon_{r1} \int_0^a \left[\left| E_{z1}^c \right|^2 \int_0^b \cos^2(k_{z1}z) \, dz + \left| E_{\rho 1}^c \right|^2 \int_0^b \sin^2(k_{z1}z) \, dz \right. \\
&\quad \left. + \left| E_{\phi 1}^c \right|^2 \int_0^b \sin^2(k_{z1}z) \, dz \right] \rho \, d\rho \qquad\qquad (2.49) \\
&= \frac{\pi \varepsilon_0 \varepsilon_{r1}}{2} \left[P_{z1c} \left| E_{z1}^c \right|^2 + P_{z1s} \left| E_{\rho 1}^c \right|^2 + P_{z1s} \left| E_{\phi 1}^c \right|^2 \right] \rho \, d\rho \\
&= \frac{\pi \varepsilon_0 \varepsilon_{r1}}{2} |A_{n1}|^2 \int_0^a \left[P_{z1c} J_n^2(k_{\rho 1}\rho) + 2P_{z1s} \frac{k_{z1}^2}{4k_{\rho 1}^2} (1-s_n)^2 J_{n-1}^2(k_{\rho 1}\rho) \right. \\
&\quad \left. + 2P_{z1s} \frac{k_{z1}^2}{4k_{\rho 1}^2} (1+s_n)^2 J_{n+1}^2(k_{\rho 1}\rho) \right] \rho \, d\rho \qquad\qquad (2.50)
\end{aligned}
$$

where

$$
P_{z1c} = \int_0^b \cos^2(k_{z1}z) \, dz = \frac{b}{2} + \frac{\sin(2k_{z1}b)}{4k_{z1}} \qquad\qquad (2.51)
$$

$$
P_{z1s} = \int_0^b \sin^2(k_{z1}z) \, dz = \frac{b}{2} - \frac{\sin(2k_{z1}b)}{4k_{z1}} \qquad\qquad (2.52)
$$

Similarly, stored electric energy in region 0 is

$$
\begin{aligned}
W_{e0} &= \frac{1}{4} \int_a^\infty \int_0^b \int_0^{2\pi} \varepsilon(\rho, \phi, z) \left| \overrightarrow{E_0}(\rho, \phi, z) \right|^2 \rho \, d\rho \, d\phi \, dz \\
&= \frac{\pi \varepsilon_0}{2} \int_a^\infty \left[P_{z0c} \left| E_{z0}^c \right|^2 + P_{z0s} \left| E_{\rho 0}^c \right|^2 + P_{z0s} \left| E_{\phi 0}^c \right|^2 \right] \rho \, d\rho \\
&= \frac{\pi \varepsilon_0}{2} \frac{J_n^2(u)}{K_n^2(v)} |A_n|^2 \int_a^\infty \left[P_{z1c} K_n^2(\alpha_\rho \rho) + 2P_{z1s} \frac{k_{z1}^2}{4\alpha_\rho^2} (1-s_n)^2 K_{n-1}^2(\alpha_\rho \rho) \right. \\
&\quad \left. + 2P_{z1s} \frac{k_{z1}^2}{4\alpha_\rho^2} (1+s_n)^2 K_{n+1}^2(\alpha_\rho \rho) \right] \rho \, d\rho \qquad\qquad (2.53)
\end{aligned}
$$

where we use the definition and integral identities (A.7) and (A.10)

$$
\begin{aligned}
P_{J,n} &= \int_0^a J_n^2(k_{\rho 1}\rho)\rho \, d\rho \\
&= \frac{a^2}{2}\left[J_n^2(k_{\rho 1}a) - J_{n-1}(k_{\rho 1}a)J_{n+1}(k_{\rho 1}a)\right] \quad (n \geq 1) \quad (2.54) \\
P_{K,n} &= \int_a^\infty K_n^2(\alpha_\rho \rho)\rho \, d\rho \\
&= \frac{a^2}{2}\left[K_{n-1}(\alpha_\rho a)K_{n+1}(\alpha_\rho a) - K_n^2(\alpha_\rho a)\right] \quad (n \geq 1) \quad (2.55)
\end{aligned}
$$

$$
\tilde{P}_{J,n} = \left(P_{J,n-1}(1-s_n)^2 + P_{J,n+1}(1+s_n)^2\right)/2 \quad (2.56)
$$

$$
\tilde{P}_{K,n} = \left(P_{K,n-1}(1-s_n)^2 + P_{K,n+1}(1+s_n)^2\right)/2 \quad (2.57)
$$

W_{e1} and W_{e0} can be further simplified

$$
W_{e1} = \frac{\pi \varepsilon_0 \varepsilon_{r1}}{2}|A_{n1}|^2 \left[P_{z1c}P_{J,n} + \frac{k_{z1}^2}{k_{\rho 1}^2}P_{z1s}\tilde{P}_{J,n}\right] \quad (2.58)
$$

$$
W_{e0} = \frac{\pi \varepsilon_0}{2}\frac{J_n^2(u)}{K_n^2(v)}|A_{n1}|^2 \left[P_{z1c}P_{K,n} + \frac{k_{z1}^2}{\alpha_\rho^2}P_{z1s}\tilde{P}_{K,n}\right] \quad (2.59)
$$

From (2.47) and (2.48) , $|A_{n2}|^2$ and $|A_{n3}|^2$ can be expressed as

$$
|A_{n2}|^2 = \frac{1}{4}\left[\frac{\varepsilon_{r1}}{\varepsilon_{r2}}\cos\left(k_{z1}b\right) + \frac{k_{z1}}{\alpha_{z2}}\sin\left(k_{z1}b\right)\right]^2 |A_{n1}|^2 \quad (2.60)
$$

$$
|A_{n3}|^2 = \frac{\varepsilon_{r2}^2}{4}\left[\frac{\varepsilon_{r1}}{\varepsilon_{r2}}\cos\left(k_{z1}b\right) + \frac{k_{z1}}{\alpha_{z2}}\sin\left(k_{z1}b\right)\right]^2 \left[e^{-2\alpha_{z2}h} + E_{n2}^2 e^{2\alpha_{z2}h} + 2E_{n2}\right]|A_{n1}|^2 \\
(2.61)
$$

Furthermore, we define the following integrals as P_{z2c} and P_{z2s}

$$
\begin{aligned}
P_{z2c} &= \int_b^{b+h}\left|e^{-\alpha_{z2}(z-b)} + E_{n2}e^{\alpha_{z2}(z-b)}\right|^2 dz \\
&= \frac{1}{2\alpha_{z2}}\left[E_{n2}^2 e^{2\alpha_{z2}h} - e^{-2\alpha_{z2}h} + 1 - E_{n2}^2\right] + 2E_{n2}h \quad (2.62)
\end{aligned}
$$

26

$$
\begin{aligned}
P_{z2s} &= \int_b^{b+h} \left| e^{-jk_{z2}(z-b)} - E_{n2}e^{jk_{z2}(z-b)} \right|^2 dz \\
&= \frac{1}{2\alpha_{z2}} \left[E_{n2}^2 e^{2\alpha_{z2}h} - e^{-2\alpha_{z2}h} + 1 - E_{n2}^2 \right] - 2E_{n2}h \quad (2.63)
\end{aligned}
$$

$$
P_{z3} = \int_{b+h}^{\infty} e^{-2\alpha_{z3}(z-b-h)}dz = \frac{1}{2\alpha_{z3}} \quad (2.64)
$$

Following the similar approach, the stored electric energy in region 2 is

$$
\begin{aligned}
W_{e2} &= \frac{1}{4} \int_0^a \int_b^{b+h} \int_0^{2\pi} \varepsilon(\rho, \phi, z) \left| \overrightarrow{E_1}(\rho, \phi, z) \right|^2 \rho d\rho d\phi dz \\
&= \frac{\pi}{2} \varepsilon_0 \varepsilon_{r2} \int_0^a \left[|E_{z2}^c|^2 \int_b^{b+h} \left| e^{-\alpha_{z2}(z-b)} + E_{n2}e^{\alpha_{z2}(z-b)} \right|^2 dz \right. \\
&\quad + \left. \left(|E_{\rho2}^c|^2 + |E_{\phi2}^c|^2 \right) \int_b^{b+h} \left| e^{-\alpha_{z2}(z-b)} - E_{n2}e^{\alpha_{z2}(z-b)} \right|^2 dz \right] \rho d\rho \\
&= \frac{\pi \varepsilon_0 \varepsilon_{r2}}{2} \int_0^a \left[P_{z2c} |E_{z2}^c|^2 + P_{z2s} |E_{\rho2}^c|^2 + P_{z2s} |E_{\phi2}^c|^2 \right] \rho d\rho \\
&= \frac{\pi \varepsilon_0 \varepsilon_{r2}}{2} |A_{n2}|^2 \left[P_{z2c} P_{J,n} + \frac{\alpha_{z2}^2}{k_{\rho1}^2} P_{z2s} \tilde{P}_{J,n} \right] \quad (2.65)
\end{aligned}
$$

$$
(2.66)
$$

The stored electric energy in region 3 is

$$
\begin{aligned}
W_{e3} &= \frac{1}{4} \int_0^a \int_{b+h}^{\infty} \int_0^{2\pi} \varepsilon(\rho, \phi, z) \left| \overrightarrow{E_3}(\rho, \phi, z) \right|^2 \rho d\rho d\phi dz \\
&= \frac{\pi}{2} \varepsilon_0 \int_0^a \left(|E_{z3}^c|^2 + |E_{\rho3}^c|^2 + |E_{\phi3}^c|^2 \right) \rho d\rho \int_{b+h}^{\infty} e^{-2\alpha_{z3}(z-b-h)} dz \\
&= \frac{\pi \varepsilon_0}{2} P_{z3} \int_b^{b+h} \left[|E_{z2}^c|^2 + |E_{\rho2}^c|^2 + |E_{\phi2}^c|^2 \right] \rho d\rho \\
&= \frac{\pi \varepsilon_0}{2} |A_{n3}|^2 P_{z3} \left[P_{J,n} + \frac{\alpha_{z3}^2}{k_{\rho1}^2} \tilde{P}_{J,n} \right] \quad (2.67)
\end{aligned}
$$

$$
(2.68)
$$

With the availability of W_e and dielectric loss tangent in each region, the first term in Equation (2.28) is found.

2.4.2 Evaluation of the Conduction Loss

Assuming the only existing metallic surface is the ground plane (plane $z = 0$), we will find the H fields over the plane and substitute them into (2.31).

The magnetic fields H over the ground plane are:

In region #1

$$
\begin{cases}
H_{\rho 1}(\rho, \phi, z = 0) & = \frac{1}{k_{\rho 1}^2} \left[-\frac{k_0 \varepsilon_{1r} n}{\eta_0 \rho} A_{n1} J_n(k_{\rho 1}\rho) - j k_{z1} k_{\rho 1} B_{n1} J_n'(k_{\rho 1}\rho) \right] e^{jn\phi} \\
H_{\phi 1}(\rho, \phi, z = 0) & = \frac{1}{k_{\rho 1}^2} \left[-\frac{j k_{\rho 1} k_0 \varepsilon_{1r}}{\eta_0} A_{n1} J_n'(k_{\rho 1}\rho) + \frac{k_{z1} n}{\rho} B_{n1} J_n(k_{\rho 1}\rho) \right] e^{jn\phi}
\end{cases}
\tag{2.69}
$$

In region #2

$$
\begin{cases}
H_{\rho 0}(\rho, \phi, z = 0) & = -\frac{1}{\alpha_\rho^2} \left[-\frac{k_0 n}{\eta_0 \rho} C_{n1} J_n(k_{\rho 1}\rho) - j k_{z1} \alpha_\rho D_{n1} J_n'(k_{\rho 1}\rho) \right] e^{jn\phi} \\
H_{\phi 0}(\rho, \phi, z = 0) & = -\frac{1}{\alpha_\rho^2} \left[-\frac{j \alpha_\rho k_0}{\eta_0} C_{n1} J_n'(k_{\rho 1}\rho) + \frac{k_{z1} n}{\rho} D_{n1} J_n(k_{\rho 1}\rho) \right] e^{jn\phi}
\end{cases}
\tag{2.70}
$$

Defining

$$
s_{n0} = \frac{k_{z1}^2}{k_0^2} s_n
\tag{2.71}
$$

$$
s_{n1} = \frac{k_{z1}^2}{\varepsilon_{r1} k_0^2} s_n
\tag{2.72}
$$

Substituting (2.36), (2.38), (2.39), (2.71) and (2.72) into (2.69) and (2.70), we get

$$
\begin{cases}
H_{\rho 1}(\rho, \phi, z = 0) & = -\frac{k_0 \varepsilon_{1r}}{2 k_{\rho 1} \eta_0} A_{n1} \left[(1 - s_{n1}) J_{n-1}(k_{\rho 1}\rho) + (1 + s_{n1}) J_{n+1}(k_{\rho 1}\rho) \right] e^{jn\phi} \\
H_{\phi 1}(\rho, \phi, z = 0) & = -\frac{j k_0 \varepsilon_{1r}}{2 k_{\rho 1} \eta_0} A_{n1} \left[(1 - s_{n1}) J_{n-1}(k_{\rho 1}\rho) - (1 + s_{n1}) J_{n+1}(k_{\rho 1}\rho) \right] e^{jn\phi}
\end{cases}
\tag{2.73}
$$

$$
\begin{cases}
H_{\rho 0}(\rho, \phi, z = 0) & = \frac{k_0}{2 \alpha_\rho \eta_0} \frac{J_n(u)}{K_n(v)} A_{n1} \\
& \quad \times \left[(1 - s_{n0}) K_{n-1}(k_{\rho 1}\rho) + (1 + s_{n0}) K_{n+1}(k_{\rho 1}\rho) \right] e^{jn\phi} \\
H_{\phi 0}(\rho, \phi, z = 0) & = \frac{j k_0}{2 \alpha_\rho \eta_0} \frac{J_n(u)}{K_n(v)} A_{n1} \\
& \quad \times \left[(1 - s_{n0}) K_{n-1}(k_{\rho 1}\rho) - (1 + s_{n0}) K_{n+1}(k_{\rho 1}\rho) \right] e^{jn\phi}
\end{cases}
\tag{2.74}
$$

Therefore, the conduction loss will be

$$
\begin{aligned}
P_c &= \frac{R_s}{2} \iint_{S_1} \overrightarrow{H_t} \cdot \overrightarrow{H_t^*} dS + \frac{R_s}{2} \iint_{S_0} \overrightarrow{H_t} \cdot \overrightarrow{H_t^*} dS \\
&= \frac{R_s}{2} \int_0^a \int_0^{2\pi} \left(\left| H_{\rho 1} \right|^2 + \left| H_{\phi 1} \right|^2 \right) \rho d\rho d\phi + \frac{R_s}{2} \int_a^\infty \int_0^{2\pi} \left(\left| H_{\rho 0} \right|^2 + \left| H_{\phi 0} \right|^2 \right) \rho d\rho d\phi \\
&= \frac{\pi R_s k_0^2}{\eta_0^2} \left(\frac{\varepsilon_{1r}^2}{k_{\rho 1}^2} \tilde{P}_{J1,n} + \frac{J_n^2(u)}{\alpha_\rho^2 K_n^2(v)} \tilde{P}_{K0,n} \right) |A_{n1}|^2
\end{aligned}
$$

where we define

$$
\tilde{P}_{J1,n} = \left(P_{J,n-1}(1 - s_{n1})^2 + P_{J,n+1}(1 + s_{n1})^2 \right)/2 \tag{2.75}
$$

$$
\tilde{P}_{K0,n} = \left(P_{K,n-1}(1 - s_{n0})^2 + P_{K,n+1}(1 + s_{n0})^2 \right)/2 \tag{2.76}
$$

Conduction quality factors of the $WGH_{n,1,0}$ modes in a grounded single-layered disk resonator are calculated and compared with results from HFSS eigenmode solver in Figure 2.13. For this graph, the resonator parameters are $a = 5mm$, $b = 1mm$, $\varepsilon_r = 14.8$ and the ground plate is made of copper ($\sigma = 5.8 \times 10^7 S \cdot m^{-1}$) . The discrepancies between the two results are due to the inaccuracies in field intensities predicted by the DWM.
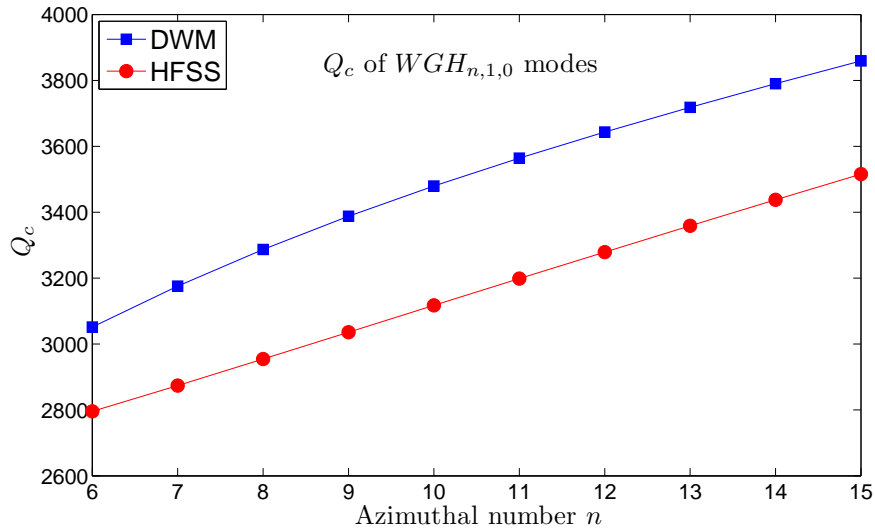
Figure 2.13: Conduction quality factor Q_c varying with n for a disk resonator grounded by copper plate.

2.4.3   Evaluation of the Radiation Loss

An open resonator, even though made of lossless material, will have complex resonance frequencies. This is due to the intrinsic radiation loss of the open resonator. To address this loss, equivalent volume polarization current is applied to find the radiation power [27]. Equivalent volume polarization current is also widely used in formulating volume integral equation for dielectric scattering problems [70], waveguide bend loss [45], radiation quality factor of spherical WGM resonator [51] , and radiation of dielectric antennas [44, 84]. DWM gives a good estimation of internal fields of $WGH_{n,1,0}$ mode and hence the equivalent polarization current $\overrightarrow{J}_v = j\omega\varepsilon_0\left(\varepsilon_{r1} - 1\right)\overrightarrow{E}$ (Figure 2.14). We will revisit and use this method to analyze the radiation from dielectric rod antenna in the Chapter 3.
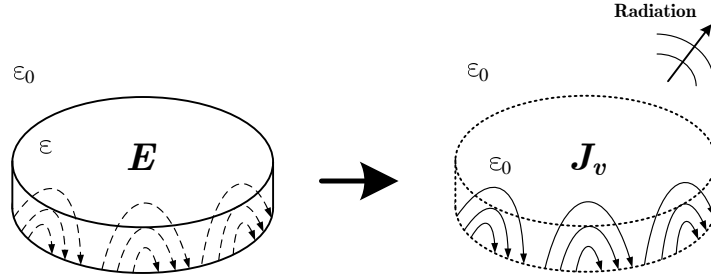
Figure 2.14: Illustration of Volume Current Method.

The magnetic vector potential in the far field is found by integration of equivalent volume current source. Furthermore, applying the image method (for a grounded disk) and paraxial approximation, we have

$$
\begin{aligned}
\overrightarrow{A}(\overrightarrow{r}_0) &= 2\iiint \frac{\mu_0\overrightarrow{J}_v(\overrightarrow{r}')e^{-jk_0R}}{4\pi R}dV' \\
&\simeq \int_0^b dz'\frac{\mu_0 e^{-jk_0 r_0}}{2\pi r_0}\int_0^a\int_0^{2\pi}\overrightarrow{J}_v(\rho',\phi',z') \\
&\qquad \exp\left[jk_0\rho'\sin\theta_0\cos\left(\phi' - \phi_0\right)\right]\rho' d\rho' d\phi'
\end{aligned}
\qquad (2.77)
$$

where $\vec{r}_0 = \{r_0, \theta_0, \phi_0\}$ (spherical coordinate) is the far field observation point.

Here, we further approximate the equivalent volume current $\overrightarrow{J}_v$ as $j\omega\varepsilon_0\left(\varepsilon_{r1} - 1\right)\overrightarrow{E}_z$ and neglect the minor components generated by $\overrightarrow{E}_\phi$ and $\overrightarrow{E}_\rho$. The resulting magnetic vector potential will have only vector component long $\hat{z}$.

$$
\begin{aligned}
\vec{A}(\vec{r}_0) &= \hat{z}j\omega\varepsilon_0\mu_0\left(\varepsilon_{r1}-1\right)\frac{e^{-jk_0r_0}}{2\pi r_0}\frac{\sin\left(k_{z1}b\right)}{k_{z1}}A_{n1} \\
&\quad \times \int_0^a \int_0^{2\pi} J_n(k_{\rho1}\rho')e^{jn\phi'}\exp\left[jk_0\rho'\sin\theta_0\cos\left(\phi'-\phi_0\right)\right]\rho'd\rho'd\phi' \\
&= \hat{z}j^{(n+1)}\omega\varepsilon_0\mu_0\left(\varepsilon_{r1}-1\right)\frac{e^{-jk_0r_0}}{r_0}\frac{\sin\left(k_{z1}b\right)}{k_{z1}}A_{n1}e^{jn\phi_0} \\
&\quad \times \int_0^a J_n\left(k_{\rho1}\rho'\right)J_n\left(k_0\sin\theta_0\rho'\right)\rho'd\rho' \\
&= \hat{z}j^{(n+1)}\omega\varepsilon_0\mu_0\left(\varepsilon_{r1}-1\right)\frac{e^{-jk_0r_0}}{r_0}\frac{\sin\left(k_{z1}b\right)}{k_{z1}}A_{n1}I_{Jn}e^{jn\phi_0}
\end{aligned}
$$

where we use the identities (A.5) and (A.9)

$$
\begin{aligned}
&\int_0^{2\pi} e^{jn\phi'}\exp\left[jk_0\rho'\sin\theta_0\cos\left(\phi'-\phi_0\right)\right]d\phi' \\
&= e^{jn\phi_0}2\pi j^n J_n\left(k_0\sin\theta_0\rho'\right)
\end{aligned}
$$

$$
\begin{aligned}
I_{Jn}\left(\theta_0\right) &= \int_0^a J_n\left(k_{\rho1}\rho'\right)J_n\left(k_0\sin\theta_0\rho'\right)\rho'd\rho' \\
&= \frac{a}{k_0^2\sin^2\theta_0-k_{\rho1}^2}\left[k_0\sin\theta_0 J_n(k_{\rho1}a)J_{n+1}(k_0\sin\theta_0 a)\right. \\
&\quad \left.-k_{\rho1}J_{n+1}(k_{\rho1}a)J_n(k_0\sin\theta_0 a)\right]
\end{aligned}
\tag{2.78}
$$

Total radiation power is the integration of radiation intensities over a semi-sphere (considering a grounded disk)

$$
\begin{aligned}
P_r &= \frac{\omega^2}{2\eta_0}\int_0^{\frac{\pi}{2}}\int_0^{2\pi} r_0^2\left|A_\theta\right|^2\sin\theta_0 d\theta_0 d\phi_0 \\
&= \frac{\omega^2}{2\eta_0}\int_0^{\frac{\pi}{2}}\int_0^{2\pi} r_0^2\left|A_z\right|^2\sin^3\theta_0 d\theta_0 d\phi_0 \\
&= \frac{k_0^4\pi}{2k_{z1}^2\eta_0}\left(\varepsilon_{r1}-1\right)^2\sin^2\left(k_{z1}b\right)\int_0^{\frac{\pi}{2}} I_{Jn}^2\left(\theta_0\right)\sin^3\theta_0 d\theta_0
\end{aligned}
$$

The integration $\int_0^{\frac{\pi}{2}} I_{Jn}^2\left(\theta_0\right)\sin^3\theta_0 d\theta_0$ is carried out numerically.

In Figure 2.16, the radiation quality factors with different n are calculated for a sample resonator grounded with perfect electric conductor (PEC). The same set of resonator parameters as those in Figure 2.13 are used. The results are also compared with HFSS eigenmode results and Q_r from the complex resonance frequencies of 2D $WGH_{n,1}$ modes in a cylinder with the same material and radius as the 3D resonator. These resonance frequencies are complex roots of Equation (2.4) [69, 57, 29]. Q_r^{2D} of these 2D WGH modes are defined as

$$Q_r^{2D} = \left| \frac{Re(k_0)}{2Im(k_0)} \right| \tag{2.79}$$
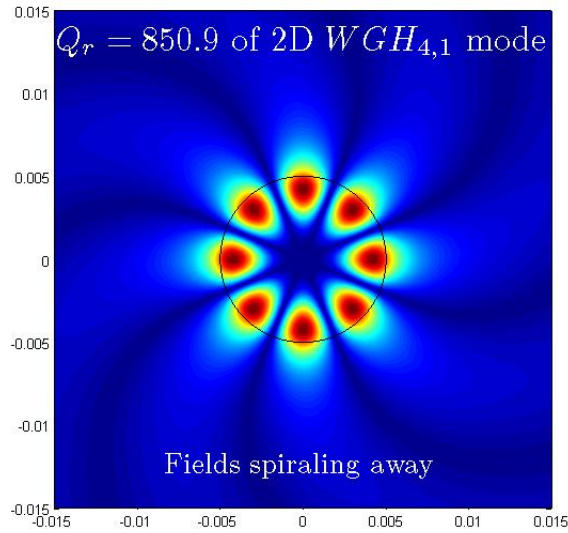
Figure 2.15: Field magnitude plot of 2D $WGH_{4,1}$ mode ($f = 15.63 + j9.18 \times 10^{-4}GHz$) in cylinder with a radius $a = 5mm$ and $\varepsilon_r = 14.8$.

where k_0 is the complex resonance frequencies solved from the dispersion equation (2.4). As an example shown in Figure 2.15, the complex resonance frequency of 2D $WGH_{4,1}$ is solved to be $f = 15.63 + j9.18 \times 10^{-4}GHz$ with $Q_r^{2D} = 850.9$ by Equation (2.79). Moreover, Figure 2.15 shows the leaky E_z fields are spiraling away from the resonator and this is their leaky mechanism [57]. Although solved from leaky resonator mode in 2D, Q_r^{2D} are still comparable in scale with Q_r estimated from volume current method. Therefore, Q_r^{2D} can be used as a quick reference to estimate Q_r. HFSS results show some discrepancies compared with the former two data points. These discrepancies, which awaits further investigation, may be caused by the insufficient meshes used in HFSS to capture the correct field behavior especially with a large n.
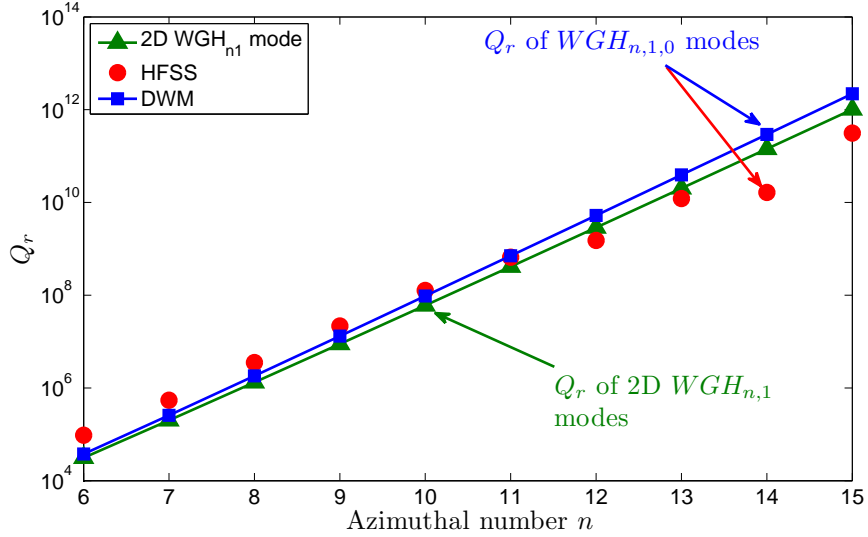
Figure 2.16: Radiation quality factor Q_r varying with n for a disk resonator grounded with PEC.

$\tan \delta_2$	0.1	0.01	0.001	0.0001
Q_d	255	2090	7473	10064
Q_u	238	1319	2419	2638

Table 2.1: Quality factors of $WGM_{10,1,0}$ mode in an axially double-layered resonator with $a = 5mm$, $b = 1mm$, $h = 4mm$, $\varepsilon_r = 14.8$, $\tan \delta_1 = 0.0001$ and $\varepsilon_{r1} = 2.33$.

2.4.4 Results

In Table 2.1, the quality factors Q_d owing to the dielectric loss and Q_u are listed for different loss tangents in region 2. The dielectric constant and loss tangent of the material in Region 1 are $\varepsilon_r = 14.8$ and $\tan \delta_1 = 0.0001$, respectively. These are calculated for the $WGM_{10,1,0}$ mode in an axially double-layered resonator with $a = 5mm$, $b = 1mm$ and $h = 4mm$ as shown in Figure 2.10. In Region 2, the dielectric constant ε_{r1} is 2.33 and the loss tangent is $\tan \delta_2$. The energy filling factors which is calculated based on the lossless fields are

$$p_{e1} = 0.9553 \quad p_{e2} = 0.0383$$

The radiation quality factor Q_r is 4.76×10^{12} and the conduction loss quality factor Q_c is 3575.8 owing to the finite conductivity $5.8 \times 10^7 S \cdot m^{-1}$ of the ground plane. It is observed that at mmW range of frequencies, the dielectric loss is much larger than the radiation loss in an isolated resonant.

33

2.5 Waveguide-Disk Resonator Coupling
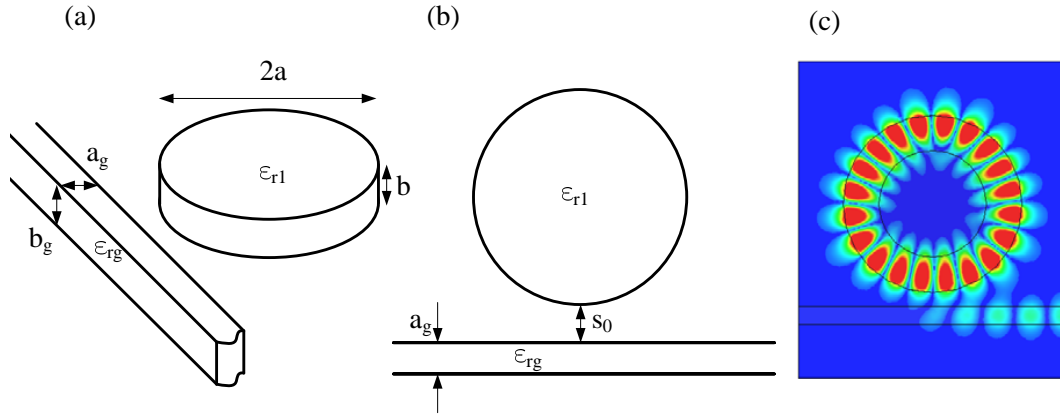
Figure 2.17: Geometry of waveguide-disk coupling: (a) Perspective view; (b) Top view; (c) A near critical-coupling field plot.

Coupled mode theory [51] is successfully applied to estimate the coupling between a rectangular core dielectric waveguide and a WGM disk resonator (Figure 2.17). In this context, WGM resonator can be viewed as curved waveguide with joint ends. Mode $WGM_{n,1,0}$ with phase variation $e^{-jn\phi}$ can be considered as a traveling wave with propagation constant n/R_n where R_n is the bent radius of the effective waveguide. Therefore, the coupling is between the dielectric waveguide and effective WGM waveguide. CMT assumes that the total field of the whole coupled system is direct superposition of the fields of these two isolated waveguides. The calculation needs to be done with the knowledge of normalized fields of isolated waveguides. Field expressions of a stand-alone WGM disk resonator and a dielectric waveguide are detailed in the following sections and each of them is normalized to carry unit propagation power.

2.5.1 Fields of the Grounded Dielectric Disk Resonator

A cross-sectional graph of a disk resonator is illustrated in Figure 2.18. Similar to the former section, fields in each region are listed below. Other than the E field, H field expressions are also required for power normalization.

Fields in Region #1
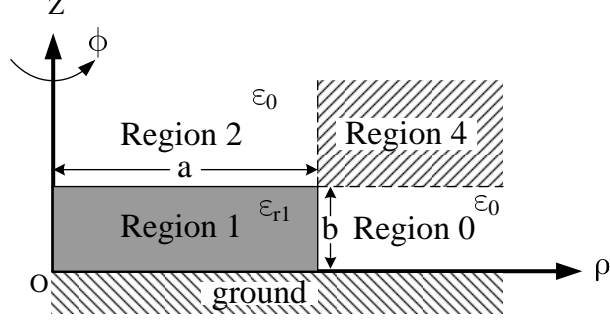
Figure 2.18: Geometry and region divisions of a cross-section of grounded disk WGM resonator. The structure is rotationally symmetric along ϕ.

$$\begin{cases} E_{z1}(\rho, \phi, z) &= A_{n1} J_n(k_{\rho 1}\rho) e^{-jn\phi} \cos\left(k_{z1} z\right) \\ E_{\rho 1}(\rho, \phi, z) &= -\frac{j}{k_{\rho 1}^2}\left[-jk_{z1}k_{\rho 1}A_{n1}J_n'(k_{\rho 1}\rho) + \frac{k_0\eta_0 n}{\rho}B_{n1}J_n(k_{\rho 1}\rho)\right]e^{-jn\phi}\sin\left(k_{z1}z\right) \\ E_{\phi 1}(\rho, \phi, z) &= \frac{j}{k_{\rho 1}^2}\left[\frac{k_{z1}n}{\rho}A_{n1}J_n(k_{\rho 1}\rho) + jk_0\eta_0 k_{\rho 1}B_{n1}J_n'(k_{\rho 1}\rho)\right]e^{-jn\phi}\sin\left(k_{z1}z\right) \\ H_{z1}(\rho, \phi, z) &= jB_{n1}J_n(k_{\rho 1}\rho)e^{-jn\phi}\sin\left(k_{z1}z\right) \\ H_{\rho 1}(\rho, \phi, z) &= -\frac{1}{k_{\rho 1}^2}\left[-\frac{k_0\varepsilon_{r1}n}{\rho\eta_0}A_{n1}J_n(k_{\rho 1}\rho) - jk_{z1}k_{\rho 1}B_{n1}J_n'(k_{\rho 1}\rho)\right]e^{-jn\phi}\cos\left(k_{z1}z\right) \\ H_{\phi 1}(\rho, \phi, z) &= \frac{1}{k_{\rho 1}^2}\left[-\frac{jk_0\varepsilon_{r1}k_{\rho 1}}{\eta_0}A_{n1}J_n'(k_{\rho 1}\rho) + \frac{k_{z1}n}{\rho}B_{n1}J_n(k_{\rho 1}\rho)\right]e^{-jn\phi}\cos\left(k_{z1}z\right) \end{cases}$$

$$(2.80)$$

Fields in Region #0

$$\begin{cases} E_{z0}(\rho, \phi, z) &= A_{n1}\frac{J_n(u)}{K_n(v)}K_n(\alpha_\rho\rho)e^{-jn\phi}\cos\left(k_{z1}z\right) \\ E_{\rho 0}(\rho, \phi, z) &= \frac{j}{\alpha_\rho^2}\frac{J_n(u)}{K_n(v)}\left[-jk_{z1}\alpha_\rho A_{n1}K_n'(\alpha_\rho\rho) + \frac{k_0\eta_0 n}{\rho}B_{n1}K_n(\alpha_\rho\rho)\right]e^{-jn\phi}\sin\left(k_{z1}z\right) \\ E_{\phi 0}(\rho, \phi, z) &= -\frac{j}{\alpha_\rho^2}\frac{J_n(u)}{K_n(v)}\left[\frac{k_{z1}n}{\rho}A_{n1}K_n(\alpha_\rho\rho) + jk_0\eta_0\alpha_\rho B_{n1}K_n'(\alpha_\rho\rho)\right]e^{-jn\phi}\sin\left(k_{z1}z\right) \\ H_{z0}(\rho, \phi, z) &= j\frac{J_n(u)}{K_n(v)}B_{n1}K_n(\alpha_\rho\rho)e^{-jn\phi}\sin\left(k_{z1}z\right) \\ H_{\rho 0}(\rho, \phi, z) &= \frac{1}{\alpha_\rho^2}\frac{J_n(u)}{K_n(v)}\left[-\frac{k_0 n}{\rho\eta_0}A_{n1}K_n(\alpha_\rho\rho) - jk_{z1}\alpha_\rho B_{n1}K_n'(\alpha_\rho\rho)\right]e^{-jn\phi}\cos\left(k_{z1}z\right) \\ H_{\phi 0}(\rho, \phi, z) &= -\frac{1}{\alpha_\rho^2}\frac{J_n(u)}{K_n(v)}\left[-\frac{jk_0\alpha_\rho}{\eta_0}A_{n1}K_n'(\alpha_\rho\rho) + \frac{k_{z1}n}{\rho}B_{n1}K_n(\alpha_\rho\rho)\right]e^{-jn\phi}\cos\left(k_{z1}z\right) \end{cases}$$

$$(2.81)$$

Fields in Region #2

$$
\begin{cases}
E_{z2}(\rho,\phi,z) &= A_{n2}J_n(k_{\rho1}\rho)e^{-jn\phi}e^{-\alpha_{z2}(z-b)} \\[4pt]
E_{\rho2}(\rho,\phi,z) &= \frac{1}{k_{\rho1}^2}\left[-\alpha_{z2}k_{\rho1}A_{n2}J_n'(k_{\rho1}\rho) + \frac{k_0\eta_0 n}{\rho}B_{n2}J_n(k_{\rho1}\rho)\right]e^{-jn\phi}e^{-\alpha_{z2}(z-b)} \\[4pt]
E_{\phi2}(\rho,\phi,z) &= -\frac{1}{k_{\rho1}^2}\left[\frac{\alpha_{z2}n}{j\rho}A_{n2}J_n(k_{\rho1}\rho) + jk_0\eta_0 k_{\rho1}B_{n2}J_n'(k_{\rho1}\rho)\right]e^{-jn\phi}e^{-\alpha_{z2}(z-b)} \\[4pt]
H_{z2}(\rho,\phi,z) &= -B_{n2}J_n(k_{\rho2}\rho)e^{-jn\phi}e^{-\alpha_{z2}(z-b)} \\[4pt]
H_{\rho2}(\rho,\phi,z) &= -\frac{1}{k_{\rho1}^2}\left[-\frac{k_0\varepsilon_{r2}n}{\rho\eta_0}A_{n2}J_n(k_{\rho1}\rho) - \alpha_{z2}k_{\rho1}B_{n2}J_n'(k_{\rho1}\rho)\right]e^{-jn\phi}e^{-\alpha_{z2}(z-b)} \\[4pt]
H_{\phi2}(\rho,\phi,z) &= \frac{1}{k_{\rho1}^2}\left[-\frac{jk_0\varepsilon_{r2}k_{\rho1}}{\eta_0}A_{n2}J_n'(k_{\rho1}\rho) + \frac{\alpha_{z2}n}{j\rho}B_{n2}J_n(k_{\rho1}\rho)\right]e^{-jn\phi}e^{-\alpha_{z2}(z-b)}
\end{cases}
$$

$$(2.82)$$

where we define

$$
B_{n1} = -\frac{nk_{z1}}{jk_0\eta_0}\frac{\left(\frac{1}{u^2}+\frac{1}{v^2}\right)}{\left[\frac{J_n'(u)}{uJ_n(u)} + \frac{K_n'(v)}{vK_n(v)}\right]}A_{n1} = \frac{jk_{z1}}{k_0\eta_0}s_nA_{n1} \qquad (2.83)
$$

$$
B_{n2} = \frac{\alpha_{z2}}{k_0\eta_0}s_nA_{n2}
$$

$$
A_{n2} = \frac{\varepsilon_{r1}}{\varepsilon_{r2}}A_{n1}\cos\left(k_{z1}b\right)
$$

By solving the dispersion equation 2.10 for k_{z1} and resonant wave number k_0, the field expressions (2.80,2.81,2.82,2.83) are known. Variations of fields along axis ρ are shown in Figure 2.19 where the field dependence along z is removed by dividing them by $\sin(k_{1z}z)$ or $\cos(k_{1z}z)$, and H fields are scaled by η_0 for a better view. A two dimensional plot of the E_z fields over the resonator cross-section is shown in Figure 2.20. Discrepancies of fields can be observed by comparing the FEM simulation and analytical result. The DWM overestimates the k_z and underestimates k_ρ and hence the resonator frequency. For the figure, the resonator parameters are chose as: $n = 10$, $a = 5mm$, $b = 1mm$, $\varepsilon_{r1} = 14.8$ and $\varepsilon_{r2} = 1$. The f_r calculated by DWM for $WGM_{10,1,0}$ of this resonator is $37.83GHz$.
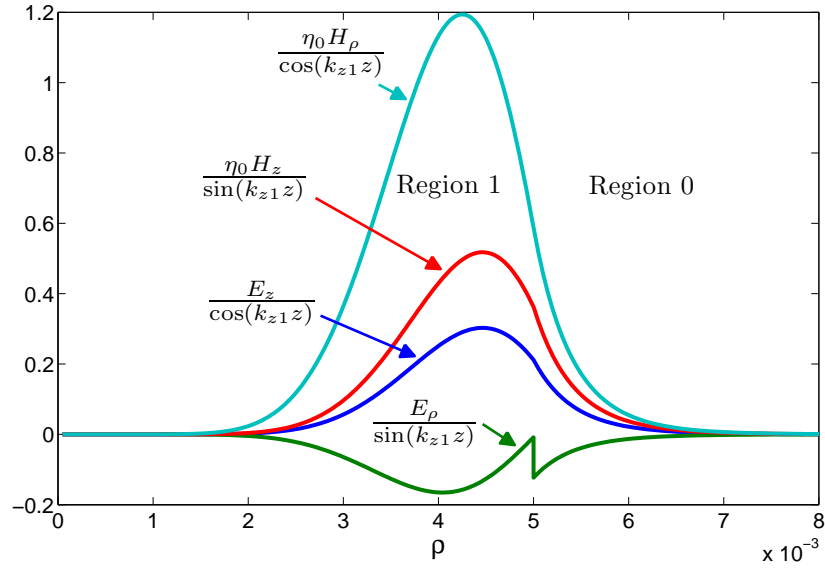
Figure 2.19: Plot of E and H fields of $WGH_{10,1,0}$ as a function of ρ across region 1 and 2. Resonator parameters are $a = 5mm$, $b = 1mm$, $\varepsilon_{r1} = 14.8$ and $\varepsilon_{r2} = 1$.
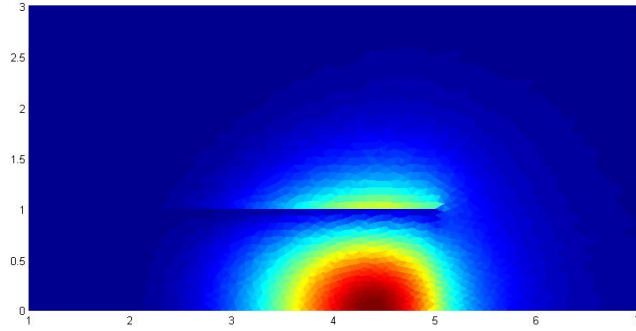
(a)
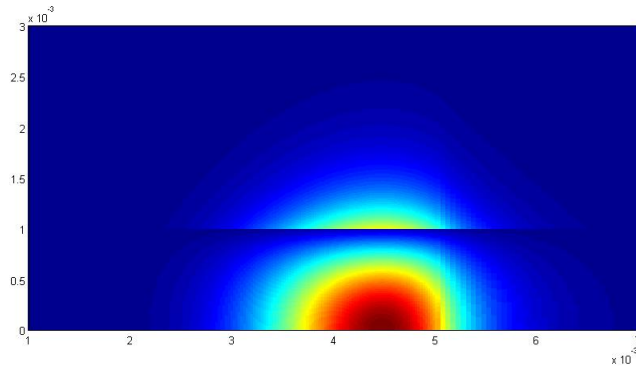
(b)

Figure 2.20: Plot of E_z of $WGH_{10,1,0}$ over the cross-section of the disk resonator: (a) FEM-BOR simulation; (b) DWM. Resonator parameters are $a = 5mm$, $b = 1mm$, $\varepsilon_{r1} = 14.8$ and $\varepsilon_{r2} = 1$.

The power carried by the mode is evaluated by integrating the Poynting vector along ϕ over the $\rho - z$ plane

$$
\begin{aligned}
P_r &= \int_{S_0+S_1+S_2+S_3} S_\phi ds \\
&= \sum P_i
\end{aligned}
$$

$$
S_\phi = \frac{1}{2}\hat{\phi} \cdot \left(\overrightarrow{E} \times \overrightarrow{H^*}\right) = \frac{1}{2}\left(E_z H_\rho^* - E_\rho H_z^*\right) \tag{2.84}
$$

By setting A_{n1} to 1 and integrating S_ϕ along z, Figure 2.21 plots values related to parts of S_ϕ along ρ. The resonator parameters are chose as that in Figure 2.19. It is clearly seen that in S_ϕ, the major part is $\frac{1}{2}E_z H_\rho^*$ and the minor part is $\frac{1}{2}E_\rho H_z^*$ which is smaller but not negligible. This further demonstrates the hybrid mode nature of WGM. Finally, it is noted that the major term of $\frac{1}{2}E_z H_\rho^*$ in region 1 is proportional to $J_n^2(k_{\rho 1})/\rho$ which is confirmed in [5].
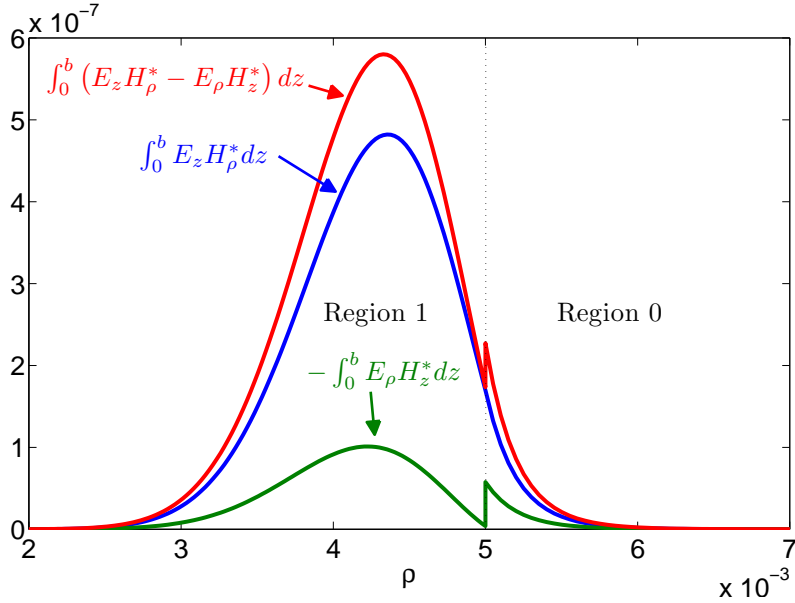
Figure 2.21: Plot of $WGH_{10,1,0}$ functions related to power flux integrated along z. Resonator parameters are $a = 5mm$, $b = 1mm$, $\varepsilon_{r1} = 14.8$ and $\varepsilon_{r2} = 1$.

Therefore, we have

$$
\begin{aligned}
P_1 &= \int_{S_1} S_\phi ds \\
&= \frac{A_{n1}^2}{2k_{\rho 1}^2 \eta_0}\left[n\left(k_0 \varepsilon_{r1} P_{z1c} + \frac{k_{z1}^2 s_n^2}{k_0} P_{z1s}\right) P_{Js} - \frac{k_{z1}^2 s_n}{2k_0} J_n^2(u)b\right]
\end{aligned}
$$

Note that the value of second term in $P1$ is smaller than the value of the first term. P_{z1c} and P_{z1s} are defined by Equation (2.51,2.52).

$$P_0 = \int_{S_0} S_\phi ds$$

$$= \frac{A_{n1}^2}{2\alpha_\rho^2 \eta_0} \frac{J_n^2(u)}{K_n^2(v)} \left[-n \left(k_0 P_{z1c} + \frac{k_{z1}^2 s_n^2}{k_0} P_{z1s} \right) P_{Ks} - \frac{k_{z1}^2 s_n}{2k_0} K_n^2(v) b \right]$$

where we define P_{z1c}(2.51), P_{z1s}(2.52) and

$$P_{Js} = \int_0^a \frac{J_n^2(k_{\rho 1}\rho)}{\rho} d\rho$$

$$P_{Ks} = \int_a^\infty \frac{K_n^2(\alpha_\rho \rho)}{\rho} d\rho$$

Similarly, power in Region 2 and 3 are founded as

$$P_2 = \int_{S_2} S_\phi ds = \frac{A_{n1}^2 \cos^2(k_{z1}b) \varepsilon_{r1}^2 n}{2k_{\rho 1}^2 \varepsilon_{r2}^2 \eta_0} \left(k_0 \varepsilon_{r2} + \frac{\alpha_{z2}^2 s_n^2}{k_0} \right) P_{Js} P_{z2}$$

$$P_{z2} = \int_b^\infty e^{-2\alpha_{z2}(z-b)} dz = \frac{1}{2\alpha_{z2}} \tag{2.85}$$

Power flow in Region 3 is neglected.

Therefore, A_{n1}^2 is normalized to make $P_r = 1$.

2.5.2 Fields of the Rectangular Image Guide
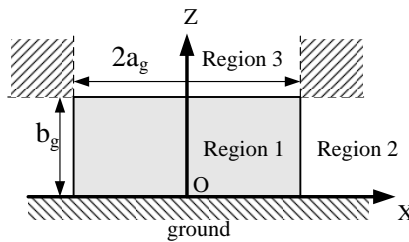
Figure 2.22: Geometry of the rectangular dielectric waveguide.

We will assume $|E_z| \gg |E_x|$ for the E_z^{11} mode in the rectangular image guide shown in Figure 2.22. The field components and propagation constant of this mode are calculated by Marcatili's approximation [53, 61].

$$H_{gx} = \begin{cases} A_g \cos\left(k_{gx}x\right)\cos\left(k_{gy}y\right) \\ A_g \cos\left(k_{gx}a_g\right)\cos\left(k_{gz}z\right)e^{-\alpha_{gx}(x-a_g)} \\ A_g \cos\left(k_{gx}x\right)\cos\left(k_{gz}b_g\right)e^{-\alpha_{gz}(z-b_g)} \end{cases} \quad E_{gz} = \begin{cases} \frac{\omega\mu_0}{\beta_g}H_{gx} & \cdots \text{Region 1} \\ \frac{\omega\mu_0}{\beta_g}H_{gx} & \cdots \text{Region 2} \\ \frac{\omega\mu_0\varepsilon_{rg}}{\beta_g}H_{gx} & \cdots \text{Region 3} \end{cases}$$

and the electric field is $E_{gz} \simeq \frac{\omega\mu_0}{\beta_g}H_{gx}$, and β_g is the propagation constant of this mode

The power carried by this E_z^{11} mode is

$$P_g = \frac{\omega\mu_0}{4\beta_g}|A_g|^2\left(a_g + \frac{1}{\alpha_{gx}}\right)\left(b_g + \frac{1}{\alpha_{gy}}\right)$$

To normalize the mode, A_g is taken as $\left[\frac{\omega\mu_0}{4\beta_g}\left(a + \frac{1}{\alpha_{gx}}\right)\left(b + \frac{1}{\alpha_{gy}}\right)\right]^{-\frac{1}{2}}$.

2.5.3 Coupled Mode Theory for the Resonator - Image Guide Coupling
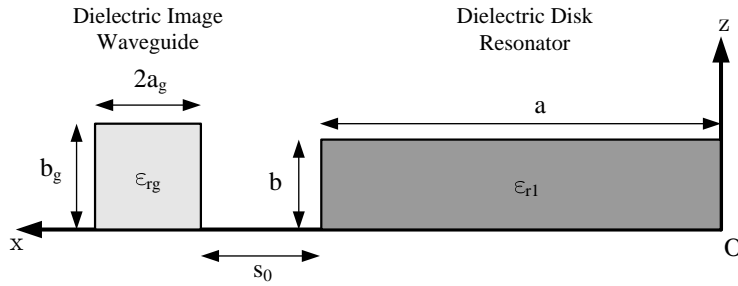
Figure 2.23: Cross-sectional view of a waveguide resonator coupled structure
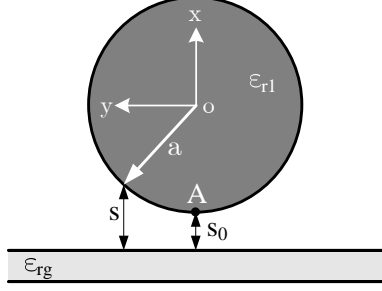
Figure 2.24: Top view of a waveguide resonator coupled structure: definition of s

The mode coupling coefficient of a transverse cut (Figure 2.23) with the waveguide-resonator spacing s is

$$\kappa\left(s\right) = \frac{\omega\varepsilon_0}{4}\int_{S_r}\left(\varepsilon_{r1} - 1\right)E_{rz}E_{gz}^*ds$$

The integration is done over the cross-sectional surface S_r inside the resonator. E_{rz} and E_{gz} are fields of a stand-alone resonator and dielectric waveguide respectively.

By substituting the field expressions, $\kappa\left(s\right)$ is evaluated to be

$$\kappa\left(s\right) = \frac{k_0^2}{4\beta_g}\left(\varepsilon_{r1} - 1\right)A_{n1}A_g\cos\left(k_{gx}a_g\right)e^{-\alpha_{gx}(s+a)}K_{zr}K_{xr} \qquad (2.86)$$

where K_{zr} and K_{xr} are results of sub-integrals

$$K_{zr} = \frac{1}{2}\left[\frac{\sin\left(\left(k_{gz} + k_{z1}\right)b\right)}{k_{gz} + k_{z1}} + \frac{\sin\left(\left(k_{gz} - k_{z1}\right)b\right)}{k_{gz} - k_{z1}}\right]$$

$$K_{xr} = \int_0^a J_n(k_{\rho1}x)e^{\alpha_{gx}x}dx$$

After knowing the coupling strengths $\kappa\left(s\right)$ over each cross-section of the structure, the net coupling coefficient is calculated by performing an integration over the whole space, which is defined as

$$\kappa = \int_{-\infty}^{\infty}\kappa\left(s\right)e^{-j\triangle\beta y}dy \qquad (2.87)$$

$$\triangle\beta = \frac{n}{R_n} - \beta_g$$

$\triangle\beta$ is the difference of the propagation constants of traveling waves in the waveguide and the resonator. The effective wave propagation constant of $WGH_{n,1,0}$ in the resonator is denoted as $\beta_r = \frac{n}{R_n}$. R_n can be approximated as [69]

$$R_n = \frac{\int_0^a J_n^2(k_{\rho 1}\rho)d\rho}{\int_0^a \frac{J_n^2(k_{\rho 1}\rho)}{\rho}d\rho}$$

In the case when n is large, the radial field maxima of $WGH_{n,1,0}$ is squeezed to the boundary of the resonator, and R_n can be well approximated as a.

The coupling intensity is localized near the point A in Figure 2.24 where the spacing s between the resonator and the waveguide is minimum. And $\kappa(s)$ decays fast with an increasing s. Resulting from this, $\kappa(s)$ can be written as a function of $\kappa(s_0)$ by approximating the circular curvature of resonator as parabolic around point A (Figure 2.24). That is, the spacing s is written as

$$\begin{aligned} s &= s_0 + a - \sqrt{a^2 - y^2} \\ &\simeq s_0 + \gamma y^2 \end{aligned} \tag{2.88}$$

$$\gamma = \frac{1}{2a}$$

where a is the radius of the curvature of the resonator boundary.

Using this approximation, we have

$$\kappa(s) = \kappa(s_0)\exp\left(-\alpha_{gx}\gamma y^2\right) \tag{2.89}$$

Substituting Equation (2.89) into (2.87), we can obtain the net coupling coefficient in closed form

$$\kappa = \kappa(s_0)\exp\left(-\frac{a\triangle\beta^2}{2\alpha_{gx}}\right)\sqrt{\frac{2\pi a}{\alpha_{gx}}} \tag{2.90}$$

by using following integral identity

$$\int_{-\infty}^{\infty} \exp\left(-p^2x^2 \pm qx\right)dx = \exp\left(\frac{q^2}{4p^2}\right)\frac{\sqrt{\pi}}{|p|}$$

Figure 2.25 shows the calculated κ^2 decaying exponential with respect to the increasing distance of separation s_0. The decaying constant is $-2\alpha_{gx}$. The external coupling quality factor are shown to be [51]

$$Q_e = \frac{2n\pi}{\kappa^2} \qquad (2.91)$$

The external quality factors are also extracted from HFSS and are compared with CMT results in Figure 2.27. A good agreement is observed. In HFSS simulations, the external-Q is estimated by

$$Q_e = \left(Q_t^{-1} - Q_u^{-1}\right)^{-1} \qquad (2.92)$$

where Q_u is the unloaded quality factor of an isolated resonator calculated in previous sections, and Q_t is the total quality factor calculated from the transmission response of the two-port system as shown in Figure 2.28 [35]. The critical coupling (zero transmission to the output at resonance) of the resonator-waveguide coupling system occurs when

$$Q_e = Q_u = 2Q_t \qquad (2.93)$$

which means the external coupling loss equals to the internal loss of the resonator [23, 35, 15].
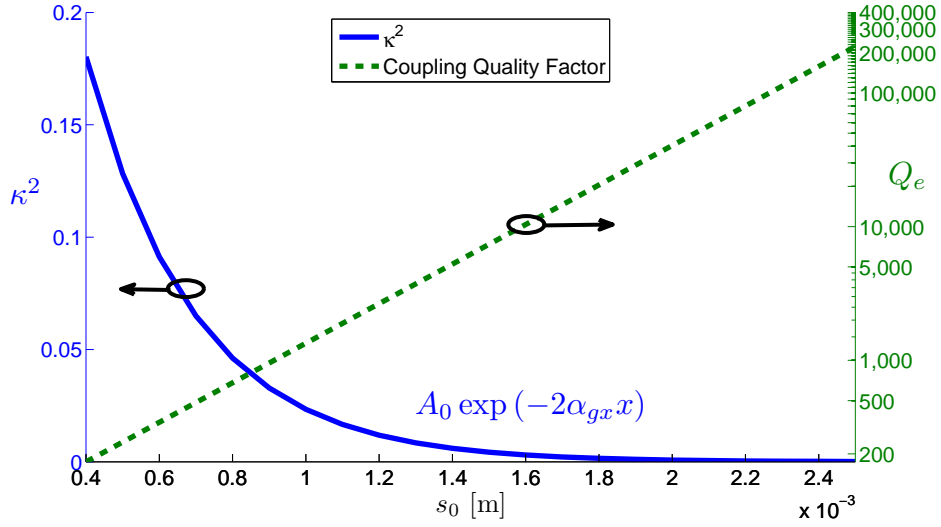
Figure 2.25: Plot of κ^2 of $WGM_{10,1,0}$ as a function of WG-Resonator separation s_0. The geometry and material parameters are $a_g = 0.5mm$, $b_g = 2mm$, $\varepsilon_{rg} = 9.8$, $a = 5mm$, $b = 1mm$, $\varepsilon_{r1} = 14.8$ and $\varepsilon_{r2} = 1$. The resulting curve from CMT is exponentially decaying with constant $-2\alpha_{gx}$ which is evident from Equation (2.86).
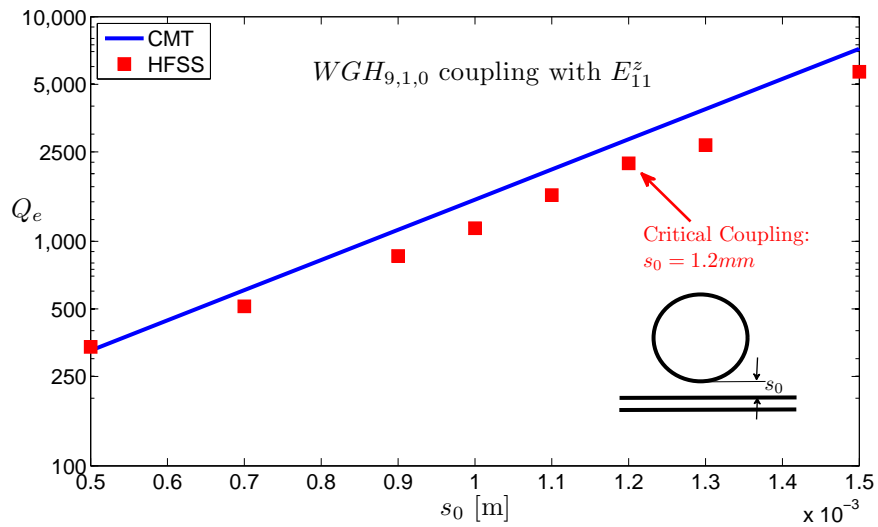
Figure 2.26: Plot of Q_e of $WGH_{9,1,0}$ as a function of the separation s_0. The same configuration as that in Figure 2.25 is investigated.
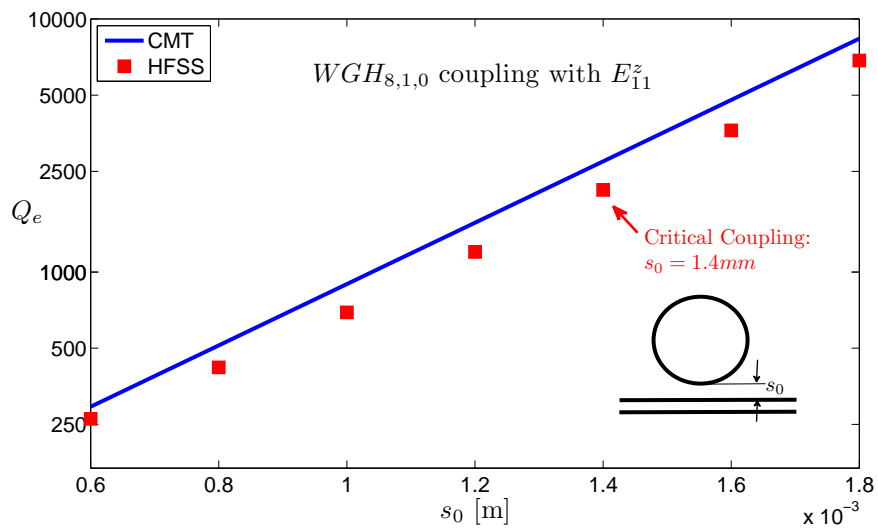
Figure 2.27: Plot of Q_e of $WGH_{8,1,0}$ as a function of the separation s_0. The same configuration as that in Figure 2.25 is investigated.
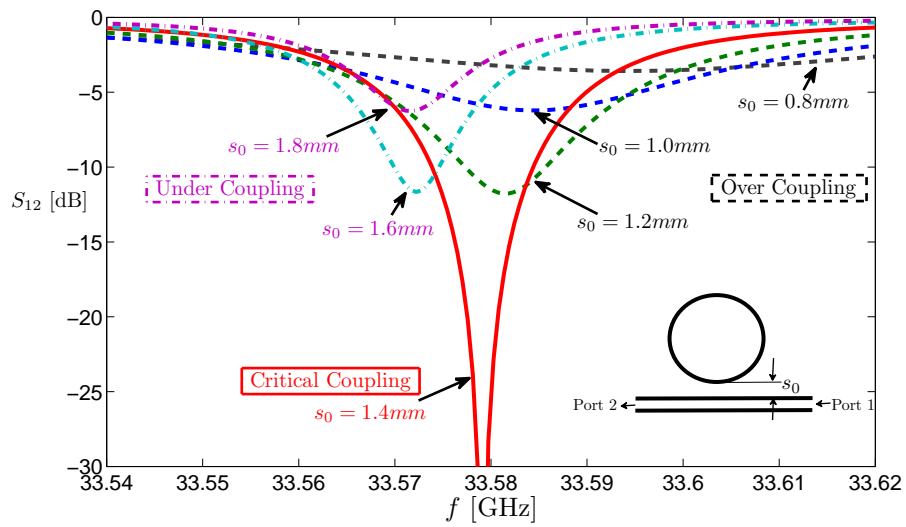
Figure 2.28: Simulated transmission responses of $WGH_{8,1,0}$ coupling with E^z_{11} mode in a image guide. The same configuration as that in Figure 2.25 is investigated.

Chapter 3

Tapered Dielectric Rod Antenna Analysis and Design

3.1 Introduction

Dielectric rod antennas, the end-fired surface-wave antennas, have been known for a long time [58, 71, 91, 72]. They radiate by converting guided waves into free space propagating waves. These rod antennas can have different shapes and feeding schemes. The most popular cross-sections of the dielectric rod antennas are rectangular [73, 40] and circular [85, 38, 76, 2, 33, 19]. Also, rods with a variety of tip profiles have been designed such as the original uniform rod [76, 3], the most popular tapered rod [40] and many other profiles [38]. Furthermore, a number of transitions have been proposed to excite the rod antenna. These excitations can be a monopole probe [71], metallic waveguides [85], horns [80], an active diode [87], conical dipoles [11], tapered slot lines [68, 20, 30], microstrip lines [78], microstrip fed quasi-yagi slots [86], coplanar waveguides [63], ring slots [26] and patch antennas [33].

Despite the widely use of rod antennas, the existing theoretical design guidelines are oversimplified [91, 72]. Instead, a number of rigorous numerical methods, such as FDTD [16, 3, 2], integral equation based method [38, 10], and FEM [22], have been applied to investigate the radiation characteristics of dielectric rod antenna. Although these methods are accurate, they are computationally complicated and offer little further thoughts about underlying working mechanism. In order to avoid these computational complexities of numerical methods, analytical methods using local mode theory have been applied to analyze the tapered dielectric wedge [84] and tapered rod antenna [60]. However, the result in [84] is only in two-dimension, and the analysis in [60] is not in detail. In addition, both of the former two papers only investigated the sharp-ended tapered profile which is usually not optimal for a high gain pattern. Based on the local mode analysis in [84, 60], we present in this
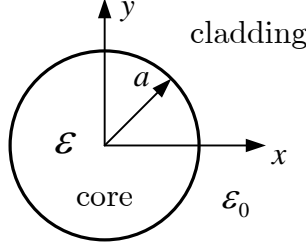
Figure 3.1: Cross-section of a circular waveguide with a radius a

chapter a Local Mode-Volume Current Method (LM-VCM) for tapered circular rod antenna excited by HE_{11} mode. Launching mechanism of this mode [85] is not the focus in this analysis and we assume a purely guided HE_{11} mode is supplied at the input of the rod. We will start from the field expressions of the HE_{11} mode in circular waveguide in the next section.

The surface-wave antenna gain as an increasing function of rod length has been given by Zucker et al. [91]. This increasing tendency is evidenced by our LM-VCM results. For a tapered rod antenna with a fixed length and input geometry, there exists an optimal tapered profile to achieve the maximally attainable gain. Empirical formulas for maximal gain varying with rod lengths are also provided in [91]. Different tapered rod antenna linear and curvilinear taper profiles are simulated by FDTD method in [2]. The authors show that a curvilinearly tapered rod antenna could achieve a higher gain than that with a linear taper. LM-VCM is applied to confirm these results. Dielectric rod antenna can be used not only as a high gain single radiator itself, but also as a feed to the reflector and lens antenna [67, 74]. To locate the feed point in the system, an analysis on the effective phase center of the tapered rod are presented in the last section of this Chapter.

3.2 Analysis of the Circular Waveguide

For a circular waveguide without longitudinal discontinuities, a discrete spectrum of guided modes and a continuous spectrum of radiation modes are supported. The fundamental mode is called HE_{11} mode, also known as the dipole mode. We return to the well-known dispersion relation for the lowest-order hybrid mode in a air-cladding circular waveguide

$$\left[\frac{J_1'(u)}{uJ_1(u)} + \frac{K_1'(v)}{vK_1(v)}\right]\left[\frac{J_1'(u)}{uJ_1(u)} + \frac{K_1'(v)}{\varepsilon_r vK_1(v)}\right] = \left(\frac{1}{u^2} + \frac{1}{v^2}\right)\left(\frac{1}{u^2} + \frac{1}{\varepsilon_r v^2}\right) \quad (3.1)$$

where ε_r is the relative permittivity of waveguide core, $u = k_{\rho 1} a$ and $v = \alpha_{\rho 0} a$. Here, a is the radius of the cylinder and

$$
\begin{aligned}
k_{\rho 1} &= \sqrt{k_0^2 \varepsilon_r - k_z^2} \\
\alpha_{\rho 0} &= \sqrt{k_z^2 - k_0^2}
\end{aligned}
\tag{3.2}
$$

In these definitions, k_z is the waveguide propagation constant in axial direction, k_0 is the free space wave number.

$J_n (\cdot)$ and $K_n (\cdot)$ are the n-th order Bessel function of the first kind and modified Bessel function of the second kind, respectively. $J'_n (\cdot)$, $K'_n (\cdot)$ are the derivatives of Bessel functions with respect to the argument. Their recurrence relationships are (A.2,A.4)

$$
\begin{aligned}
J'_n (z) &= \frac{1}{2} [J_{n-1} (z) - J_{n+1} (z)] \\
K'_n (z) &= \frac{1}{2} [K_{n-1} (z) + K_{n+1} (z)]
\end{aligned}
\tag{3.3}
$$

The HE_{11} mode is degenerate (e.g. HE_{11}^x and HE_{11}^y) due to the circular symmetry. For the mode HE_{11}^y with dominant field components E_y and H_x, the field expressions are [61]

for $\rho \leq a$ (core region)

$$
\begin{aligned}
E_x (\rho, \phi) &= -j \frac{Ak_z}{2k_{\rho 1}} (1 + s) J_2 (k_{\rho 1} \rho) \sin (2\phi) \\
E_y (\rho, \phi) &= j \frac{Ak_z}{2k_{\rho 1}} [(1 - s) J_0 (k_{\rho 1} \rho) + (1 + s) J_2 (k_{\rho 1} \rho) \cos (2\phi)] \\
E_z (\rho, \phi) &= -A J_1 (k_{\rho 1} \rho) \sin (\phi)
\end{aligned}
\tag{3.4}
$$

$$
\begin{aligned}
H_x (\rho, \phi) &= -j \frac{A\omega \varepsilon_0 \varepsilon_r}{2k_{\rho 1}} [(1 - s_1) J_0 (k_{\rho 1} \rho) + (1 + s_1) J_2 (k_{\rho 1} \rho) \cos (2\phi)] \\
H_y (\rho, \phi) &= -j \frac{A\omega \varepsilon_0 \varepsilon_r}{2k_{\rho 1}} (1 + s_1) J_2 (k_{\rho 1} \rho) \sin (2\phi) \\
H_z (\rho, \phi) &= -\frac{Ak_z s}{\omega \mu_0} J_1 (k_{\rho 1} \rho) \cos (\phi)
\end{aligned}
\tag{3.5}
$$

48

for $\rho > a$ (cladding region)

$$
\begin{aligned}
E_x(\rho, \phi) &= j\frac{Ak_z J_1(u)}{2\alpha_{\rho 0} K_1(v)}(1+s)K_2(\alpha_{\rho 0}\rho)\sin(2\phi) \\
E_y(\rho, \phi) &= j\frac{Ak_z J_1(u)}{2\alpha_{\rho 0} K_1(v)}[(1-s)K_0(\alpha_{\rho 0}\rho)-(1+s)K_2(\alpha_{\rho 0}\rho)\cos(2\phi)] \quad (3.6) \\
E_z(\rho, \phi) &= -A\frac{J_1(u)}{K_1(v)}K_1(\alpha_{\rho 0}\rho)\sin(\phi)
\end{aligned}
$$

$$
\begin{aligned}
H_x(\rho, \phi) &= -j\frac{A\omega\varepsilon_0}{2\alpha_{\rho 0}}\frac{J_1(u)}{K_1(v)}[(1-s_0)K_0(\alpha_{\rho 0}\rho)-(1+s_0)K_2(\alpha_{\rho 0}\rho)\cos(2\phi)] \\
H_y(\rho, \phi) &= j\frac{A\omega\varepsilon_0}{2\alpha_{\rho 0}}\frac{J_1(u)}{K_1(v)}(1+s_0)K_2(\alpha_{\rho 0}\rho)\sin(2\phi) \quad (3.7) \\
H_z(\rho, \phi) &= -\frac{Ak_z s}{\omega\mu_0}\frac{J_1(u)}{K_1(v)}K_1(\alpha_{\rho 0}\rho)\cos(\phi)
\end{aligned}
$$

where s, s_{n0} and s_{n1} are defined to simplify the former expression

$$
s = \left(\frac{1}{u^2}+\frac{1}{v^2}\right)\left[\frac{J_1'(u)}{uJ_1(u)}+\frac{K_1'(v)}{vK_1(v)}\right]^{-1} \quad (3.8)
$$

$$
s_{n0} = \frac{k_z^2}{k_0^2}s_n \qquad s_{n1} = \frac{k_z^2}{\varepsilon_r k_0^2}s_n
$$

Electric fields pattern from Equation (3.4) and (3.6) is plotted in Figure 3.2 with $a = 1mm$, $\varepsilon_r = 9.8$ (Alumina) at 33GHz. It is indicated in the figure that the electric fields in the core region are almost linearly polarized in y direction.

3.3 Local HE_{11} Mode along the Tapered Rod

Generally, when the medium is changing its characteristic in the direction of propagation, the pure guided modes in a uniform system no longer exist. However, with the slowly varying transverse properties in the tapered rod, local mode theory is a good approximation for rigorous solution of propagating wave along the taper

49
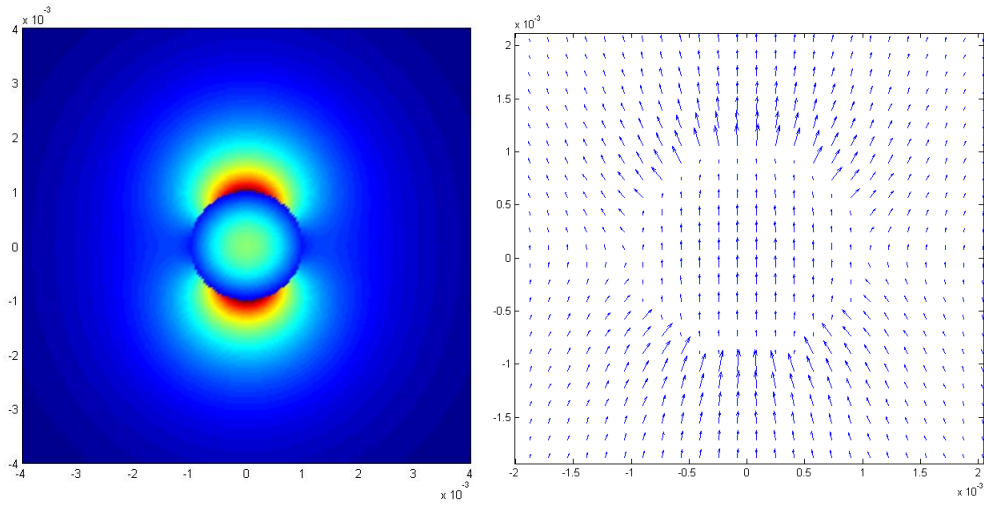
Figure 3.2: Electric field for HE_{11}^y mode in circular dielectric waveguide with $a = 1mm$, $\varepsilon_r = 9.8$ (Alumina) at 33GHz
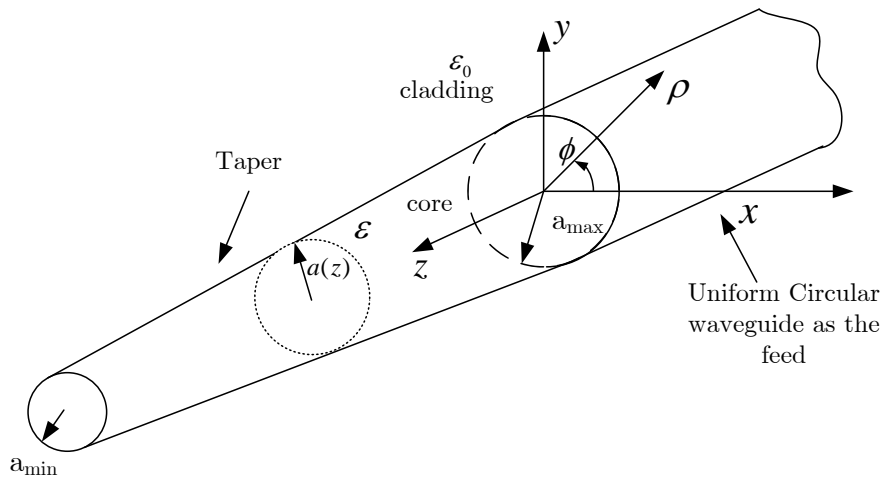
Figure 3.3: Geometry of a tapered rod radiator
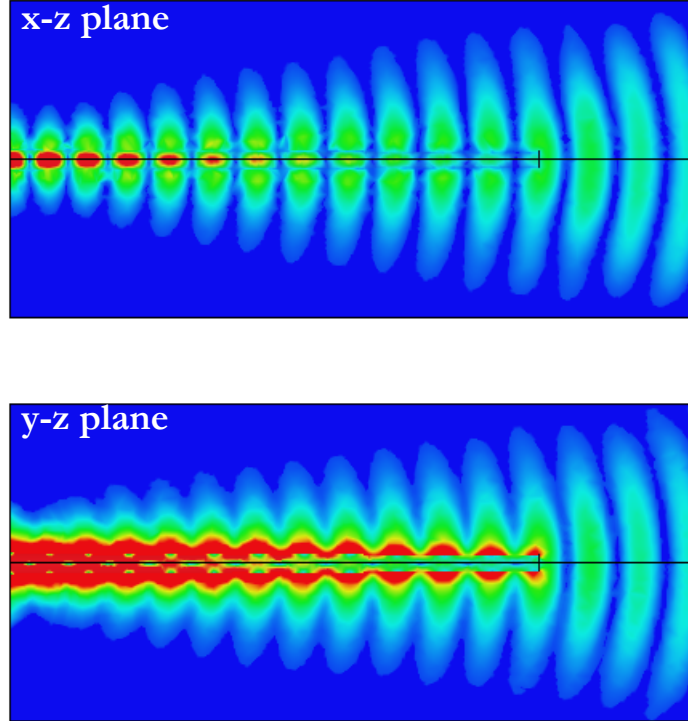
Figure 3.4: Simulated fields of a tapered circular rod exited by HE_{11}^y mode. The rod parameters are: $f = 33GHz$, $\varepsilon_r = 9.8$, $L = 50mm$, $a_{max} = 1mm$ and $a_{min} = 0.75mm$.

[84, 60]. Local mode theory for a taper waveguide simply assumes that: first, the fields over a local transverse plane of the taper will behave as the guided modes in a uniform infinite waveguide which has the same local transverse structures as the taper waveguide; Secondly, the guided mode conversions are adiabatic and no radiation loss along the taper. That is, the fields on any transverse plane $(z = z_0)$ of the tapered waveguide will behave locally with a mode property of the infinite circular waveguide with the same radius $a(z_0)$. 2D field plots in two cutting planes of a rod antenna with $a_{min} = 0.75mm$ are shown in Figure 3.4. In this plot, traveling wave-tails are bent gradually away from the core of the rod, while fields behave as locally guided mode fields near and inside the rod surface.

In this analysis, the radius a_{max} at the input of the tapered rod will be chosen to support only the fundamental HE_{11} mode above cutoff at the operating frequency. Consequently, under the local mode approximation, electric fields in a transverse cut of the tapered waveguide are similar to those in Equation (3.4) but they are updated with the local radius $a(z)$.

$$
\begin{aligned}
E_x\left(\rho, \phi, z\right) &= -j\frac{Ak_z}{2k_{\rho1}}\left(1+s\right)J_2\left(k_{\rho1}\rho\right)\sin\left(2\phi\right) \\[2mm]
E_y\left(\rho, \phi, z\right) &= j\frac{Ak_z}{2k_{\rho1}}\left[\left(1-s\right)J_0\left(k_{\rho1}\rho\right)+\left(1+s\right)J_2\left(k_{\rho1}\rho\right)\cos\left(2\phi\right)\right] \qquad (3.9) \\[2mm]
E_z\left(\rho, \phi, z\right) &= -AJ_1\left(k_{\rho1}\rho\right)\sin\left(\phi\right)
\end{aligned}
$$

Note that A, k_z, $k_{\rho1}$, s, u and v in Equation (3.9) are variables depending on the local radius $a(z)$ of tapered waveguide. z is suppressed in the expression for simplicity. $k_z(z)$ can be solved from the dispersion equation (3.1) with local dimensions.

The other important assumption in the local mode theory mentioned is that the power guided along the tapered waveguide is adiabatic, which means there is no conversion of power into radiation except at the very end of taper. Additionally, we assume the input power launched into the waveguide is 1W and hence the power flowing through any transverse plane of the tapered waveguide is also 1W. Then the coefficient $A(z)$ in the field expression (3.9) can be normalized to have unit power carried by HE_{11} mode. It is shown as

$$
\begin{aligned}
P(z) = P_{inc} = 1\text{W} &= \int_0^{2\pi}\int_0^{\infty} S_z(z)\rho\,d\rho\,d\theta \\[2mm]
&= \frac{1}{2}\int_0^{2\pi}\int_0^{\infty}\left[E_\rho(z)H_\theta^*(z)-E_\theta(z)H_\rho^*(z)\right]\rho\,d\rho\,d\theta \quad (3.10)
\end{aligned}
$$

where

$$
P(z) = |A|^2\left[P_{core}(z)+P_{clad}(z)\right] \tag{3.11}
$$

$$
\begin{aligned}
P_{core} = \frac{\pi}{4}\omega\varepsilon_0\varepsilon_r\frac{k_z}{k_{\rho1}^2}&\left[\left(1-s\right)\left(1-s_1\right)\int_0^a J_0^2\left(k_{\rho1}\right)\rho\,d\rho\right. \\[2mm]
&\left.+\left(1+s\right)\left(1+s_1\right)\int_0^a J_2^2\left(k_{\rho1}\right)\rho\,d\rho\right] \qquad (3.12)
\end{aligned}
$$

$$
\begin{aligned}
P_{clad} = \frac{\pi}{4}\omega\varepsilon_0\frac{k_z}{\alpha_{\rho0}^2}\frac{J_1^2\left(u\right)}{K_1^2\left(v\right)}&\left[\left(1-s\right)\left(1-s_0\right)\int_a^{\infty} K_0^2\left(\alpha_{\rho0}\rho\right)\rho\,d\rho\right. \\[2mm]
&\left.+\left(1+s\right)\left(1+s_0\right)\int_a^{\infty} K_2^2\left(\alpha_{\rho0}\rho\right)\rho\,d\rho\right] \qquad (3.13)
\end{aligned}
$$
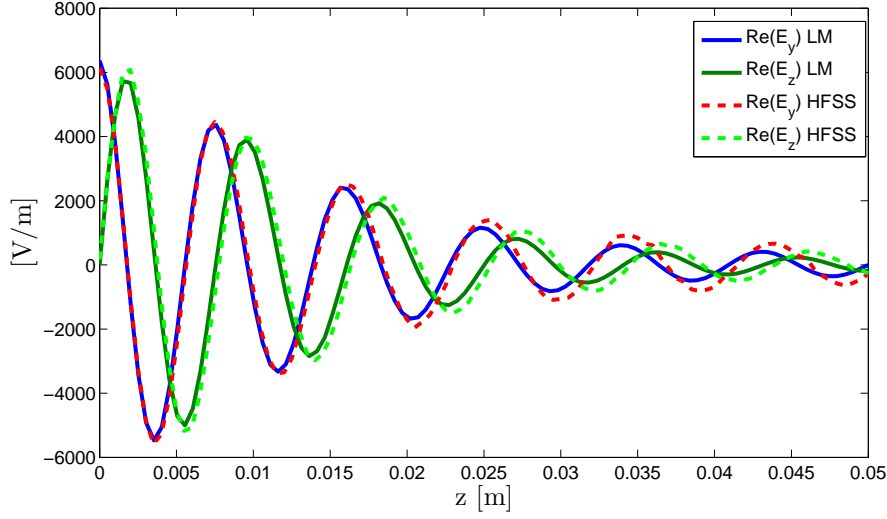
Figure 3.5: $Re(E_y)$ and $Re(E_z)$ for a 50mm long tapered alumina rod with $a_{max} = 1mm$, $a_{min} = 0.5mm$ at 33GHz. These are sampled along a line parametrized as $\left\{ \rho(z) = \frac{a(z)}{2}; \phi(z) = \frac{\pi}{4} \right\}$.

From equation (3.10,3.12,3.13), $A(z)$ can be normalized

$$A(z) = (P_{core}(z) + P_{clad}(z))^{-\frac{1}{2}} \exp \left[-j \int_0^z k_z(z') dz' \right] \qquad (3.14)$$

where $\exp \left[-j \int_0^z k_z(z') dz' \right]$ is the term accounting for the phase delay accumulated along the tapered waveguide.

Closed form expression for integration in Equations (3.12) and (3.13) can be evaluated using integral identities (A.7) and (A.8) in the Appendix. $A(z)$ in Equation (3.32) is then evaluated and substituted back into (3.9) to find the normalized fields. These normalized fields are then sampled along some rods and compared with HFSS [6] simulation results in Figure 3.5, 3.6 and 3.7. Good agreements are observed between the field values obtained from LM and HFSS simulation except small discrepancies near the end of rods. Therefore, the adiabatic local mode (LM) approximation is validated.

Further from the former results, local mode theory tells that $k_z(z)$ of the traveling wave along the taper is solely determined by the local parameter $a(z)$ in Equation (3.1). As will be explain below, this $k_z(z)$ can be an important parameter for designing the tapered rod. Figure 3.8 shows propagation constants of HE_{11} mode solved from Equation (3.1) varying with rod radius from $1mm$ to $0.5mm$. It shows that the value of the propagation constant k_z at $a = 0.75mm$ is actually very close to the k_0, which means the wave with this k_z will has a good match to the fast

53
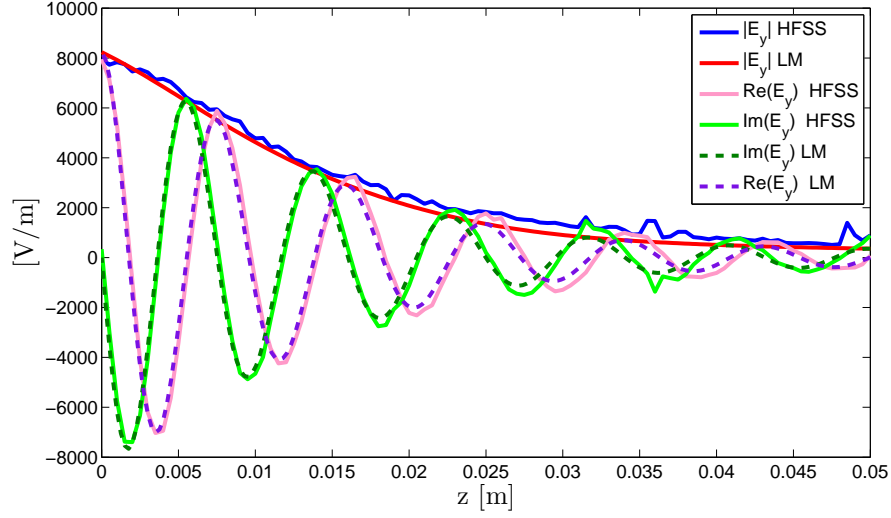
Figure 3.6: Complex E_y for a 50mm long tapered alumina rod with $a_{max} = 1mm$, $a_{min} = 0.5mm$ at 33GHz. These are sampled along a line parametrized as $\left\{ \rho(z) = 0; \phi(z) = \frac{\pi}{4} \right\}$.
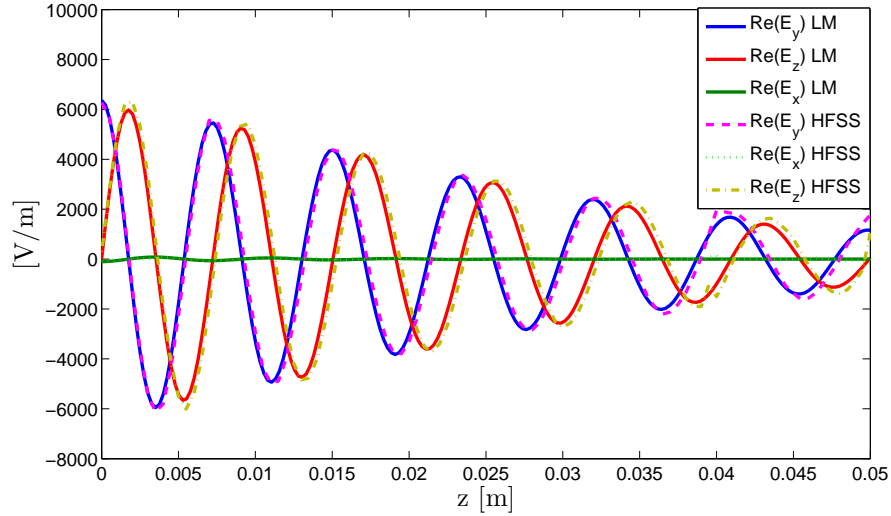
Figure 3.7: Real parts of normalized E_x, E_y and E_z sampled along a line parametrized as $\left\{ \rho(z) = \frac{a(z)}{2}; \phi(z) = \frac{\pi}{4} \right\}$. The simulation is done on a tapered alumina rod with $L = 50mm$, $a_{max} = 1mm$ and $a_{min} = 0.75mm$ at 33GHz.
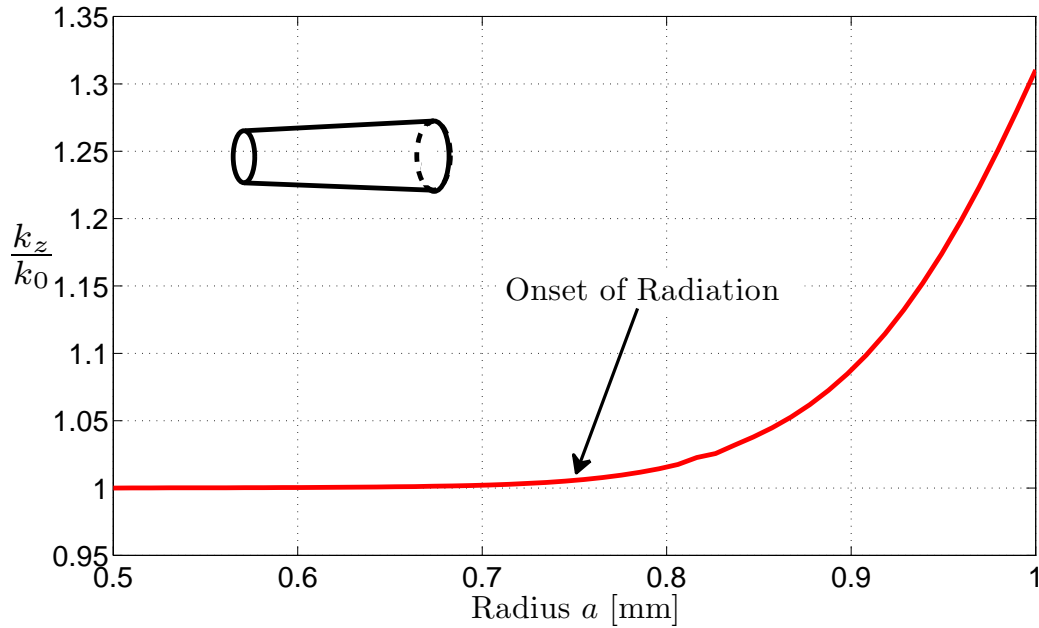
Figure 3.8: Normalized propagation constant of HE_{11} mode varying with a radius a of the rod ($\varepsilon_r = 9.8$).

wave in free space. An important observation drawn from this is that to have an onset of radiation, the radius a_{min} at the tip of taper do not necessarily decrease to zero or even $0.5mm$ in this example. For a rod with $a_{min} = 0.75mm$, the reflection at the tip coupling waves back into the rod can be neglected as it is also evident from Figure 3.4. From a circuit theory point of view, the tapered dielectric rod can essentially be considered as an impedance transformer between the uniform feeding waveguide and the free space. The ending radius $a_{min} = 0.75mm$ is good enough to match the free space impedance. Providing a good match at the end of the rod, intuitively a blunt-end rod antenna will have a higher gain than a sharp-end rod antenna since the former allows the tapered radius decrease more gradually over a limited taper length. This slow variation is believed to help broaden the equi-phase region over terminal aperture at the tip of the rod antenna. The larger the equi-phase region is, the larger the antenna gain is [2]. It is therefore raising a question about what optimal designs of a_{min} and taper profile for a certain L and a_{max} can be chosen to achieve a highest antenna gain. This question will be addressed in later sections.
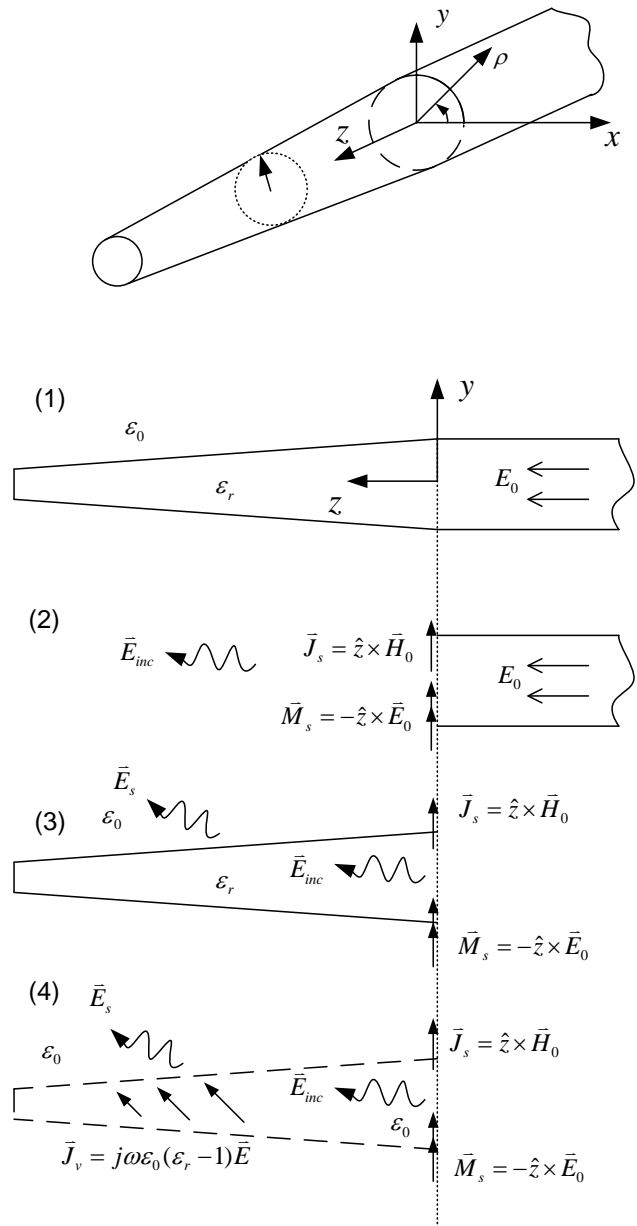
Figure 3.9: Volume current and surface current equivalence for circular rod antenna

3.4 Scattering Approach for the Radiation Pattern of a Tapered Rod

3.4.1 Local Mode-Volume Current Formulation

By considering the wave in the uniform feeding waveguide as the incident wave, the problem can be regarded as a scattering problem [10, 60, 84]. Figure 3.9 demonstrate the equivalent formulation of the problem. Figure 3.9.(2) and 3.9.(3) show the scattering problem equivalent to the original problem in 3.9.(1). Figure 3.9.(2) shows that tapered dielectric rod section is shined on by an incident wave $\overrightarrow{E}_{inc}$ radiated by equivalent surface currents over the feeding aperture at $z = 0$. Meanwhile, this material inhomogeneity formed by the dielectric tapered rod will scatter the incident field and produce the scattering wave denoted as $\overrightarrow{E}_s$. The $\overrightarrow{E}_{inc}$ can also be interpreted as the field radiated from the antenna feeding aperture, while $\overrightarrow{E}_s$ is the terminal field contributed by the tapered antenna section itself. The total radiation field is the superposition of two components. That is

$$\overrightarrow{E} = \overrightarrow{E}_{inc} + \overrightarrow{E}_s \tag{3.15}$$

$\overrightarrow{E}_{inc}$ is produced by equivalent surface magnetic current $\overrightarrow{M}_s$ and electric current $\overrightarrow{J}_s$ as shown in Figure 3.9. Following the volume current equivalence principle [27] which is often seen in the integral equation formulation, $\overrightarrow{E}_s$ is produced by volume polarization current $\overrightarrow{J}_v$. That is

$$\overrightarrow{E}_s = \frac{1}{j\omega\varepsilon_0\mu_0}\overrightarrow{\nabla} \times \overrightarrow{\nabla} \times \overrightarrow{A}_s(\overrightarrow{r}_0) \tag{3.16}$$

where

$$
\begin{aligned}
\overrightarrow{A}_s(\overrightarrow{r}_0) &= \iiint \frac{\mu_0 \overrightarrow{J}_v(\overrightarrow{r}')e^{-jk_0 R}}{4\pi R}dV' \\
&= \int_0^L dz' \int_0^{a(z')} \int_0^{2\pi} \frac{\mu_0 \overrightarrow{J}_v(\rho',\phi',z')e^{-jk_0 R}}{4\pi R}\rho'd\rho'd\phi'
\end{aligned}
\tag{3.17}
$$

$$R = |\overrightarrow{r}_0 - \overrightarrow{r}'| = \sqrt{\rho_0^2 + \rho'^2 - 2\rho_0\rho'\cos(\phi_0 - \phi') + (z' - z_0)^2}$$

$$\overrightarrow{J}_v(\overrightarrow{r}') = j\omega\varepsilon_0\left(\varepsilon_r(\overrightarrow{r}') - 1\right)\overrightarrow{E}(\overrightarrow{r}') \tag{3.18}$$

57

Here $\overrightarrow{r}_0 = [\rho_0, \phi_0, z_0] = [r_0, \phi_0, \theta_0]$ and $\overrightarrow{r'} = [\rho, \phi, z]$ are the observation point and source point, respectively. Rigorously speaking, the field component $\overrightarrow{E}$ in expression of polarization current $\overrightarrow{J}_v = j\omega\varepsilon_0\left(\varepsilon_r - 1\right)\overrightarrow{E}$ is the exact total field inside the core region of the circular rod, and expression (3.16) is generally substituted back into (3.15) to solve for $\overrightarrow{E}$ as an electric field integral equation (EFIE). However, we have demonstrated in the last section that the local mode approximation gives a very good estimation of the total field $\overrightarrow{E}$ in the core region of the taper. Therefore, the rigorous $\overrightarrow{E}$ in (3.18) can be approximated by local mode fields in expression (3.9). As a result, a simple analytical formulation is obtained without resorting to the complex numerical solution of the integral equation (3.15) .

3.4.2 Evaluation of the Scattered Fields Radiated by the Volume Current

Antenna far field analysis is performed in this subsection to obtain the expression for field $\overrightarrow{E}_s$. In the far field, Equation (3.17) can be further simplified by using paraxial approximation

$$
\begin{aligned}
\overrightarrow{A}_s(\overrightarrow{r}_0) &= \iiint \frac{\mu_0 \overrightarrow{J}_v(\overrightarrow{r'})e^{-jk_0 R}}{4\pi R}dV' \\
&= \int_0^L dz' \frac{\mu_0 e^{-jk_0 R'}}{4\pi R'} \int_0^{a(z')} \int_0^{2\pi} \overrightarrow{J}_v(\rho', \phi', z') \\
&\quad \times \exp\left[jk_0\rho'\sin\left(\theta_0'\right)\cos\left(\phi' - \phi_0\right)\right]\rho'd\rho'd\phi' \qquad (3.19)
\end{aligned}
$$

where

$$
R' = \sqrt{\rho_0^2 + \left(z' - z_0\right)^2}
$$

$$
\sin\left(\theta_0'\right) = \frac{r_0}{R}\sin\left(\theta_0\right)
$$

With the far field magnetic potential $\overrightarrow{A}_s$, the scattering electric field expression are derived as

$$
\begin{aligned}
E_{s\theta}(\overrightarrow{r}_0) &= -j\omega A_\theta^s(\overrightarrow{r}_0) \\
&= -j\omega\left[A_x^s(\overrightarrow{r}_0)\cos\left(\theta_0\right)\cos\left(\phi_0\right) + \right. \\
&\quad \left. A_y^s(\overrightarrow{r}_0)\cos\left(\theta_0\right)\sin\left(\phi_0\right) - A_z^s(\overrightarrow{r}_0)\sin\left(\theta_0\right)\right] \qquad (3.20)
\end{aligned}
$$

$$E_{s\phi}(\overrightarrow{r}_0) = -j\omega A_\phi^s(\overrightarrow{r}_0) = -j\omega \left[-A_x^s(\overrightarrow{r}_0)\sin(\phi_0) + A_y^s(\overrightarrow{r}_0)\cos(\phi_0) \right] \quad (3.21)$$

In the following analysis, field expressions (3.9) are plugged into the integral of magnetic potential and the integrations are performed. Each of x, y, and z vector components of $\overrightarrow{A}_s$ is evaluated separately. Although the expressions seem complicated, but all the sub-integrals can be obtained in closed form except the integration along z which will be discretized into a summation. Starting with the dominant component $A_y^s(\overrightarrow{r}_0)$, we have

$$A_y^s(\overrightarrow{r}_0) = -\frac{\omega\varepsilon_0\mu_0}{8\pi}(\varepsilon_r - 1)\int_0^L \frac{e^{-jk_0 R'}k_z(z')A(z')}{R'k_{\rho 1}(z')}I_y(z')dz' \quad (3.22)$$

where $I_y(z')$, which can be evaluated in closed form, is defined as

$$I_y(z') = \int_0^{a(z')}\int_0^{2\pi} \left[(1-s)J_0(k_{\rho 1}\rho') + (1+s)J_2(k_{\rho 1}\rho')\cos(2\phi') \right]$$
$$\exp\left[jk_0\sin\theta_0'\rho'\cos(\phi'-\phi_0) \right]\rho'd\rho'd\phi' \quad (3.23)$$

. Using the integral representation of Bessel function (A.5) and (A.6), we have

$$\int_0^{2\pi} \exp\left[jk_0\sin\theta_0'\rho'\cos(\phi'-\phi_0) \right]d\phi' = 2\pi J_0(k_0\sin\theta_0'\rho') \quad (3.24)$$

$$\int_0^{2\pi} \cos(2\phi')\exp\left[jk_0\sin\theta_0'\rho'\cos(\phi'-\phi_0) \right]d\phi'$$
$$= -2\pi\cos(2\phi_0)J_2(k_0\sin\theta_0'\rho')$$

Thus

$$I_y(z') = 2\pi\int_0^{a(z')} \left[(1-s)J_0(k_{\rho 1}\rho')J_0(k_0\sin\theta_0'\rho') \right.$$
$$\left. -(1+s)J_2(k_{\rho 1}\rho')J_2(k_0\sin\theta_0'\rho')\cos(2\phi_0) \right]\rho'd\rho' \quad (3.25)$$

The two integration involving Bessel functions in the former expression can also be obtained in closed form using the identity in (A.9). Defining

$$
\begin{aligned}
I_{Jn}(z') &= \frac{a\,(z')}{k_0^2 \sin^2 \theta_0' - k_{\rho1}^2} \left[k_0 \sin \theta_0' J_n(k_{\rho1} a\,(z')) J_{n+1}(k_0 \sin \theta_0' a\,(z')) \right. \\
&\quad \left. -k_{\rho1} J_{n+1}(k_{\rho1} a\,(z')) J_n(k_0 \sin \theta_0' a\,(z')) \right]
\end{aligned}
\tag{3.26}
$$

Substituting (3.26), (3.25) back into (3.22), we have

$$
\begin{aligned}
A_y^s(\overrightarrow{r}_0) &= -\frac{\omega \varepsilon_0 \mu_0}{4} (\varepsilon_r - 1) \int_0^L \frac{e^{-jk_0 R'} k_z(z') A(z')}{R' k_{\rho1}(z')} \\
&\quad \left[(1-s) I_{J0}(z') - (1+s) \cos (2\phi_0) I_{J2}(z') \right] dz'
\end{aligned}
\tag{3.27}
$$

Following a similar approach, $A_x^s(\overrightarrow{r}_0)$ and $A_z^s(\overrightarrow{r}_0)$ can be evaluated as follows

$$
A_x^s(\overrightarrow{r}_0) = \frac{\omega \varepsilon_0 \mu_0}{8\pi} (\varepsilon_r - 1) \int_0^L \frac{e^{-jk_0 R'} k_z(z') A(z')}{R' k_{\rho1}(z')} I_x(z') dz'
\tag{3.28}
$$

where $I_x(z')$ is defined as

$$
\begin{aligned}
I_x(z') &= \int_0^{a(z')} \int_0^{2\pi} (1+s) J_2 (k_{\rho1} \rho') \sin (2\phi') \\
&\quad \exp \left[jk_0 \sin \theta_0' \rho' \cos (\phi' - \phi_0) \right] \rho' d\rho' d\phi'
\end{aligned}
\tag{3.29}
$$

The integration inside $I_x(z')$ can be evaluated using (A.6)

$$
\begin{aligned}
&\int_0^{2\pi} \sin (2\phi') \exp \left[jk_0 \sin \theta_0' \rho' \cos (\phi' - \phi_0) \right] d\phi' \\
&= -2\pi \sin (2\phi_0) J_2 (k_0 \sin \theta_0' \rho')
\end{aligned}
\tag{3.30}
$$

Substituting (3.30) and (3.26) into (3.28), we get

$$
A_x^s(\overrightarrow{r}_0) = -\frac{\omega \varepsilon_0 \mu_0}{4} (\varepsilon_r - 1) \sin (2\phi_0) \int_0^L \frac{e^{-jk_0 R'} k_z(z') A(z')}{R' k_{\rho1}(z')} I_{J2}(z') dz'
\tag{3.31}
$$

Similarly, we obtain $A_z^s(\overrightarrow{r}_0)$ as

$$A_z^s(\overrightarrow{r}_0) \;=\; -j\frac{\omega\varepsilon_0\mu_0}{4\pi}(\varepsilon_r-1)\int_0^L \frac{e^{-jk_0R'}A(z')}{R'}I_z(z')dz' \tag{3.32}$$

where $I_z(z')$ is defined as

$$I_z(z') \;=\; \int_0^{a(z')}\int_0^{2\pi} J_1\left(k_{\rho 1}\rho'\right)\sin\left(\phi'\right)$$
$$\exp\left[jk_0\sin\theta_0'\rho'\cos\left(\phi'-\phi_0\right)\right]\rho'd\rho'd\phi' \tag{3.33}$$

Again, the integration inside $I_z(z')$ can be evaluated as

$$\int_0^{2\pi}\sin\left(\phi'\right)\exp\left[jk_0\sin\theta_0'\rho'\cos\left(\phi'-\phi_0\right)\right]d\phi'$$
$$=\;2\pi j\sin\left(\phi_0\right)J_1\left(k_0\sin\theta_0'\rho'\right) \tag{3.34}$$

Substituting (3.34) and (3.26) into (3.32), we have

$$A_z^s(\overrightarrow{r}_0) \;=\; \frac{\omega\varepsilon_0\mu_0}{2}(\varepsilon_r-1)\sin\left(\phi_0\right)\int_0^L \frac{e^{-jk_0R'}A(z')}{R'}I_{J1}(z')dz' \tag{3.35}$$

Because the integration along z in $A_x^s(\overrightarrow{r}_0)$, $A_y^s(\overrightarrow{r}_0)$ and $A_z^s(\overrightarrow{r}_0)$ cannot be obtained in closed form, the tapered rod with a length L is chopped into N small segments and each segment can be approximated by a uniform waveguide with a length $\triangle z = L/N$ and radius a_n where $n = 1, 2, \cdots, N$. In this fashion, the integration along z becomes a summation of N terms. Each term involves solving HE_{11} mode dispersion equation (3.1) and evaluation of sub-integral along ρ and ϕ. Finally, scattered electric far field can be obtained from (3.20) and (3.21).

3.4.3 Evaluation of the Incident Fields Radiated by the Surface Currents

In this subsection, far field expressions for $\overrightarrow{E}_{inc}$ are derived. The equivalent surface current $\overrightarrow{J}_s$ and $\overrightarrow{M}_s$ on the transverse surface at $z = 0$, which generate $\overrightarrow{E}_{inc}$, are expressed as

$$\overrightarrow{M}_s = -\hat{z} \times \overrightarrow{E}_0 \tag{3.36}$$

$$\overrightarrow{J}_s = \hat{z} \times \overrightarrow{H}_0 \tag{3.37}$$

Again, the total fields $\overrightarrow{E}_0$ and $\overrightarrow{H}_0$ are approximated by the local mode fields in (3.4) and (3.6) which are calculated from a uniform circular waveguide with a radius a_0. It should be noted that reflected fields at $z = 0$ are assumed to be negligible due to the slow taper and hence only forward propagating field expressions are plugged into (3.36) and (3.37). $\overrightarrow{E}_{inc}$ produced by $\overrightarrow{J}_s$ and $\overrightarrow{M}_s$ in the far field region is:

$$E_{inc\theta} = -j\omega A_\theta - j\omega\eta_0 F_\phi \qquad E_{inc\phi} = -j\omega A_\phi + j\omega\eta_0 F_\theta \tag{3.38}$$

$$\overrightarrow{F}\left(\overrightarrow{r}_0\right) = \frac{\varepsilon_0 e^{-jk_0 r_0}}{4\pi r_0} \int_0^\infty \int_0^{2\pi} \overrightarrow{M}_s\left(\rho', \phi'\right) \exp\left[jk_0\rho' \sin\left(\theta_0\right) \cos\left(\phi' - \phi_0\right)\right] \rho' d\rho' d\phi' \tag{3.39}$$

$$\overrightarrow{A}\left(\overrightarrow{r}_0\right) = \frac{\mu_0 e^{-jk_0 r_0}}{4\pi r_0} \int_0^\infty \int_0^{2\pi} \overrightarrow{J}_s\left(\rho', \phi'\right) \exp\left[jk_0\rho' \sin\left(\theta_0\right) \cos\left(\phi' - \phi_0\right)\right] \rho' d\rho' d\phi' \tag{3.40}$$

Putting (3.36) into (3.39), we have

$$F_x\left(\overrightarrow{r}_0\right) = \frac{\varepsilon_0 e^{-jk_0 r_0}}{4\pi r_0} \int_0^\infty \int_0^{2\pi} E_y\left(\rho', \phi'\right) \exp\left[jk_0\rho' \sin\left(\theta_0\right) \cos\left(\phi' - \phi_0\right)\right] \rho' d\rho' d\phi' \tag{3.41}$$

$$F_y\left(\overrightarrow{r}_0\right) = -\frac{\varepsilon_0 e^{-jk_0 r_0}}{4\pi r_0} \int_0^\infty \int_0^{2\pi} E_x\left(\rho', \phi'\right) \exp\left[jk_0\rho' \sin\left(\theta_0\right) \cos\left(\phi' - \phi_0\right)\right] \rho' d\rho' d\phi' \tag{3.42}$$

$$A_x\left(\overrightarrow{r}_0\right) = -\frac{\mu_0 e^{-jk_0 r_0}}{4\pi r_0} \int_0^\infty \int_0^{2\pi} H_y\left(\rho', \phi'\right) \exp\left[jk_0\rho' \sin\left(\theta_0\right) \cos\left(\phi' - \phi_0\right)\right] \rho' d\rho' d\phi' \tag{3.43}$$

$$A_y\left(\overrightarrow{r}_0\right) = \frac{\mu_0 e^{-jk_0 r_0}}{4\pi r_0} \int_0^\infty \int_0^{2\pi} H_x\left(\rho', \phi'\right) \exp\left[jk_0\rho' \sin\left(\theta_0\right) \cos\left(\phi' - \phi_0\right)\right] \rho' d\rho' d\phi' \tag{3.44}$$

$\overrightarrow{F}\left(\overrightarrow{r}_0\right)$ is broken down into the core and cladding parts to be evaluated separately. Evaluations of the above integrals in the core region has already been presented in the previous section. The integration in the cladding region is similar:

$$F_{xcore}\left(\overrightarrow{r}_0\right) = j\frac{\varepsilon_0 Ak_z e^{-jk_0 r_0}}{4k_{\rho 1}r_0}\left[(1-s)I_{J0} - (1+s)\cos(2\phi_0)I_{J2}\right]$$

$$F_{ycore}\left(\overrightarrow{r}_0\right) = -j\frac{\varepsilon_0 Ak_z e^{-jk_0 r_0}}{4k_{\rho 1}r_0}(1+s)\sin(2\phi_0)I_{J2}$$

$$F_{xclad}\left(\overrightarrow{r}_0\right) = j\frac{\varepsilon_0 Ak_z e^{-jk_0 r_0}J_1\left(u\right)}{4\alpha_{\rho 0}r_0 K_1\left(v\right)}\left[(1-s)I_{K0} + (1+s)\cos(2\phi_0)I_{K2}\right]$$

$$F_{yclad}\left(\overrightarrow{r}_0\right) = j\frac{\varepsilon_0 Ak_z e^{-jk_0 r_0}J_1\left(u\right)}{4\alpha_{\rho 0}r_0 K_1\left(v\right)}(1+s)\sin(2\phi_0)I_{K2}$$

$$A_{xcore}\left(\overrightarrow{r}_0\right) = -j\frac{A\omega\varepsilon_0\mu_0\varepsilon_r e^{-jk_0 r_0}}{4k_{\rho 1}r_0}(1+s_1)\sin(2\phi_0)I_{J2}$$

$$A_{ycore}\left(\overrightarrow{r}_0\right) = -j\frac{A\omega\varepsilon_0\mu_0\varepsilon_r e^{-jk_0 r_0}}{4k_{\rho 1}r_0}\left[(1-s_1)I_{J0} - (1+s_1)\cos(2\phi_0)I_{J2}\right]$$

$$A_{xclad}\left(\overrightarrow{r}_0\right) = j\frac{A\omega\varepsilon_0\mu_0 e^{-jk_0 r_0}J_1\left(u\right)}{4\alpha_{\rho 0}r_0 K_1\left(v\right)}(1+s_0)\sin(2\phi_0)I_{K2}$$

$$A_{yclad}\left(\overrightarrow{r}_0\right) = -j\frac{A\omega\varepsilon_0\mu_0 e^{-jk_0 r_0}J_1\left(u\right)}{4\alpha_{\rho 0}r_0 K_1\left(v\right)}\left[(1-s_0)I_{K0} + (1+s_0)\cos(2\phi_0)I_{K2}\right]$$

Using the identity in (A.10), we define

$$\begin{aligned}
I_{Kn} &= \int_{a_0}^{\infty} K_n(\alpha_{\rho 0}\rho')J_n(k_0\sin\theta_0\rho')\rho'd\rho'\\
&= -\frac{a_0}{k_0^2\sin^2\theta_0 - \alpha_{\rho 0}^2}\left[k_0\sin\theta_0 K_n(\alpha_{\rho 0}a_0)J_{n+1}(k_0\sin\theta_0 a_0)\right.\\
&\quad \left. - k_{\rho 1}K_{n+1}(\alpha_{\rho 0}a_0)J_n(k_0\sin\theta_0 a_0)\right] \tag{3.45}
\end{aligned}$$

Therefore, we have

$$F_x\left(\overrightarrow{r}_0\right) = j\frac{\varepsilon_0 A k_z e^{-jk_0 r_0}}{4r_0}\left[(1-s)\left(\frac{I_{J0}}{k_{\rho1}} + \frac{J_1\left(u\right)I_{K0}}{K_1\left(v\right)\alpha_{\rho0}}\right)\right.$$
$$\left. - (1+s)\cos\left(2\phi_0\right)\left(\frac{I_{J2}}{k_{\rho1}} - \frac{J_1\left(u\right)I_{K2}}{K_1\left(v\right)\alpha_{\rho0}}\right)\right]$$

$$F_y\left(\overrightarrow{r}_0\right) = -j\frac{\varepsilon_0 A k_z e^{-jk_0 r_0}}{4r_0}(1+s)\sin\left(2\phi_0\right)\left(\frac{I_{J2}}{k_{\rho1}} - \frac{J_1\left(u\right)I_{K2}}{K_1\left(v\right)\alpha_{\rho0}}\right)$$

$$A_x\left(\overrightarrow{r}_0\right) = A_{xcore} + A_{xclad} \quad A_y\left(\overrightarrow{r}_0\right) = A_{ycore} + A_{yclad}$$

3.4.4   The Total Radiation Fields and Their Properties

As shown in (3.15), the total radiation field is the superposition of incident field from the feeding aperture and scattered field from the tapered rod

$$E_\theta = -j\omega\left(A_\theta^s(\overrightarrow{r}_0) + A_\theta\right) - j\omega\eta_0 F_\phi \qquad (3.46)$$

$$E_\phi = -j\omega\left(A_\phi^s(\overrightarrow{r}_0) + A_\phi\right) + j\omega\eta_0 F_\theta \qquad (3.47)$$

3.4.4.1   Directivity Analysis

The radiation intensity $U\left(\theta_0, \phi_0\right)$ and directivity pattern $F\left(\theta_0, \phi_0\right)$ are

$$U\left(\theta_0, \phi_0\right) = \frac{r_0^2}{2\eta_0}\left(|E_\theta|^2 + |E_\phi|^2\right) \qquad (3.48)$$

$$F\left(\theta_0, \phi_0\right) = \frac{U\left(\theta_0, \phi_0\right)}{\left[U\left(\theta_0, \phi_0\right)\right]_{max}} \qquad (3.49)$$

It is shown in Figure 3.10, 3.11 and 3.12, our local mode-volume current method (LM-VCM) gives a good estimation of the radiation pattern especially for small θ_0, as compared to the simulation results from HFSS. The half power beamwidths are predicted quite accurately. The directivity of the tapered rod antenna can be estimate using a simple formula [8]
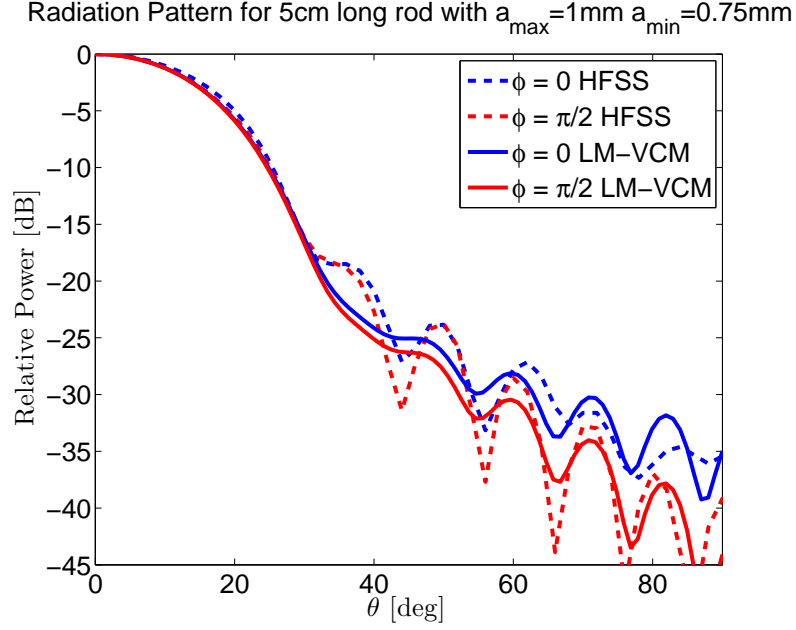
Figure 3.10: Radiation pattern for a 50mm long tapered alumina rod with $a_{max} = 1mm$, $a_{min} = 0.75mm$ at 33GHz. The half power bandwidths from LM-VCM are $\Theta_1 = \Theta_2 = 29.4°$ and $D \simeq 16.79$dB. The simulated directivity from HFSS is 16.22dB.

$$D \simeq \frac{4\pi}{\Theta_1 \Theta_2} \qquad (3.50)$$

Θ_1 and Θ_2 are half power beamwidths in the cutting plane with $\phi_0 = 0$ and $\phi_0 = \frac{\pi}{2}$, respectively. The graph reveals that $\Theta_1 \simeq \Theta_2$ for all the cases since E field and H field intensity profiles are almost the same in the core region for HE_{11} mode [91].

It can be observed from Figure 3.13 and 3.14 that the rod with $a_{min} = 0.75mm$ has a higher gain since it has a smaller beamwidth and a lower side-lobe level . It should be noted that although the local mode approximation might not be valid when $a_{min} \rightarrow a_{max}$ since the reflection at the dielectric-air interface can no longer be negligible, still the tendency in Figure 3.13 helps designers to identify a higher gain configuration.

It is well-known that a longer taper enabling a more gradually-varying profile leads to a higher antenna gain and smaller main-lobe beamwidth [91]. Figure 3.15 and 3.16 demonstrate the gain enhancement of a tapered rod antenna varies with an increasing antenna length. It reveals that the directivity increases and the half power bandwidth shrinks as taper length increases. The half power bandwidths are compared with Zucker's approximate beamwidth formula [91] for the optimal gain
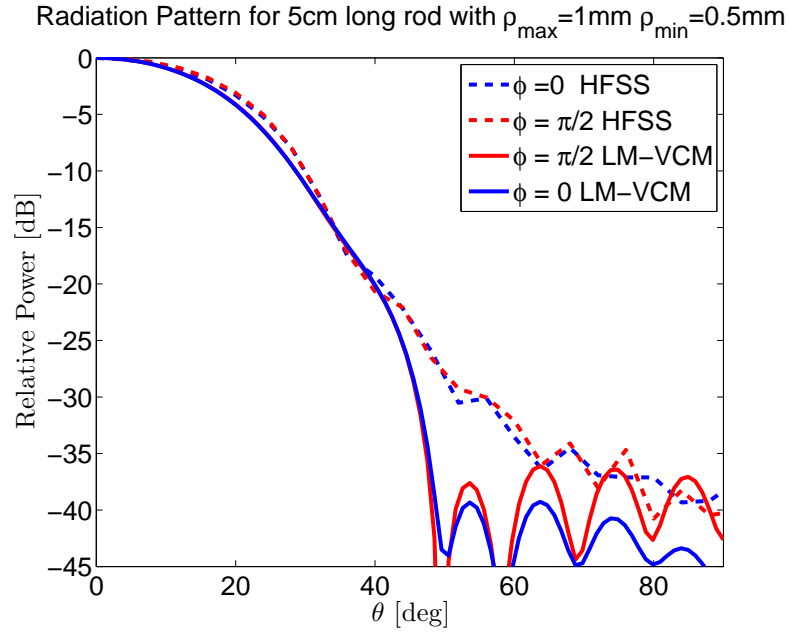
Figure 3.11: Radiation pattern for a 50mm long tapered alumina rod with $a_{max} = 1mm$, $a_{min} = 0.5mm$ at 33GHz. The half power bandwidths from LM-VCM are $\Theta_1 = \Theta_2 = 36.6°$ and $D \simeq 14.87$dB. The simulated directivity from HFSS is 15.17dB.
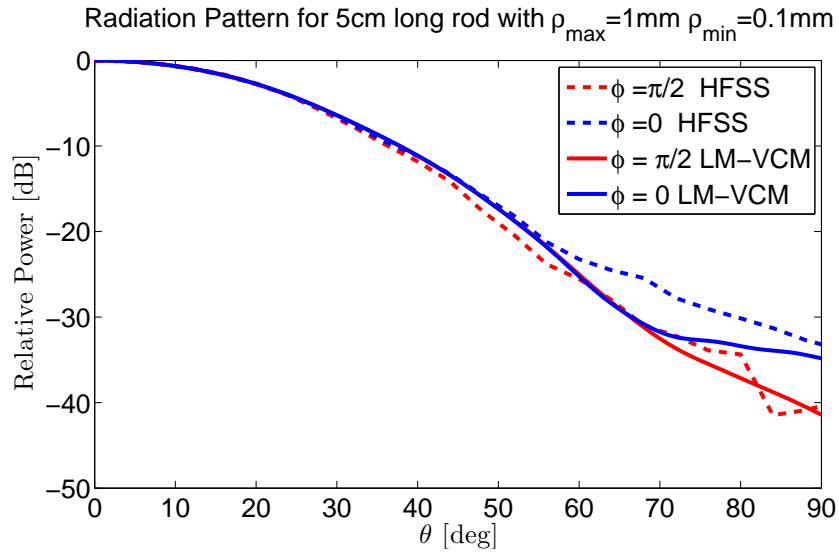
Figure 3.12: Radiation pattern for a 50mm long tapered alumina rod with $a_{max} = 1mm$, $a_{min} = 0.1mm$ at 33GHz. The half power bandwidths from LM-VCM are $\Theta_1 = \Theta_2 = 41.6°$ and $D \simeq 13.77$dB. The simulated directivity from HFSS is 13.49dB.
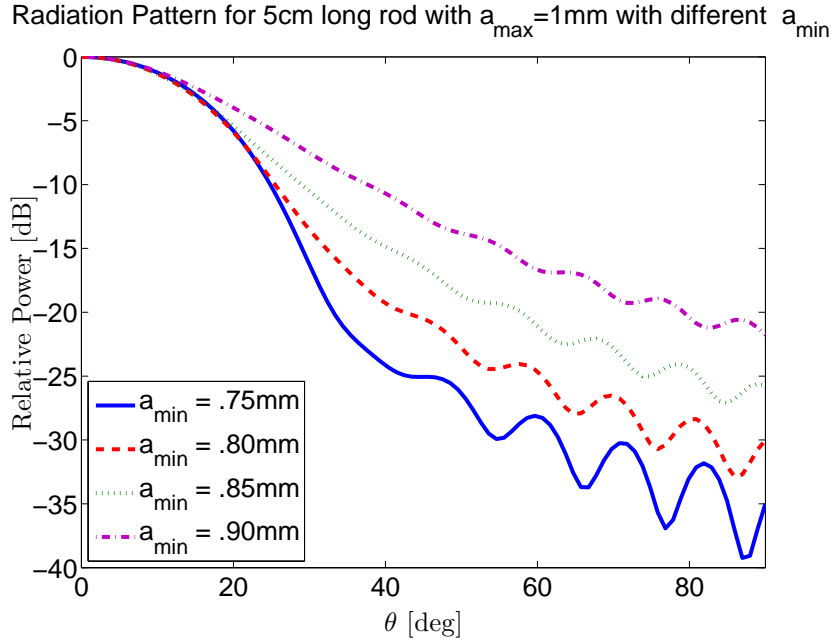
Figure 3.13: Radiation pattern with $\phi = 0°$ for a 50mm long tapered alumina rod with $a_{max} = 1mm$ and different a_{min} at 33GHz.
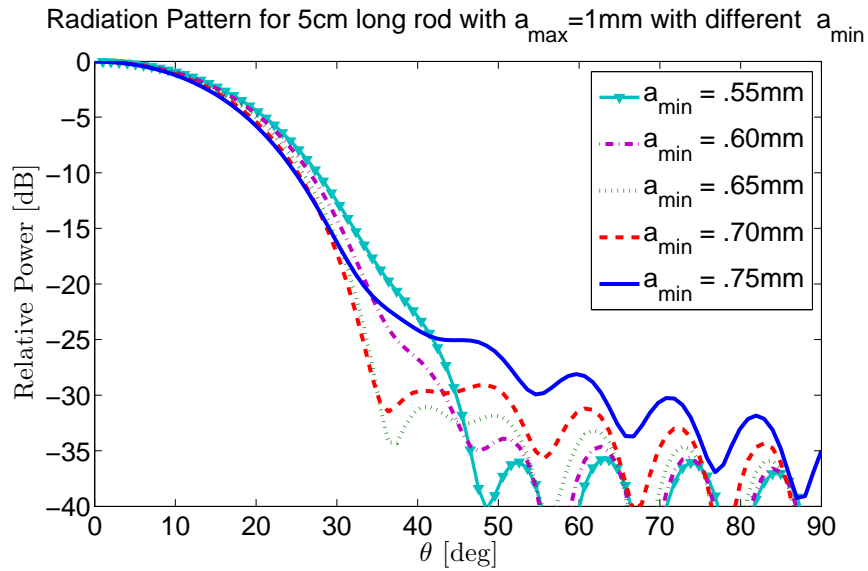
Figure 3.14: Radiation pattern with $\phi = 0°$ for a 50mm long tapered alumina rod with $a_{max} = 1mm$ and different a_{min} at 33GHz.

Figure 3.15: Radiation pattern with $\phi = 0°$ for tapered alumina rods with $a_{max} = 1mm$ and $a_{min} = 0.75mm$ at 33GHz with different length to free space wavelength ratio .
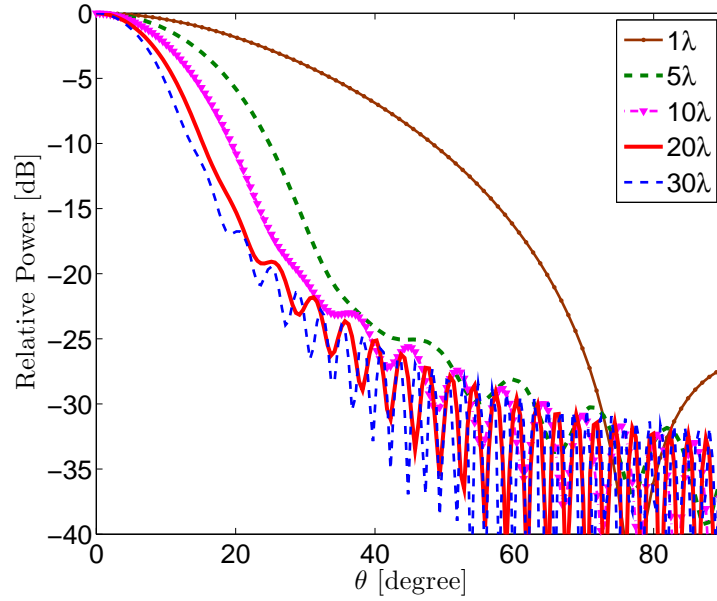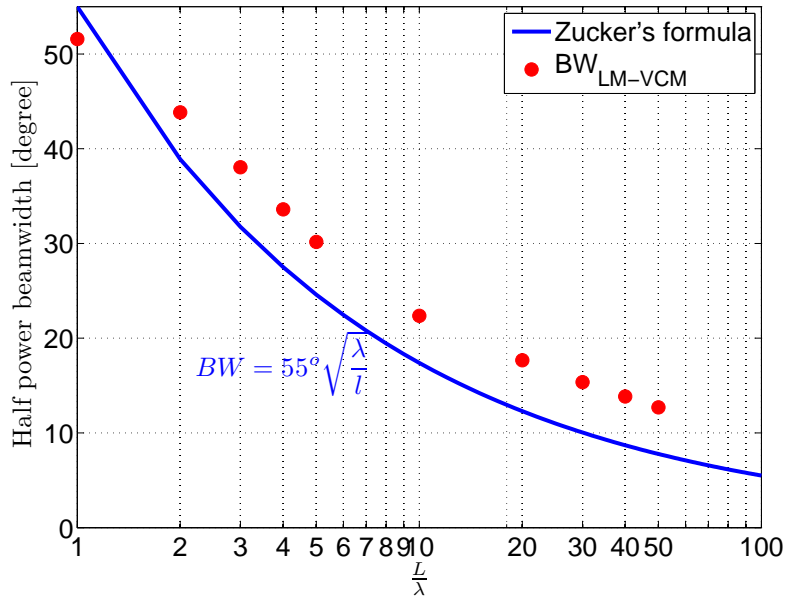

Figure 3.16: Half power beamwidths of tapered alumina rods with $a_{max} = 1mm$ and $a_{min} = 0.75mm$ at 33GHz with different length to wavelength ratio .

design of surface wave antennas (Figure 3.16)

$$BW = 55\sqrt{\lambda/l} \;\; \text{[degree]} \tag{3.51}$$

where l is the antenna taper length, λ is the wavelength of operation.

Although a linearly tapered rod with $a_{max} = 1mm$ and $a_{min} = 0.75mm$ is not an optimal design for all antenna lengths, it shows the tendency of decreasing band-widths with an increasing tapered length in Figure 3.16. Other than linear taper, curvilinear taper profile should be considered to achieve the near optimal directivity for a specific length. The superposition and interaction of the two complex fields emanated from the feed aperture (surface current source) and the dielectric rod itself (volume current source) should be further investigate to fully understand the radiation characteristic.

3.4.4.2 Comparison of Linearly and Curvilinearly Tapered Rod Profile

Figure 3.16 in the previous sub-section shows the beamwidths achieved by linearly tapered rods are not optimal yet. It is of practical importance to provide guidelines and methods to design a maximal gain tapered rod antenna. With the availability of the present analytical method, we are able to select and optimize the taper profile to meet such a requirement. In order to discriminate the effectiveness of taper profile, we fix the value of a_{min} and a_{max}, and interpolate the local radius in between the feed and the tip. Following the interpolation formula suggested by Ando et al. [2], the equation governing the taper profile is chosen be to

$$a(z) = a_{max} - (a_{max} - a_{min}) \left(\frac{z}{L}\right)^{\frac{1}{n}} \tag{3.52}$$

The parameter n is used to control the curvature of the taper. Obviously, curve with $n = 1$ is linear, while curves with $n > 1$ are concavely-curvilinear and curves with $0 < n < 1$ are convexly-curvilinear (Figure 3.17). For a larger n value, the local radius approaches to a_{min} faster along z. It is expected the convexly-curvilinear tapered rod will have a less gain than the rod with a linear profile. As we can see from Figure 3.17(c) that this taper type effectively extends uniform section and shortens the taper length L. The reduction in effective taper length will decrease the gain. Whitman et al. [84] also confirmed convexly-curvilinear tapered wedge antennas has small gains compared to that with a linear taper.

We adopt same test cases presented by Ando et al. [2] by having a 20λ long Teflon ($\varepsilon_r = 2$) tapered rod with $a_{max} = 0.32\lambda$ and $a_{min} = 0.16\lambda$ test with linear ($n = 1$) and curvilinear ($n = 3, 1/3$) profiles. The resulting patterns are shown in Figure 3.18. When the profile changes from a linear taper to a curvilinear taper ($n = 3$), the
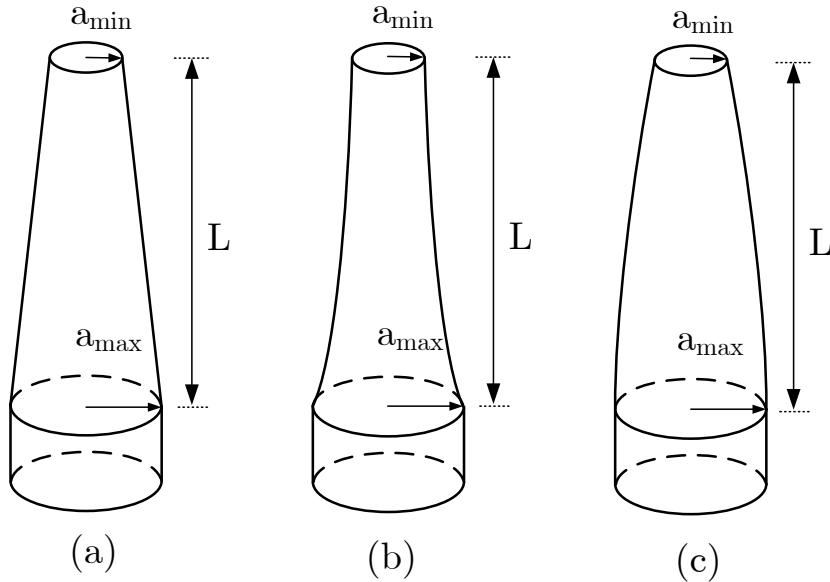
Figure 3.17: Different taper profiles of circular rod antenna: (a) Linear taper; (b) Concavely-curvilinear taper; (c) Convexly-curvilinear taper.

half-power beamwidth drops from 18.22° to 14.52°, which is almost the same as the result presented in the original paper. The figure also confirms the ineffectiveness of convex-curvilinear profile. From now on, the term curvilinear taper refers to the concave-curvilinear case for simplicity. Figure 3.19 plots the half power beamwidth of a curvilinearly tapered rod antenna compared with the linearly tapered rod case and the optimal gain beamwidth given by Zucker (3.51). Similar tendencies and the beamwidth improvements are observed for curvilinear taper case.

3.4.4.3   Phase Center Analysis

Dielectric rod antennas possesses the characteristic of high efficiencies and low side-lobe levels . They can be further integrated into the lens-antenna shown in Figure 3.20 to increase the antenna directivity [74]. In these applications, the feed antenna is usually considered as a source radiating spherical waves from its effective phase center. This effective phase center is aligned at the focal point of the reflector or the lens [74, 66, 67]. Thus, we need to estimate the effective phase center of the out-going wave from the dielectric rod antenna if it is used as a feed.

It is shown in Figure 3.21 and 3.22 that the calculated field magnitudes and phases from LM-VCM agree well with simulated results from HFSS over the aperture 10mm away from the tip of the 50mm tapered rod antenna. Therefore, assuming spherical wavefront over the aperture as shown by Equation (3.53) , the phase center of the out going wave can be obtained by curve-fitting the analytical result in Figure 3.21.
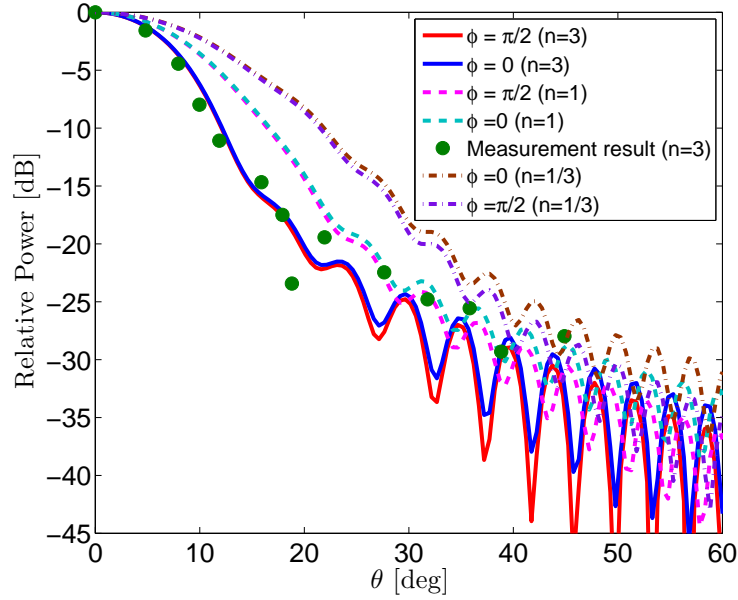
Figure 3.18: Radiation pattern of a 20λ long Teflon ($\varepsilon_r = 2$) tapered rod with $a_{max} = 0.32\lambda$ and $a_{min} = 0.16\lambda$ with different tapered profile: $n = 1$ and $n = 3$.
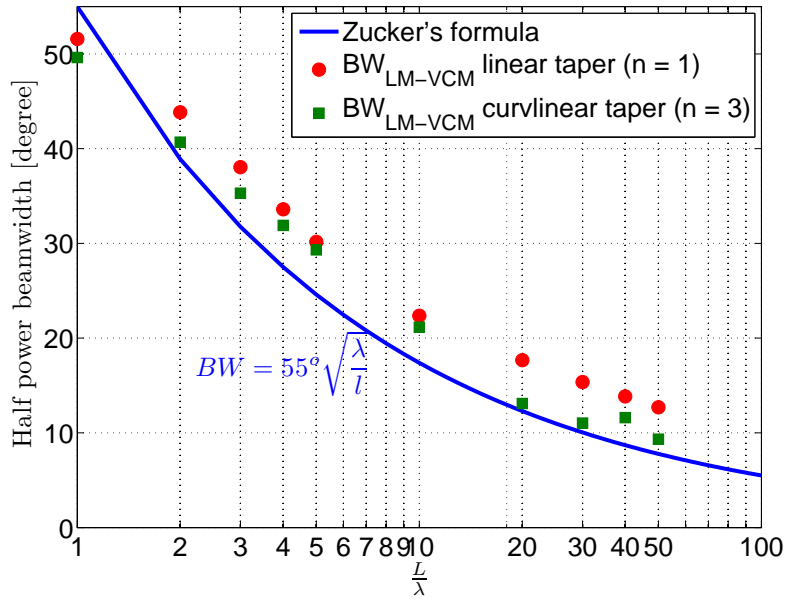
Figure 3.19: Half power beamwidth of tapered alumina rods with $a_{max} = 1mm$ and $a_{min} = 0.75mm$ at 33GHz with different length to wavelength ratio .

$$\phi(x) = \phi_0 - k_0 \left(\sqrt{x^2 + (z - z_0)^2} - z + z_0 \right) \qquad (3.53)$$

where k_0 is the free space wave number, z_0 is the location of the phase center and ϕ_0 is the phase at $x = 0$. For Figure 3.21, the phase center are shown to be $z_0 = 32mm$ (Figure 3.23).
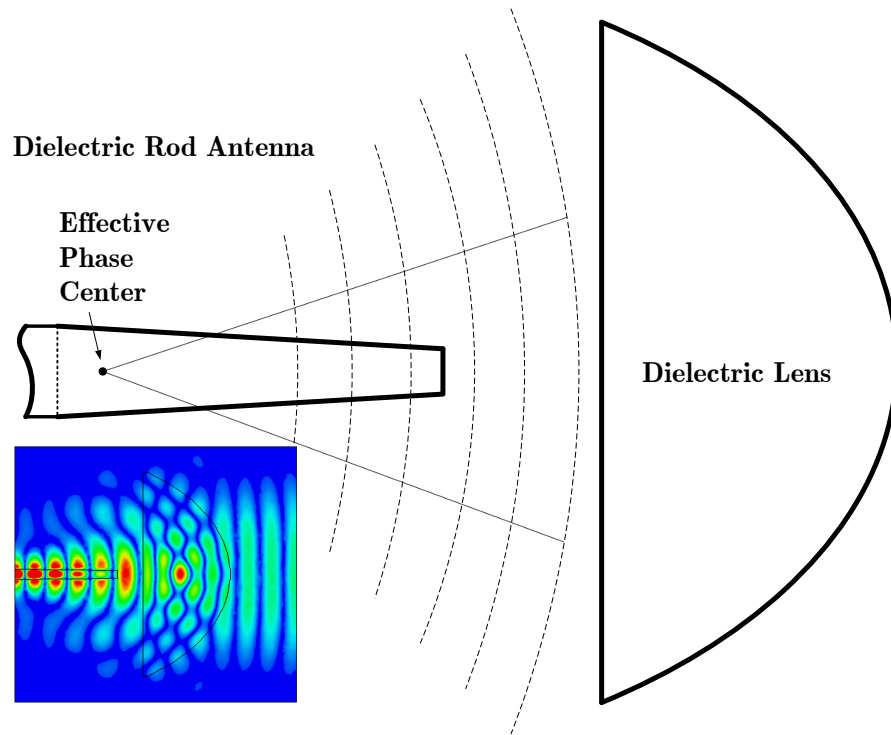
Figure 3.20: Effective phase center of dielectric rod-lens antenna configuration
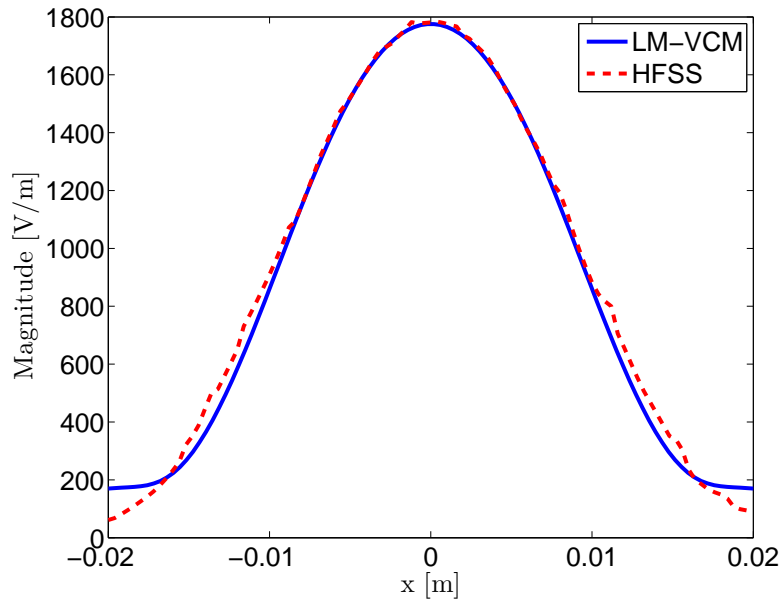
(a)
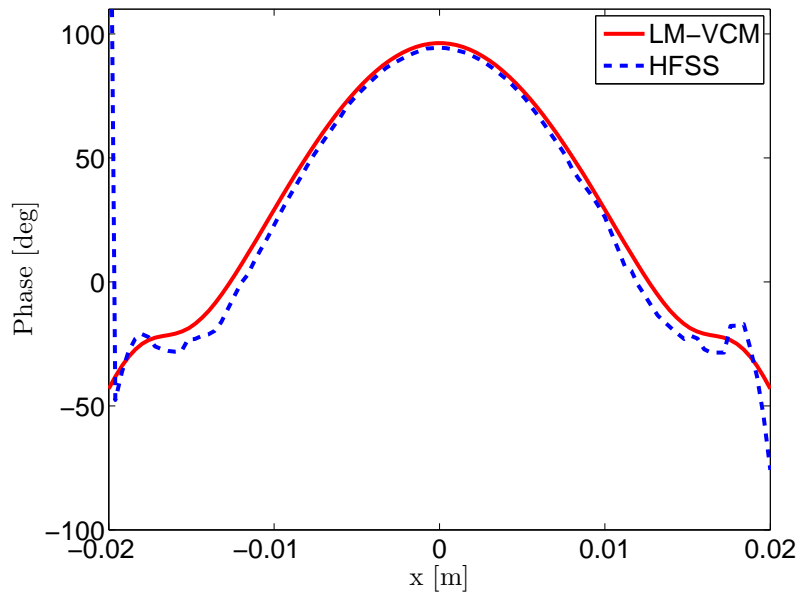
(b)

Figure 3.21: Calculated and simulated E_y field along the line x=[-20mm:20mm], y=0, z=60mm for a 50mm long tapered rod antenna with $a_{max} = 1mm$, $a_{min} = 0.75mm$: (a) Magnitude; (b) Phase
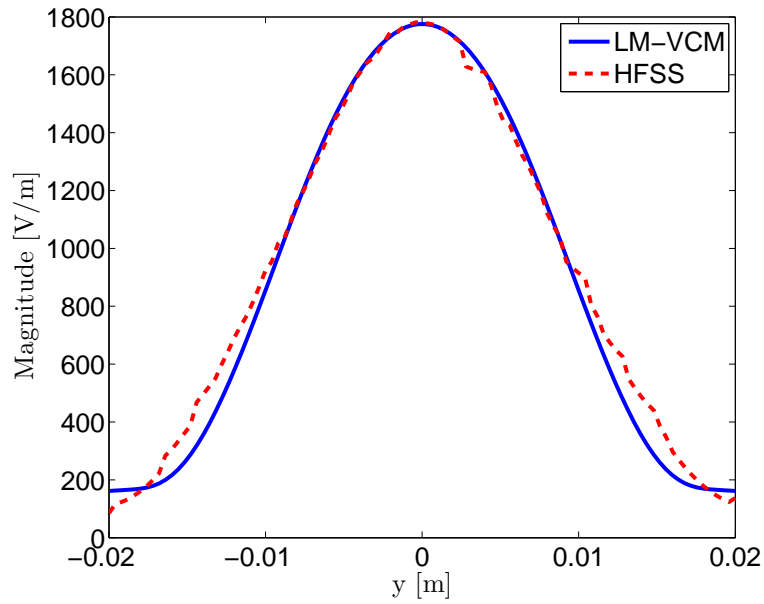
(a)
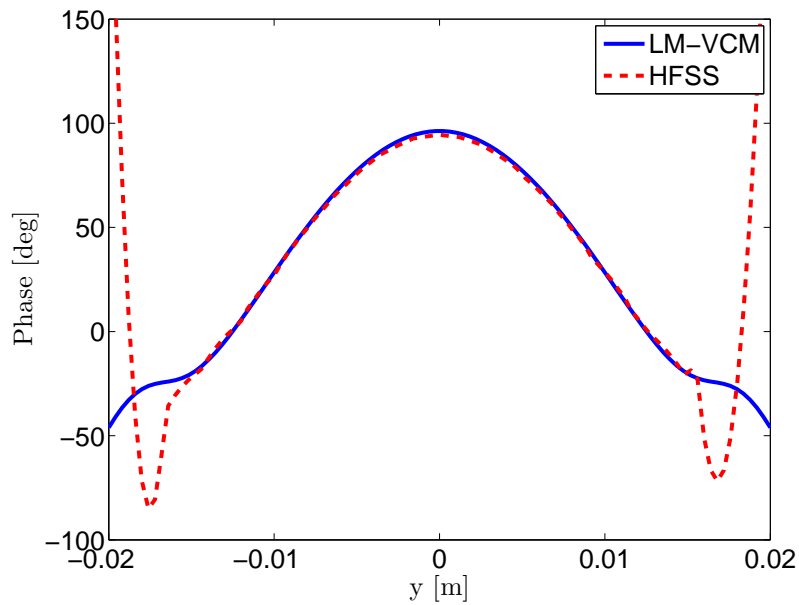
(b)

Figure 3.22: Calculated and simulated E_y field along the line y=[-20mm:20mm], x=0, z=60mm for a 50mm long tapered rod antenna with $a_{max} = 1mm$, $a_{min} = 0.75mm$: (a) Magnitude; (b) Phase
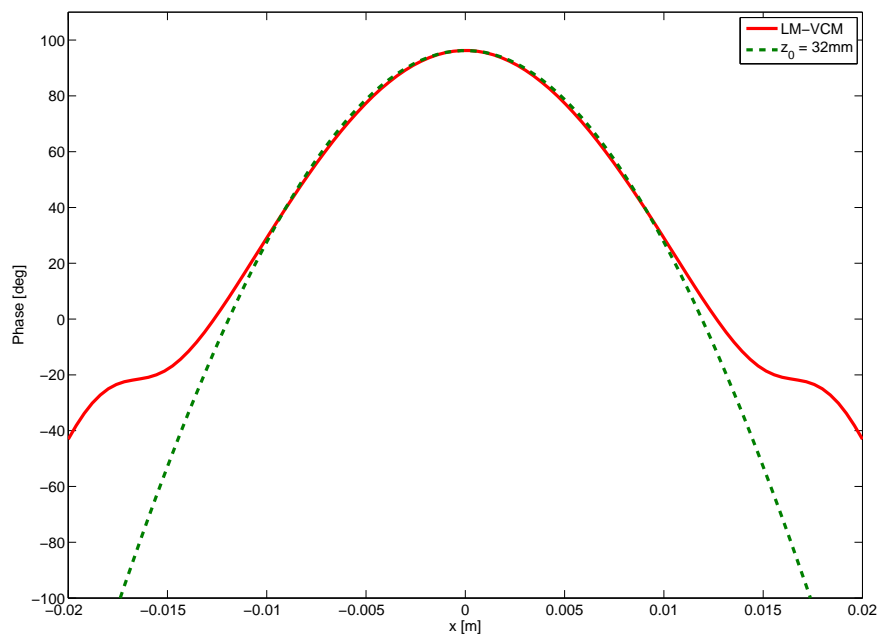
Figure 3.23: Comparison of calculated phase of E_y field from Equation (3.53) and LM-VCM along the line x=[-20mm:20mm], y=0, z=60mm for a 50mm long tapered rod antenna with $a_{max} = 1mm$, $a_{min} = 0.75mm$

Chapter 4

Conclusion and Future Works

In this thesis, we have discussed analytical methods for axis-symmetric structure like disk resonators and dielectric rod antenna. We have shown that the DWM based method for WGM resonance frequencies has good agreements with numerical and experimental results. A quality factor analysis and a resonator-waveguide coupling analysis have also been presented for WGM resonator design. We have demonstrated the LM-VCM is useful in predicting the radiation pattern of slowly tapered circular dielectric rod antenna.

Some of the future works can be

- Perturbation correction [37] of the WGM resonance frequency calculated by DWM method

- Sensitivity analysis of the waveguide coupled WGM resonator sensor

- MMW receiver using WGM microdisk

- Concentrically coupled ring resonators analyzed by DWM

- CMT applied to the laterally coupled disk resonator

- New feeding structure for the dielectric rod antenna : coplanar slots and slotted rectangular waveguide

- Radiation from tapered rectangular waveguide

- BOR-FEM analysis of dielectric rod antenna

APPENDICES

Appendix A

Useful Identities for Bessel functions

A.1 Recursive Relationship

$$J'_n(k) = \frac{1}{2}\left[J_{n-1}(k) - J_{n+1}(k)\right] \tag{A.1}$$

$$J_n(k) = \frac{k}{2n}\left[J_{n-1}(k) + J_{n+1}(k)\right] \tag{A.2}$$

$$K'_n(k) = -\frac{1}{2}\left[K_{n-1}(k) + K_{n+1}(k)\right] \tag{A.3}$$

$$K_n(k) = -\frac{k}{2n}\left[K_{n-1}(k) - K_{n+1}(k)\right] \tag{A.4}$$

A.2 Integral Identity

$$\int_0^{2\pi} \exp\left[-jk_0\rho\cos\phi' - in\phi'\right]d\phi' = 2\pi(j)^{-n}J_n(k_0\rho) \tag{A.5}$$

$$\int_0^{2\pi} e^{jn\phi'} \exp\left[jk_0\rho'\sin\theta_0\cos(\phi' - \phi_0)\right]d\phi' = e^{jn\phi_0}2\pi j^n J_n(k_0\sin\theta_0\rho') \tag{A.6}$$

$$\int_0^a J_n^2(k\rho)\rho d\rho = \begin{cases} \frac{a^2}{2}\left[J_0^2(ka) + J_1^2(ka)\right] & (m = 0) \\ \frac{a^2}{2}\left[J_n^2(ka) - J_{n-1}(ka)J_{n+1}(ka)\right] & (m \geq 1) \end{cases} \tag{A.7}$$

$$\int_a^\infty K_n^2(k\rho)\rho d\rho = \begin{cases} \frac{a^2}{2}\left[K_0^2(ka) - K_1^2(ka)\right] & (m=0) \\ \frac{a^2}{2}\left[K_{n-1}(ka)K_{n+1}(ka) - K_n^2(ka)\right] & (m \geq 1) \end{cases} \qquad \text{(A.8)}$$

$$\int_0^a J_n(k_1\rho)J_m(k_2\rho)\rho d\rho$$
$$= \frac{a}{k_1^2 - k_2^2}\left[k_1 J_n(k_1 a)J_{m+1}(k_2 a) - k_2 J_{n+1}(k_1 a)J_m(k_2 a)\right] \qquad \text{(A.9)}$$

$$\int_a^\infty K_n(k_1\rho)J_m(k_2\rho)\rho d\rho$$
$$= -\frac{a}{k_1^2 - k_2^2}\left[k_1 K_n(k_1 a)J_{m+1}(k_2 a) - k_2 K_{n+1}(k_1 a)J_m(k_2 a)\right] \qquad \text{(A.10)}$$

Appendix B

Basis Functions and Local Matrices for Finite Element Method
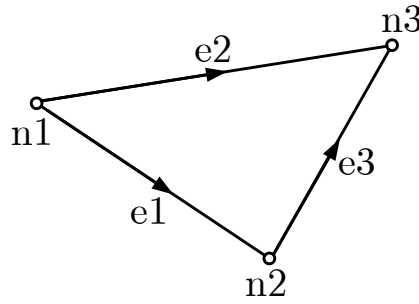
Figure B.1: Local numbering of nodes and edges in a triangle element (Note that edges direct from lower-numbered nodes to higher-numbered nodes)

The local numbering of edges and nodes are shown in figure B.1. The 1st-order edge basis functions are expressed in terms of 1st-order nodal basis function

$$
\begin{aligned}
\overrightarrow{N}_1^e &= \varphi_1^e \cdot \nabla \varphi_2^e - \varphi_2^e \cdot \nabla \varphi_1^e \\
\overrightarrow{N}_2^e &= \varphi_1^e \cdot \nabla \varphi_3^e - \varphi_3^e \cdot \nabla \varphi_1^e \\
\overrightarrow{N}_3^e &= \varphi_2^e \cdot \nabla \varphi_3^e - \varphi_3^e \cdot \nabla \varphi_2^e
\end{aligned}
\qquad (B.1)
$$

φ_i^e are 1st-order nodal basis function which is linear interpolating functions on a triangular element with value 1 on node i and 0 on other node.

$$
[A_1] = \iint_{\triangle} \left(\overrightarrow{\nabla}_t \times \left\{ \overrightarrow{N}^e \right\} \right) \cdot \left(\overrightarrow{\nabla}_t \times \left\{ \overrightarrow{N}^e \right\}^t \right) dS = \frac{\mathbf{S}^{00}}{|J|^2}
\qquad (B.2)
$$

where

$$
\mathbf{S}^{00} = \begin{bmatrix} +2 & -2 & +2 \\ -2 & +2 & -2 \\ +2 & -2 & +2 \end{bmatrix} \qquad J = \hat{z} \cdot \left(\overrightarrow{l}\,^e_1 \times \overrightarrow{l}\,^e_2 \right)
$$

$\overrightarrow{l}\,^e_i$ is the vector with magnitude equals the length of edge i and direction shown in Figure B.1. It can be observed that $|J|$ equals two times the area of triangular element.

$$
\begin{aligned}
[A_2] &= \iint_{\triangle} \left\{ \overrightarrow{N}^e \right\} \cdot \left\{ \overrightarrow{N}^e \right\}^t dS && \text{(B.3)} \\
&= |J| \left(\overrightarrow{\nabla}_t \varphi^e_2 \cdot \overrightarrow{\nabla}_t \varphi^e_2 \mathbf{M}^{22} + \overrightarrow{\nabla}_t \varphi^e_2 \cdot \overrightarrow{\nabla}_t \varphi^e_3 \mathbf{M}^{23} + \overrightarrow{\nabla}_t \varphi^e_3 \cdot \overrightarrow{\nabla}_t \varphi^e_3 \mathbf{M}^{33} \right)
\end{aligned}
$$

$$
\mathbf{M}^{22} = \frac{1}{12} \begin{bmatrix} +3 & +1 & -1 \\ +1 & +1 & -1 \\ -1 & -1 & +1 \end{bmatrix} \qquad \mathbf{M}^{23} = \frac{1}{12} \begin{bmatrix} +3 & +3 & +1 \\ +3 & +3 & -1 \\ +1 & -1 & -1 \end{bmatrix}
$$

$$
\mathbf{M}^{23} = \frac{1}{12} \begin{bmatrix} +1 & +1 & +1 \\ +1 & +3 & +1 \\ +1 & +1 & +1 \end{bmatrix}
$$

$$
\begin{aligned}
[A_3] &= \iint_{\triangle} \left\{ \overrightarrow{N}^e \right\} \cdot \overrightarrow{\nabla}_t \left\{ \varphi^e \right\}^t dS && \text{(B.4)} \\
&= |J| \left(\overrightarrow{\nabla}_t \varphi^e_2 \cdot \overrightarrow{\nabla}_t \varphi^e_2 \mathbf{K}^{22} + \overrightarrow{\nabla}_t \varphi^e_2 \cdot \overrightarrow{\nabla}_t \varphi^e_3 \mathbf{K}^{23} + \overrightarrow{\nabla}_t \varphi^e_3 \cdot \overrightarrow{\nabla}_t \varphi^e_3 \mathbf{K}^{33} \right)
\end{aligned}
$$

$$
\mathbf{K}^{22} = \frac{1}{6} \begin{bmatrix} -2 & +2 & +0 \\ -1 & +1 & +0 \\ +1 & -1 & +0 \end{bmatrix} \qquad \mathbf{K}^{23} = \frac{1}{6} \begin{bmatrix} -3 & +1 & +2 \\ -3 & +2 & +1 \\ +0 & +1 & -1 \end{bmatrix}
$$

$$
\mathbf{K}^{23} = \frac{1}{6} \begin{bmatrix} -1 & +0 & +1 \\ -2 & +0 & +2 \\ -1 & +0 & +1 \end{bmatrix}
$$

$$[A_4] \;=\; \iint_\triangle \{\varphi^e\}\{\varphi^e\}^t\, dS \tag{B.5}$$

$$=\; \frac{|J|}{24} \begin{bmatrix} 2 & 1 & 1 \\ 1 & 2 & 1 \\ 1 & 1 & 2 \end{bmatrix}$$

$$[A_5] \;=\; \iint_\triangle \overrightarrow{\nabla}_t \varphi_q^e \cdot \overrightarrow{\nabla}_t \varphi_p^e\, dS \tag{B.6}$$

$$=\; \frac{|J|}{2} \begin{bmatrix} \overrightarrow{\nabla}_t \varphi_1^e \cdot \overrightarrow{\nabla}_t \varphi_1^e & \overrightarrow{\nabla}_t \varphi_1^e \cdot \overrightarrow{\nabla}_t \varphi_2^e & \overrightarrow{\nabla}_t \varphi_1^e \cdot \overrightarrow{\nabla}_t \varphi_3^e \\ \overrightarrow{\nabla}_t \varphi_2^e \cdot \overrightarrow{\nabla}_t \varphi_1^e & \overrightarrow{\nabla}_t \varphi_2^e \cdot \overrightarrow{\nabla}_t \varphi_2^e & \overrightarrow{\nabla}_t \varphi_2^e \cdot \overrightarrow{\nabla}_t \varphi_3^e \\ \overrightarrow{\nabla}_t \varphi_3^e \cdot \overrightarrow{\nabla}_t \varphi_1^e & \overrightarrow{\nabla}_t \varphi_3^e \cdot \overrightarrow{\nabla}_t \varphi_2^e & \overrightarrow{\nabla}_t \varphi_3^e \cdot \overrightarrow{\nabla}_t \varphi_3^e \end{bmatrix}$$

$$=\; \frac{|J|}{2} \left(\overrightarrow{\nabla}_t \varphi_2^e \cdot \overrightarrow{\nabla}_t \varphi_2^e \begin{bmatrix} +1 & -1 & +0 \\ -1 & +1 & +0 \\ +0 & +0 & +0 \end{bmatrix} + \overrightarrow{\nabla}_t \varphi_2^e \cdot \overrightarrow{\nabla}_t \varphi_3^e \begin{bmatrix} +2 & -1 & -1 \\ -1 & +0 & +1 \\ -1 & +1 & +0 \end{bmatrix} \right.$$

$$\left. + \overrightarrow{\nabla}_t \varphi_3^e \cdot \overrightarrow{\nabla}_t \varphi_3^e \begin{bmatrix} +1 & +0 & -1 \\ +0 & +0 & +0 \\ -1 & +0 & +1 \end{bmatrix} \right)$$

From the above expression, it is easily observed that only $\nabla_t \varphi_2^e, \nabla \varphi_3^e$, and J are varying for different elements and we need only calculating these local values while implementing a numerical procedure.

References

[1] P. Affolter and B. Eliasson. Electromagnetic resonances and q-factors of lossy dielectric spheres. *Microwave Theory and Techniques, IEEE Transactions on*, 21(9):573–578, Sep 1973.

[2] T. Ando, Isao Ohba, S. Numata, J. Yamauchi, and H. Nakano. Linearly and curvilinearly tapered cylindrical- dielectric-rod antennas. *Antennas and Propagation, IEEE Transactions on*, 53(9):2827–2833, Sept. 2005. 46, 47, 55, 69

[3] T. Ando, J. Yamauchi, and H. Nakano. Numerical analysis of a dielectric rod antenna - demonstration of the discontinuity-radiation concept. *Antennas and Propagation, IEEE Transactions on*, 51(8):2007–2013, Aug. 2003. 46

[4] G. Annino, M. Cassettari, M. Fittipaldi, I. Longo, M. Martinelli, C. A. Massa, and L. A. Pardi. High-field, multifrequency epr spectroscopy using whispering gallery dielectric resonators. *Journal of Magnetic Resonance*, 143(1):88 – 94, 2000. 2, 4

[5] G. Annino, M. Cassettari, I. Longo, and M. Martinelli. Whispering gallery modes in a dielectric resonator: characterization at millimeter wavelength. *Microwave Theory and Techniques, IEEE Transactions on*, 45(11):2025–2034, Nov 1997. 8, 9, 11, 38

[6] Ansoft Corp., Pittsburg, PA. *High Frequency Structure Simulator (HFSS) v10*, 2006. 53

[7] T. Baba. Photonic crystals and microdisk cavities based on gainasp-inp system. *Selected Topics in Quantum Electronics, IEEE Journal of*, 3(3):808–830, Jun 1997. 4

[8] C. A. Balanis. *Antenna Theory: Analysis and Design*. Wiley-Interscience, 3rd edition, 2005. 64

[9] W. Berglund and A. Gopinath. Wkb analysis of bend losses in optical waveguides. *Lightwave Technology, Journal of*, 18(8):1161–1166, Aug 2000. 5

[10] J. Blakey. A scattering theory approach to the prediction of dielectric rod antenna radiation patterns: The tm01mode. *Antennas and Propagation, IEEE Transactions on*, 23(4):577–579, Jul 1975. 46, 57

[11] M.D. Blech and T.F. Eibert. A dipole excited ultrawideband dielectric rod antenna with reflector. *Antennas and Propagation, IEEE Transactions on*, 55(7):1948–1954, July 2007. 46

[12] C. F. Bohren and D. R. Huffman. *Absorption and Scattering of Light by Small Particles*. Wiley, 1st edition, 1983. 4

[13] A. Bondeson, T. Rylander, and P. Ingelstrom. *Computational Electromagnetics*. Springer, 1st edition, 2005. 18

[14] Robert W. Boyd and John E. Heebner. Sensitive disk resonator photonic biosensor. *Appl. Opt.*, 40(31):5742–5747, 2001. 4

[15] Ming Cai, Oskar Painter, and Kerry J. Vahala. Observation of critical coupling in a fiber taper to a silica-microsphere whispering-gallery mode system. *Phys. Rev. Lett.*, 85(1):74–77, Jul 2000. 43

[16] Chi-Chih Chen, Kishore Rama Rao, and R. Lee. A new ultrawide-bandwidth dielectric-rod antenna for ground-penetrating radar applications. *Antennas and Propagation, IEEE Transactions on*, 51(3):371–377, March 2003. 46

[17] N. Chen and Z. L. Sun. Theoretical analysis of whispering-gallery mode dielectric resonator in mm-wave mic. *International Journal of Infrared and Millimeter Waves*, 14(1):1801–1812, Sep 1993. 4

[18] M.K. Chin and S.T. Ho. Design and modeling of waveguide-coupled single-mode microring resonators. *Lightwave Technology, Journal of*, 16(8):1433–1446, Aug 1998. 4, 5

[19] Jae-Young Chung and Chi-Chih Chen. Two-layer dielectric rod antenna. *Antennas and Propagation, IEEE Transactions on*, 56(6):1541–1547, June 2008. 46

[20] A. Elsherbini, Cemin Zhang, Song Lin, M. Kuhn, A. Kamel, A.E. Fathy, and H. Elhennawy. Uwb antipodal vivaldi antennas with protruded dielectric rods for higher gain, symmetric patterns and minimal phase center variations. *Antennas and Propagation Society International Symposium, 2007 IEEE*, pages 1973–1976, June 2007. 46

[21] S. Gigoyan, D. Saeedkia, M. Neshat, Huanyu Chen, and S. Safavi-Naeini. Tapered dielectric image-line antenna array for millimeter-wave applications. *Radio and Wireless Symposium, 2008 IEEE*, pages 667–670, Jan. 2008. 1

[22] Jose Ma Gil, Javier Monge, J. Rubio, and J. Zapata. A cad-oriented method to analyze and design radiating structures based on bodies of revolution by using finite elements and generalized scattering matrix. *Antennas and Propagation, IEEE Transactions on*, 54(3):899–907, March 2006. 46

[23] M. L. Gorodetsky and V. S. Ilchenko. Optical microsphere resonators: optimal coupling to high-q whispering-gallery modes. *J. Opt. Soc. Am. B*, 16(1):147–154, 1999. 5, 43

[24] A.D. Greenwood and Jian-Ming Jin. Finite-element analysis of complex axisymmetric radiating structures. *Antennas and Propagation, IEEE Transactions on*, 47(8):1260–1266, Aug 1999.

[25] S.C. Hagness, D. Rafizadeh, S.T. Ho, and A. Taflove. Fdtd microcavity simulations: design and experimental realization of waveguide-coupled single-mode ring and whispering-gallery-mode disk resonators. *Lightwave Technology, Journal of*, 15(11):2154–2165, Nov 1997.

[26] S. Hanham, T. Bird, and B. Johnston. A ring slot excited dielectric rod antenna for terahertz imaging. *Antennas and Propagation Society International Symposium, 2007 IEEE*, pages 5539–5542, June 2007. 46

[27] R. F. Harrington. *Time-Harmonic Electromagnetic Fields*. Wiley-IEEE Press, 2nd edition, 2001. 30, 57

[28] H. Haus, W. Huang, S. Kawakami, and N. Whitaker. Coupled-mode theory of optical waveguides. *Lightwave Technology, Journal of*, 5(1):16–23, Jan 1987. 5

[29] John E. Heebner, Tiziana C. Bond, and Jeff S. Kallman. Generalized formulation for performance degradations due to bending and edge scattering loss in microdisk resonators. *Opt. Express*, 15(8):4452–4473, 2007. 5, 32

[30] A. Hees, J. Hasch, and J. Detlefsen. Characteristics of a corrugated tapered slot antenna with dielectric rod and metallic reflector. *Ultra-Wideband, 2008. ICUWB 2008. IEEE International Conference on*, 1:1–4, Sept. 2008. 46

[31] M. Hossein-Zadeh and K.J. Vahala. Photonic rf down-converter based on optomechanical oscillation. *Photonics Technology Letters, IEEE*, 20(4):234–236, Feb.15, 2008. 4

[32] Kao-Cheng Huang and D.J. Edwards. 60 ghz multibeam antenna array for gigabit wireless communication networks. *Antennas and Propagation, IEEE Transactions on*, 54(12):3912–3914, Dec. 2006. 1

[33] Kao-Cheng Huang and Zhaocheng Wang. V-band patch-fed rod antennas for high data-rate wireless communications. *Antennas and Propagation, IEEE Transactions on*, 54(1):297–300, Jan. 2006. 46

[34] T. Itoh and R.S. Rudokas. New method for computing the resonant frequencies of dielectric resonators (short papers). *Microwave Theory and Techniques, IEEE Transactions on*, 25(1):52–54, Jan 1977. 4, 9

[35] Xiao Hu Jiao, P. Guillon, L.A. Bermudez, and P. Auxemery. Whispering-gallery modes of dielectric structures: Applications to millimeter-wave band-stop filters. *Microwave Theory and Techniques, IEEE Transactions on*, 35(12):1169–1175, Dec 1987. 1, 4, 43

[36] D. Kajfez, A.W. Glisson, and J. James. Computed modal field distributions for isolated dielectric resonators. *Microwave Theory and Techniques, IEEE Transactions on*, 32(12):1609–1616, Dec 1984. 15

[37] D. Kajfez and P. Guillon. *Dielectric Resonators*. Artech House, 1st edition, 1986. 4, 5, 76

[38] A. Kishk and L. Shafai. Radiation characteristics of the short dielectric rod antenna: A numerical solution. *Antennas and Propagation, IEEE Transactions on*, 35(2):139–146, Feb 1987. 46

[39] R.M. Knox. Dielectric waveguide microwave integrated circuits—an overview. *Microwave Theory and Techniques, IEEE Transactions on*, 24(11):806–814, Nov 1976. 1

[40] S. Kobayashi, R. Mittra, and R. Lampe. Dielectric tapered rod antennas for millimeter-wave applications. *Antennas and Propagation, IEEE Transactions on*, 30(1):54–58, Jan 1982. 46

[41] S. Kobayashi, R. Mittra, and R. Lampe. Dielectric tapered rod antennas for millimeter-wave applications. *Antennas and Propagation, IEEE Transactions on*, 30(1):54–58, Jan 1982.

[42] S. K. Koul. *Millimeter Wave and Optical Dielectric Integrated Guides and Circuits*. John Wiley & Sons Incs, 1997. 9, 11

[43] J. Krupka, K. Derzakowski, A. Abramowicz, M.E. Tobar, and R.G. Geyer. Use of whispering-gallery modes for complex permittivity determinations of ultra-low-loss dielectric materials. *Microwave Theory and Techniques, IEEE Transactions on*, 47(6):752–759, Jun 1999. 4, 5, 20

[44] R. Kumar Mongia and A. Ittipiboon. Theoretical and experimental investigations on rectangular dielectric resonator antennas. *Antennas and Propagation, IEEE Transactions on*, 45(9):1348–1356, Sep 1997. 30

[45] M. Kuznetsov and H. Haus. Radiation loss in dielectric waveguide structures by the volume current method. *Quantum Electronics, IEEE Journal of*, 19(10):1505–1514, Oct 1983. 5, 30

[46] Juha-Pekka Laine, Charles Tapalian, Brent Little, and Hermann Haus. Acceleration sensor based on high-q optical microsphere resonator and pedestal antiresonant reflecting waveguide coupler. *Sensors and Actuators A: Physical*, 93(1):1 – 7, 2001. 4

[47] J.-F. Lee, D.-K. Sun, and Z.J. Cendes. Full-wave analysis of dielectric waveguides using tangential vector finite elements. *Microwave Theory and Techniques, IEEE Transactions on*, 39(8):1262–1271, Aug 1991. 16, 17

[48] Jin-Fa Lee, G.M. Wilkins, and R. Mitra. Finite-element analysis of axisymmetric cavity resonator using a hybrid edge element technique. *Microwave Theory and Techniques, IEEE Transactions on*, 41(11):1981–1987, Nov 1993. 4, 15, 16

[49] Bing-Jing Li and Pao-Lo Liu. Numerical analysis of the whispering gallery modes by the finite-difference time-domain method. *Quantum Electronics, IEEE Journal of*, 32(9):1583–1587, Sep 1996. 4, 15

[50] B.E. Little, S.T. Chu, H.A. Haus, J. Foresi, and J.-P. Laine. Microring resonator channel dropping filters. *Lightwave Technology, Journal of*, 15(6):998–1005, Jun 1997. 4, 5

[51] B.E. Little, J.-P. Laine, and H.A. Haus. Analytic theory of coupling from tapered fibers and half-blocks into microsphere resonators. *Lightwave Technology, Journal of*, 17(4):704–715, Apr 1999. 4, 5, 30, 34, 42

[52] L. Maleki, A. B. Matsko, A. A. Savchenkov, and V. S. Ilchenko. Tunable delay line with interacting whispering-gallery-moderesonators. *Opt. Lett.*, 29(6):626–628, 2004. 4

[53] E. A. J. Marcatili. Dielectric rectangular waveguide and directional coupler for integrated optics. *Bell Syst. Tech. J*, 48:2071–2102, 1969. 5, 9, 20, 40

[54] A.B. Matsko and V.S. Ilchenko. Optical resonators with whispering-gallery modes-part i: basics. *Selected Topics in Quantum Electronics, IEEE Journal of*, 12(1):3–14, Jan.-Feb. 2006. 4, 5

[55] S. L. McCall, A. F. J. Levi, R. E. Slusher, S. J. Pearton, and R. A. Logan. Whispering-gallery mode microdisk lasers. *Applied Physics Letters*, 60(3):289–291, 1992. 4

[56] R.K. Mongia. Resonant frequency of cylindrical dielectric resonator placed in an mic environment. *Microwave Theory and Techniques, IEEE Transactions on*, 38(6):802–804, Jun 1990. 4

[57] A. Morand, K. Phan-Huy, Y. Desieres, and P. Benech. Analytical study of the microdisk's resonant modes coupling with a waveguide based on the perturbation theory. *Lightwave Technology, Journal of*, 22(3):827–832, March 2004. 5, 32

[58] G. E. Mueller and W. A. Tyrrell. Polyrod antennas. *Bell. Syst. Tech. J.*, 26:851šC837, Oct 1947. 1, 46

[59] M. Neshat, S. Gigoyan, D. Saeedkia, and S. Safavi-Naeini. Travelling-wave whispering gallery resonance sensor in millimetre-wave range. *Electronics Letters*, 44(17):1020–1022, 14 2008. 2, 5

[60] E. Niver. Tapered dielectric rod antenna. In *Complex Computing-Networks*. Springer, 2006. 46, 51, 57

[61] K. Okamoto. *Fundamentals of Optical Waveguides*. Academic Press, 2000. 6, 23, 40, 48

[62] A. Patrovsky and Ke Wu. 94-ghz planar dielectric rod antenna with substrate integrated image guide (siig) feeding. *Antennas and Wireless Propagation Letters, IEEE*, 5(1):435–437, Dec. 2006.

[63] A. Patrovsky and Ke Wu. 94-ghz broadband transition from coplanar waveguide to substrate integrated image guide (siig). *Microwave Symposium, 2007. IEEE/MTT-S International*, pages 1551–1554, June 2007. 46

[64] Hong Peng. Study of whispering gallery modes in double disk sapphire resonators. *Microwave Theory and Techniques, IEEE Transactions on*, 44(6):848–853, Jun 1996. 5, 9

[65] L. Rayleigh. The problem of the whipering gallery. *Phil. Mag.*, 20:1001–1004, 1910. 4

[66] J. Richter, M. Muller, and L.-P. Schmidt. Measurement of phase centers of rectangular dielectric rod antennas. *Antennas and Propagation Society International Symposium, 2004. IEEE*, 1:743–746 Vol.1, June 2004. 70

[67] J. Richter, D. Notel, F. Kloppel, J. Huck, H. Essen, and L.-P. Schmidt. A multi-channel radiometer with focal plane array antenna for w-band passive millimeterwave imaging. *Microwave Symposium Digest, 2006. IEEE MTT-S International*, pages 1592–1595, June 2006. 47, 70

[68] Jurgen Richter, Yasar Yazici, Christof Ziegler, and Lorenz-Peter Schmidt. A broadband transition between dielectric and planar waveguides at millimeter-wave frequencies. *European Microwave Conference, 2003. 33rd*, pages 947–950, Oct. 2003. 46

[69] D.R. Rowland and J.D. Love. Evanescent wave coupling of whispering gallery modes of a dielectric cylinder. *Optoelectronics, IEE Proceedings J*, 140(3):177–188, Jun 1993. 5, 8, 32, 42

[70] D. Schaubert, D. Wilton, and A. Glisson. A tetrahedral modeling method for electromagnetic scattering by arbitrarily shaped inhomogeneous dielectric bodies. *Antennas and Propagation, IEEE Transactions on*, 32(1):77–85, Jan 1984. 30

[71] S. Schlesinger and A. Vigants. Experimental comparison of image line radiators and polyrod antennas. *Antennas and Propagation, IRE Transactions on*, 8(5):521–522, September 1960. 1, 46

[72] F. Schwering, A. A. Oliner, Y. T. Lo, and S. W. Lee. Millimeter-wave antennas. In *Antenna Handbook*, volume 3, chapter 17. Van Nostrand Reinhold, New York, 1993. 46

[73] Yih Shiau. Dielectric rod antennas for millimeter-wave integrated circuits (short papers). *Microwave Theory and Techniques, IEEE Transactions on*, 24(11):869–872, Nov 1976. 1, 46

[74] T. Shimizu and T. Yoneyama. Feeding structures for 60-ghz dielectric lens antenna with low sidelobes. *Electronics and Communications in Japan (Part II: Electronics)*, 89(8):16–26, 2006. 47, 70

[75] K. Solbach and I. Wolff. The electromagnetic fields and the phase constants of dielectric image lines. *Microwave Theory and Techniques, IEEE Transactions on*, 26(4):266–274, Apr 1978. 1

[76] A.C. Studd. Towards a better dielectric rod antenna. *Antennas and Propagation, 1991. ICAP 91., Seventh International Conference on (IEE)*, pages 117–120 vol.1, Apr 1991. 46

[77] A. Taflove and S. C. Hangess. *Computational Electrodynamics: The Finite-Difference Time-Domain Method.* Artech, 2nd edition, 2007. 4

[78] H. Tehrani, Ming-Yi Li, and Kai Chang. Broadband microstrip to dielectric image line transitions. *Microwave and Guided Wave Letters, IEEE*, 10(10):409–411, Oct 2000. 46

[79] M.E. Tobar and A.G. Mann. Resonant frequencies of higher order modes in cylindrical anisotropic dielectric resonators. *Microwave Theory and Techniques, IEEE Transactions on*, 39(12):2077–2082, Dec 1991. 1, 4, 9

[80] T.N. Trinh, J.A.G. Malherbe, and R. Mittra. A metal-to-dielectric waveguide transition with application to millimeter-wave integrated circuits. *Microwave Symposium Digest, 1980 MTT-S International*, 80(1):205–207, May 1980. 46

[81] Kerry J. Vahala. Optical microcavities. *Nature*, 424:839–846, Aug 2003. 4

[82] C. Vedrenne and J. Arnaud. Whispering-gallery modes of dielectric resonators. *Microwaves, Optics and Antennas, IEE Proceedings H*, 129(4):183–187, August 1982. 4, 8

[83] J. R. Wait. Electromagnetic whispering-gallery modes in a dielectric rod. *Radio Sci.*, 2:1005–1017, 1967. 6

[84] G.M. Whitman, C. Pinthong, A.A. Triolo, and F.K. Schwering. An approximate but accurate analysis of the dielectric wedge antenna fed by a slab waveguide using the local mode theory and schelkunoff equivalence principle. *Antennas and Propagation, IEEE Transactions on*, 54(4):1111–1121, April 2006. 30, 46, 51, 57, 69

[85] A. Yaghjian and E. Kornhauser. A modal analysis of the dielectric rod antenna excited by the he11mode. *Antennas and Propagation, IEEE Transactions on*, 20(2):122–128, Mar 1972. 46, 47

[86] Fei-Ran Yang, Yongxi Qian, and T. Itoh. A novel high-q image guide resonator using band-gap structures. *Microwave Symposium Digest, 1998 IEEE MTT-S International*, 3:1803–1806 vol.3, Jun 1998. 46

[87] C. Yao, S. E. Schwarz, and Blumenstock B. J. Monolithic integration of a dielectric millimeter-wave antenna and mixer diode: An embryonic millimeter-wave ic. *Microwave Theory and Techniques, IEEE Transactions on*, 82(8):1241–1247, Aug 1982. 46

[88] A. Yariv. Coupled-mode theory for guided-wave optics. *Quantum Electronics, IEEE Journal of*, 9(9):919–933, Sep 1973. 5

[89] C. Yeh and F. I. Shimabukuro. *The Essence of Dielectric Waveguides*. Springer, 1st edition, 2008. 13

[90] T. Yoneyama and S. Nishida. Nonradiative dielectric waveguide for millimeter-wave integrated circuits. *Microwave Theory and Techniques, IEEE Transactions on*, 29(11):1188–1192, Nov 1981. 1

[91] F. J. Zucker and R. C. Johnson. Surface-wave antennas and surface-wave excited arrays. In *Antenna Engineering Handbook*, chapter 12. McGraw-Hill, New York, 3rd edition, 1993. 46, 47, 65

[92] A. V. Zvyagin and K. Goto. Mie scattering of evanescent waves by a dielectric sphere: comparison of multipole expansion and group-theory methods. *J. Opt. Soc. Am. A*, 15(12):3003–3008, 1998.